

Syracuse University

SURFACE

Physics - Dissertations

College of Arts and Sciences

5-2012

Geometries in Soft Matter

Zhenwei Yao

Syracuse University

Follow this and additional works at: https://surface.syr.edu/phy_etd



Part of the [Physics Commons](#)

Recommended Citation

Yao, Zhenwei, "Geometries in Soft Matter" (2012). *Physics - Dissertations*. 125.

https://surface.syr.edu/phy_etd/125

This Dissertation is brought to you for free and open access by the College of Arts and Sciences at SURFACE. It has been accepted for inclusion in Physics - Dissertations by an authorized administrator of SURFACE. For more information, please contact surface@syr.edu.

Abstract

This thesis explores geometric aspects of soft matter systems. The topics covered fall into three categories: (i) geometric frustrations, including the interplay of geometry and topological defects in two dimensional systems, and the frustration of a planar sheet attached to a curved surface; (ii) geometries of liquid droplets, including the curvature driven instabilities of toroidal liquid droplets and the self-propulsion of droplets on a spatially varying surface topography; (iii) the study of the electric double layer structure around charged spherical interfaces by a geometric method. In (i), we study the crystalline order on capillary bridges with varying Gaussian curvature. Energy requires the appearance of topological defects on the surface, which are natural spots for biological activity and chemical functionalization. We further study how liquid crystalline order deforms flexible structured vesicles. In particular we find faceted tetrahedral vesicle as the ground state, which may lead to the design of supra-molecular structures with tetrahedral symmetry and new classes of nano-carriers. Furthermore, by a simple paper model we explore the geometric frustration on a planar sheet when brought to a negative curvature surface in a designed elasto-capillary system. In (ii), motivated by the idea of realizing crystalline order on a *stable* toroidal droplet and a beautiful experiment on toroidal droplets, we study the Rayleigh instability and the shrinking instability of thin and fat toroidal droplets, where the toroidal geometry plays an essential role. In (iii), by a geometric mapping we construct an approximate analytic spherical solution to the nonlinear Poisson-Boltzmann equation, and identify the applicability regime of the solution. The derived geometric solution enables further analytical study of spherical electrostatic systems such as colloidal suspensions.

Geometries in Soft Matter

*From Geometric Frustration, Liquid Droplets to Electrostatics in
Solution*

by

Zhenwei Yao

B.S. XJTU 2004

M.S. XJTU 2007

DISSERTATION

Submitted in partial fulfillment of the requirements for the
degree of Doctor of Philosophy in Physics
in the Graduate School of Syracuse University

May 2012

Copyright 2012 Zhenwei Yao

All rights reserved

To my grandfather: Yao, Rong Qing

Acknowledgements

My sincere gratitude is to my advisor, Prof. Mark Bowick for training me to recognize and appreciate the beauty and elegance in physics in addition to insightful guides in research. I thank Prof. Xiangjun Xing, now at Shanghai Jiao Tong University, for his guide in research. I appreciate the days when three of us sit down and talk about physics every week. I thank Prof. M. Cristina Marchetti, Bowick and Xing for their strong recommendation in my job application. I also thank the rest of my committee, Prof. Alan Middleton, Patrick Mather, Jennifer Schwarz and Lisa Manning, for making time to read my thesis.

I thank all my friends at Syracuse who make my life colorful. There are too many names to mention individually, and I always wish you the best. Finally I deeply thank my mother and father. Special thanks to my wife for her everlasting support, love, and inspiration.

Contents

1	Introduction	1
1.1	Geometric frustration in two-dimensional systems†	2
1.2	Geometry in liquid droplets	5
1.3	Poisson-Boltzmann theory and beyond	7
2	Crystalline order on catenoidal capillary bridges	13
2.1	Introduction	13
2.1.1	Crystalline order and Euler’s theorem	13
2.1.2	Background	14
2.2	Geometry of capillary bridges	16
2.2.1	A capillary bridge is a CMC surface	17
2.2.2	The solutions to the shape equation	18
2.3	Crystalline order on catenoid	23
2.3.1	The geometric approach	24
2.3.2	Effective disclination charge	27
2.3.3	Energetics of topological defects	29
	Appendix 2.A Conformal mapping of catenoid onto complex plane	35
3	Morphology of nematic and smectic vesicles	37
3.1	Introduction	37
3.2	Model	38

CONTENTS	vii
3.2.1 Free energy	38
3.2.2 Lattice model	41
3.3 Ground state morphologies	43
3.3.1 Analytical analysis	43
3.3.2 Monte Carlo simulation	47
Appendix 3.A Buckling of a LC membrane	51
Appendix 3.B Discrete Frank free energy of 2-dimensional nematic	52
Appendix 3.C Discrete bending energy of isotropic vesicles	55
4 Planar sheets meet negative curvature liquid interfaces	59
4.1 Introduction	59
4.2 Design a negative curvature surface in a capillary tube	60
4.3 Patterns on sheets	64
4.3.1 Concentric wrinkles	64
4.3.2 Eye-like folds	67
4.3.3 Phase diagram	68
4.4 Conclusion	70
5 The instabilities of toroidal droplets. I: Rayleigh instability	72
5.1 Introduction	72
5.2 Free energy	75
5.2.1 Geometry of toroidal interfaces	75
5.2.2 Limitation of the free energy argument	78
5.3 Rayleigh instability of thin toroidal droplets	79
5.3.1 A new scheme in the Stokes flow regime	79
5.3.2 Velocity and vorticity fields	84
5.3.3 The fastest growing mode via energy conservation	95
5.3.4 Discussion	100

CONTENTS	viii
5.4 Rayleigh instability of fat toroidal droplets	105
Appendix 5.A Velocity field in flat interface system	108
Appendix 5.B Derivation of the dissipation rate in cylindrical coordinates	110
6 The instabilities of toroidal droplets. II: Shrinking instability	112
6.1 Pressure driving the flow	113
6.1.1 Laplace pressure	113
6.1.2 Pressure in bulk fluid	114
6.2 Velocity field	120
6.3 Shrinking speed	126
Appendix 6.A The shape of the cross section	129
Appendix 6.B Rayleigh instability vs. shrinking mode	131
7 Self-propulsion of droplets by spatially-varying surface topography	133
7.1 Introduction	134
7.2 Method	135
7.3 Results and discussion	137
8 The electric double layer structure around charged spherical inter-	142
faces	
8.1 Introduction	142
8.2 Approximate spherical solution to the PB equation	143
8.3 Applicability of the geometric solution	148
8.4 Analogy between an EDL system and capillary deformation	150
8.5 Conclusion	152
Bibliography	153

List of Figures

1.1	The spherical image of a surface (left) is obtained by parallel moving all unit normal vectors on that surface (left) onto the unit sphere (right).	4
2.1	The surface area of a catenoid versus its aspect ratio c . The radius of the boundary circular section is $R = 1$.	21
2.2	The distribution of Gaussian curvature on the capillary bridge in Fig.4i in Ref. [35] versus i . $t = t_0 + i * dt, dt = 10^{-5}\pi$. i increases from 0 on the waist of the capillary bridge towards its ends.	22
2.3	(a) The three dimensional shape of a catenoid of aspect ratio $c = 0.85$. (b) A catenoid of aspect ratio $c = 0.9$ (green) deforms to $c = 0.7$ (blue).	24
2.4	(a) A family of geodesics in $\{u, v\}$ coordinates centered at a point on the waist of a catenoid of $c = 0.85$. (b) The $ K(0) \pi r^2$ (dashed curve) and numerical result (solid curve) of the integrated Gaussian curvature over a geodesic disk of radius r versus r . $c = 1/2$.	27
2.5	(a) The geometric potential of an isolated disclination for three different values of c : $c = 0.8$ (red), $c = 0.75$ (green) and $c = 0.7$ (blue). The optimal position of an isolated disclination moves from the boundary to the waist of the catenoid in the rather narrow window c between 0.8 and 0.75. (b) The geometric potential of an isolated disclination for catenoids with $c = 0.5$ (red) and $c = 0.6$ (green).	31

- 2.6 The phase diagram in the particle number-aspect ratio plane for isolated disclinations versus scars for $c < c^*$ 31
- 2.7 (a) The geometric potential of isolated dislocations as a function of height for four different values of c : $c = 0.7$ (black), $c = 0.68$ (red), $c = 0.66$ (blue) and $c = 0.65$ (green). The optimal position moves from near the boundary towards the waist as c decreases. (b) is an enlarged view of the blue curve to show the transition from the red to the green curve. 33
- 2.8 The interactions of defects. (a) The dislocation-dislocation interaction V_{dd} of two dislocations along \vec{e}^u at the same height. $z = 0.5 z_m$ (black), $z = 0.3 z_m$ (red) and $z = 0.1 z_m$ (green). (b) The disclination-dislocation interaction V_{Dd} as a function of their longitudinal separation. The disclination is fixed on the waist ($c = 1/2$). 33
- 3.1 Top: A tetrahedron compatible with $+1/2$ disclination on each vertex can be constructed using a parallelogram, by folding along the dashed lines. A constant nematic director field in the unfold parallelogram is shown by the array of parallel straight lines. After folding up, the angles with same color circle around the same vertex. Bottom: The tetrahedron obtained via folding. There is exactly one $+1/2$ disclination on each vertex of the tetrahedron. 45

- 3.2 Morphology of nematic vesicles at different bending rigidities. Left: The local Frank (a)–(c), (g) and bending (d)–(f), (h) energy contour plots; for a case of $K_1 = K_3 = 1$, (a) and (d), $\kappa = 100.0$; (b) and (e), $\kappa = 0.3$; (c) and (f), $\kappa = 0.05$; for a case of $K_1 \neq K_3$, (g) and (h), $\kappa = 0.04$. The total Frank free energies (in units of $k_B T$) are 62.83, 59.06, 57.1, and 65.27, respectively. The normalized total bending energies (in units of $k_B T$) are 12.55, 16.0, 18.58, and 50.34, respectively. Right: Calculated asphericities of nematic vesicles as a function of the inverse bending rigidity of $1/\kappa$. The inverse triangles are for a case of $K_1 = K_3$ and the triangles are for a case of $K_1 \neq K_3$ ($K_3/K_1 \approx 2.0$). The empty circles represent locations corresponding to the morphologies of (a)(d), (b)(e), (c)(f), and (g)(h). 48
- 3.3 Comparison between experimental observations (a)–(c) and computer simulations (d)–(f). Left: Experimental results, (a) a tetrahedron-shape smectic vesicle [51]; (b) a fat tetrahedron-shape smectic vesicle [165]; (c) an ellipsoidal smectic vesicle [49]. Right: Simulation results for a case of $K_3/K_1 \approx 2.0$, (d) $\kappa = 0.04$; (e) $\kappa = 0.1$; (f) $\kappa = 0.5$. The contour plots show the distribution of the local Frank free energy. 50
- 4.1 A wall made of hydrophilic and hydrophobic materials is immersed in a liquid. The liquid interface curves up in the hydrophilic part and down in the hydrophobic part. In the transition region, the liquid profile on the wall changes smoothly. 61
- 4.2 The total energy Eq.(4.1) versus the parameter a and the dimensionless quantity Γ . The parameter a indicates the steepness of the liquid profile on the wall in the transition region. Γ controls the competition between the contact energy and the gravitational potential energy. 61

4.3	Design for generating constant mean curvature liquid menisci by controlling the pressure difference across the liquid interface through adjusting the heights h_A and h_B . Two shapes of liquid interface with vanishing mean curvature (above) and constant mean curvature (below) are shown. These shapes are generated with Surface Evolver [186].	63
4.4	Wrinkles of alternating peaks and valleys on a piece of paper redefine the metric, automatically bringing the flat paper to a saddle-like shape. (a) is excerpted from Ref.[191], and (b) is from Ref.[192] where the method to make it is described in detail.	65
4.5	A branch-like fold pattern appears on a flat paper disk by wrapping it on a negative curvature surface (left figures). The folds in the red rectangles are equivalent to removing eye-like areas as shown in the upper right figure. The buckled shape (the lower right figure; the leaf-like object therein is the removed material) of a flat disk due to an isolated fold is obtained by “closing the eye”.	67
4.6	The phase diagram of a deformed sheet on a negative curvature surface. Wrinkles on the sheet occur near the isotropic region ($\alpha/\beta \approx 1$) while folds are found in the highly anisotropic regions (α/β far from unity). The smallness of α and β as measured by the radius of the sheet guarantees that the surface is only slightly curved.	70
5.1	The geometric characterization of torus. A torus is produced by rotating the circle around the vertical axis.	76
5.2	A perturbed torus.	76
5.3	(a, b) The plot of velocity field in inside and outside fluids. (c) is the irrotational component of the velocity field in outside fluid. $\frac{\eta_i}{\eta_o} = 1, k = 1/(2r_0)$. The horizontal coordinate is r , and the vertical is z . The plot range of r for inside fluid is $r = [0, 1]$ and for outside fluid $r = [1, 20]$. $z = [0, 20]$ for both fluids.	91

5.4 The ratio of the rotational part to the full of stream functions for inside (a) and outside (b) fluids for different viscosity ratios. $kr_0 = 1/5$. Green curve: $\frac{\eta_i}{\eta_o} = 0.001$; red curve: $\frac{\eta_i}{\eta_o} = 1$; black curve: $\frac{\eta_i}{\eta_o} = 1000$. It clearly shows that vorticity field locates in the less viscous fluid. Note that the green curve in (b) is approaching one if the plot along r is extended. 95

5.5 $V_i(k)$ and $V_o(k)$ versus k for inside (a) and outside (b) fluid. $\frac{\eta_i}{\eta_o} = 1$. Minimum points exist for these two functions. 98

5.6 The growth rate of perturbation amplitude versus wavenumber kR_{20} . $kR_{20} = 2\pi/\lambda$. The radius of the torus is $R_1/R_{20} = 10$. $\frac{\eta_i}{\eta_o} = 1/30$ as in experiment [200]. The competition of dissipation rate and surface energy gives rise to the most unstable mode $kR_{20} = 0.5$, which is comparable to experimental value $kR_{20} = 0.57$ 100

5.7 The most unstable mode versus $\log_{10}^{(\eta_i/\eta_o)}$. The theoretical predictions for the most unstable modes are the dots in the figure, who are fit by smooth curves for cylindrical and toroidal cases respectively. The blue curve: for cylindrical droplets. The red curve: for toroidal droplet with $R_1/R_{20} = 10$. They are almost overlapped. The curve for the case of cylindrical liquid droplet is identical to Tomotika's [202]. Note that for toroidal interface kR_{20} can only take discrete values, since the allowed wavelengths of capillary waves on torus are quantized (see Eq.(5.5)). 101

5.8 The Laplace pressure drop versus ka . The most unstable mode occurs at the peaks. The region of $|x| > 1$ is stable. 107

6.1 Determine the values of A_p in Eq.(6.12) by fitting the boundary condition $f(\varphi)$ in Eq.(6.13). The black solid curve is $f(\varphi)$, which is the boundary condition. The dashed curve is for p_1 defined in Eq.(6.8). 116

6.2 The pressure $p(r, \alpha)$ vs. angle α at different radial distances away from the reference circle for $R_1 = 5$ mm and aspect ratio $\phi = R_1/R_2 = 1.5$. The solid black curve is the pressure distribution on the boundary $p = \sigma H$. Green curve: $r = R_1/1.5$ (boundary). Blue curve: $r = R_1/3$. Red curve: $r = R_1/10$. Dashed Black curve: $r = R_1/100$. The green curve fits the exact pressure on the boundary very well. 117

6.3 Determine the coefficient C_ν in Eq.(6.46) by fitting the boundary condition. The solid curves are the velocity field on the boundary, and the dashed curves are the velocity field derived from the stream function with $C_\nu/V = -4$. $\nu = 1$. $R_1 = 5$ mm, $R_{20} = 2$ mm. 123

6.4 The velocity field inside and outside a cross-section of a toroidal liquid droplet. The dashed semi-circle is the interface of two distinct fluids. The velocity field inside the droplet is calculated by solving the biharmonic equation. The external flow pattern is schematically plotted by imposing boundary conditions and exploiting symmetry. The mode number $\nu = 1$, $R_1 = 5$ mm and $R_{20} = 2$ mm. 124

6.5 The velocity field inside the toroidal droplet of Fig.6.4 in a comoving reference frame shrinking with the droplet. The swelling of the cross section is readily inferred. 124

6.6 (a) The vorticity $\Omega_\theta(r)/\Omega_\theta(r = R)$ versus r . Parameters: $\nu = 1$, $c_1 = 1$, $\alpha = 1$ rad, $R_1 = 5$ mm and $R = 4$ mm . The vorticity field falls to zero at the reference circle. (b) Ω_θ versus angle α for modes ν in the range $(-3, 3)$. The vorticity Ω_θ is rescaled to show different modes in the same figure. Parameters: $\phi = 5, a = 1$. Blue curve: $\nu = 0$ (vorticity vanishes). Black curve: $\nu = 1$. Brown curve: $\nu = 2$. Gray curve: $\nu = 3$. Green curve: $\nu = -1$. Red curve: $\nu = -2$. Pink curve: $\nu = -3$. Note that the number of peaks or valleys is determined by the mode number ν 126

- 6.7 The time evolution of the normalized inner droplet radius $R_{in}(t)/R_{in}(0)$ for initial aspect ratio 1.4. The theoretical result is the solid curve and the experimental data points are taken from Ref.[200]. Parameters: $R_1(0) = 3$ mm; $v_s = \sigma/\eta_o = 133$ $\mu\text{m/s}$ 128
- 6.8 Minimum energy cross-sectional shapes within a two parameter family of possible shapes (see Eq.(6.58)). The dashed curves are the unperturbed circular shapes: (a) aspect ratio 10 (thin torus) and (b) aspect ratio 2 (fat torus). 130
- 7.1 (a) A liquid droplet sitting on a rough substrate has more contact area with the substrate ($A_c > A_0$) than the same droplet on an otherwise identical flat substrate. (b) A liquid droplet partially wetting a hydrophilic substrate with inhomogeneous roughness has a smaller contact angle at the rougher end (θ_A) than at the smoother end (θ_B). 135
- 7.2 Left: a liquid droplet partially wetting a substrate with a uniaxial sinusoidally modulated roughness. Right: Schematic plot of sinusoidal grooves with wavenumber monotonically increasing in the direction orthogonal to the sinusoidal height profile. 137
- 7.3 The ratio of the effective imbibition parameter to the physical imbibition parameter versus $\Gamma = a_k^2 k^2$ for a liquid droplet partially wetting a sinusoidally modulated substrate. 138
- 7.4 A substrate etched by fractal grooves. The cross-sectional shape of the grooves is the lower half of the Koch curve, as shown in the inset. . . 139
- 8.1 The mapping from the $z > 0$ bulk space to the space outside a sphere with radius a (represented by the blue circle) via consecutive stereographic projections from a plane to a sphere. A deviation $d(z)$ is introduced to guarantee the equality of the potential on the blue spherical shell and the potential at the plane located at z 143

- 8.2 (a) The plot of the displacement field $d(z)$ for various spherical radii: $a = 0.1$ (green), $a = 1$ (red), $a = 10$ (blue), $a = 100$ (black). As $a \rightarrow \infty$, $d(z)$ is expected to vanish. (b) The plot of the strain fields $d'(z)$ for the corresponding displacement fields $d(z)$ in (a). 145
- 8.3 The potential around a charged spherical interface of unit radius in a q:q solution. The surface potentials in (a)-(d) are respectively 0.1, 1, 5, 10 measured by $q/(k_B T)$. The curves give the numerical solution to the Poisson-Boltzmann equation (black), analytical solution for weak ψ_0 (green dashed) and the solution constructed by the our method (red dots). 147
- 8.4 The ψ_G solution is applicable below the red curve in the parameter space $\{a, \psi_0\}$. On the red curve, $\delta = \epsilon = 10^{-3}$ 149
- 8.5 The comparison of the ψ_G solution (black) and the planar solution (blue) in terms of the ratio of the LHS to RHS of Eq. (8.1). The radii of the spherical interface are $a = 5(a)$ and $20(b)$. $\psi_0 = 1$ 150
- 8.6 The potential distributions ($\exp(\alpha x + \beta y)$) in the double layer corresponding to the periodic (a) and aperiodic (b) boundary conditions. $k_a = k_p = 0.5$ 150

Chapter 1

Introduction

Geometry is an important concept and tool in understanding physics as stated by d'Alembert: “geometry, which should only obey physics, when united with it sometimes commands it” [1]. The geometric approach has the advantage of intuitiveness, while the algebraic approach is more precise [2, 3, 4, 5, 6, 7]. Hua Lo-keng, a Chinese mathematician (1910-1985), once said, “numbers without shapes lack intuitiveness, shapes without numbers lose subtlety”. Physicists have the tradition of applying the geometric approach to physical systems. Newton used Euclidean geometry as the mathematical foundation of the *Mathematical Principles of Natural Philosophy*. Einstein constructed general relativity on the mathematical grounds of non-Euclidean geometry. The elegance of the geometric approach has attracted generations of physicists to apply it to various systems. As a classic example, gravity can be elegantly understood as the curvature of space according to the Einstein field equation. In the community of soft matter physics, many examples demonstrate the major role played by geometry, and various geometric models are proposed to understand the properties of condensed matter. In water-oil microemulsions, for example, a rich variety of geometric phases form, including spongelike phases of minimal surfaces and bicontinuous phases, where spontaneous curvature is a crucial parameter [8]. The Bernal model of random-close-packing of hard spheres is a useful model for understanding

the structure of a liquid (or an amorphous solid or glass) which is characterized by radial distribution functions [9].

In this thesis, we study several geometric aspects of soft matter. The topics covered can be classified into three parts. The first part deals with the geometric frustration in 2-dimensional condensed matter. We study crystalline and liquid crystalline order on curved surfaces and the geometric frustration of a planar sheet meeting a negative curvature surface. In the second part, we study the stability of toroidal liquid droplets where the geometry plays a crucial role. We also study how to realize the self-propulsion of liquid droplets on substrates by pure geometric patterning. In the third part, we study the electric double layer structures of charged spherical interfaces by constructing a geometric solution to the nonlinear Poisson-Boltzmann equation, which enables further analytical study of spherical electrostatic systems such as colloidal suspensions.

1.1 Geometric frustration in two-dimensional systems[†]

The physics of 2D condensed matter systems is a rich and mature subject [3, 9]. In the study of metallic glass, the fundamental concept of *geometric frustration* has been proposed [12, 13]. Geometric frustration refers to the geometric impossibility of establishing a preferred local order everywhere in space. Farges and coworkers were the first to show in experiments and computer simulations that long range translational order is forbidden in the structure of the aggregation of icosahedral building blocks, because icosahedra don't fill the three-dimensional Euclidean space [14, 15, 16]. How to describe the spatial disorder? Inspired by the fact that regular tetrahedra can regularly tile the three-dimensional sphere \mathbb{S}^3 (they don't fill the three-dimensional Euclidean space though), Sadoc and Kleman first observed that a number

[†] In preparing for this part, we refer to the review paper [10] and the doctoral theses of L. Giomi [1] and H. Shin [11].

of continuous random lattices can be regarded as mappings of ordered lattices into spaces of constant curvature onto \mathbb{R}^3 [17]. This idea finally leads to a new approach to spatial disorder based on the interplay between order and geometry in the work of Sadoc and Mosseri [18], Steinhardt et al. [19], Nelson [20] and Kleman [21]. Recent simulation in three dimensional systems reveals the strong coupling between defect structure and dynamics (see the systematic study in Ref.[22]).

In-plane order on two-dimensional manifolds has been subject of extensive research since the discovery of the ordered phases L_β and P_β of phospholipidic membranes [4]. Much work has been done in elucidating the intimate relation between in-plane order and the geometry of the underlying substrate in the pioneering papers of Nelson and Peliti [23], Berezinskii [24], Kosterlitz and Thouless [25, 26, 27]. Gaussian curvature introduces topological defects that are energetically prohibitive in planar systems. Order on curved surfaces has been extensively studied theoretically and experimentally, including spherical crystals [28, 29, 30], paraboloidal crystals [31], toroidal hexatics [32], crystalline order over a Gaussian bump [33, 34] and a capillary bridge [35, 36], spherical nematics [37, 38] and columnar/smectic textures on curved substrates [39, 40, 41]. In Chapter 2, we will study theoretically crystalline order on capillary bridges. These studies suggest a promising strategy for designing mesomolecules whose valencies can be controlled by functionalization of defect sites or by engineering the underlying substrate curvature itself [42, 43, 44, 45, 46, 47, 48]. On the other hand, both experiments and theory show that topological defects on a flexible substrate can significantly deform their shapes. For example, a rich variety of morphologies of liquid crystal vesicles formed from diblock copolymers are observed in a recent experiments [49, 50, 51]. The origin of these shapes can be understood in terms of the in-plane crystalline and liquid crystal orders. For example, it has been theoretically shown that defects in nematic membranes can buckle into pseudospheres [52], and a vortex or anti-vortex defect in the phase of the quantum order distorts the membrane metric into a negative conical singularity surface [53]. In Chapter 3, we

will study theoretically the morphology of the nematic and smectic vesicles that have been recently synthesized [49, 54]. These studies deepen our understanding of the origin of shapes of living and manufactured membranes and other condensed matter systems.

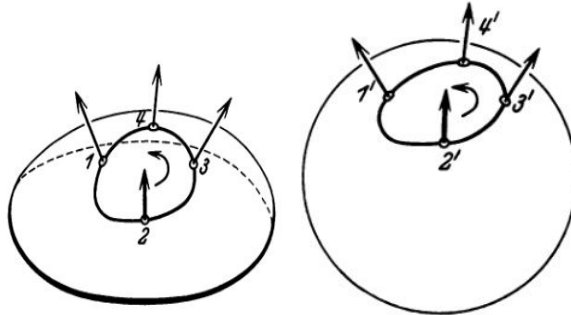


Figure 1.1: The spherical image of a surface (left) is obtained by parallel moving all unit normal vectors on that surface (left) onto the unit sphere (right).

In the above discussion of the interplay of order and geometry, Gaussian curvature can be regarded as equivalent to topological charges. An alternative interpretation of Gaussian curvature is the redefinition of metric. This may be seen from the geometric interpretation of Gaussian curvature: $K_G = \lim_{\Delta A \rightarrow 0} \frac{\Delta A_s}{\Delta A}$. ΔA_s and ΔA are the area elements on the spherical image and on the surface. The spherical image of a surface is illustrated in Fig.1.1. Around a hyperbolic point where the Gaussian curvature is negative, the contour of ΔA_s is traversed in a direction opposite to that of ΔA . For convenience in calculation, the above expression for Gaussian curvature can also be written as the limiting difference between the area of a geodesic disk of radius r and a disk in the plane $K_G = \lim_{r \rightarrow 0^+} 12 \frac{\pi r^2 - A(r)}{\pi r^4}$.

According to the geometric meaning of Gaussian curvature, geometric frustration occurs in attaching a planar sheet onto a surface of nonzero Gaussian curvature. The geometric incompatibility of a planar sheet and a curved substrate leads to the emergence of ridges. It is a process of the spontaneous condensation of energy into a small subset of the available volume in order to reduce the energy of the system

[55]. Recently the frustration of a thin circular elastic sheet of ~ 100 nm size covering the tip of a spherical droplet has been studied [56]. Fine radial wrinkles at the edge of the sheet become unstable to a few localized folds as the radius of the spherical droplet decreases. The wrinkle-fold transition is analogous to the dislocation (or pleat)-disclination (or scar) transition in crystalline order on a capillary bridge as the curvature is increased [35, 57, 58]. The structure of topological defects on positive and negative curvature surfaces are fundamentally different [59]. This suggests a distinct wrinkle/fold structure on a flat sheet when attached to a negative curvature surface; the edge of the sheet is stretched as opposed to being compressed on a spherical geometry. A completely different frustration pattern on the planar sheet is thus expected. In Chapter 4, we study what happens when a planar sheet is placed on a negative curvature surface.

1.2 Geometry in liquid droplets

Liquid droplets are ubiquitous and are multidisciplinary research objects studied in physics, chemistry, biology, pharmacy, food and meteorology [60]. The rich behavior of a liquid droplet in various circumstances is fascinating and intriguing. For example, the problem of the formation of drops, as first mentioned in a book by Mariotte (1686), remains far from exhausted after more than 300 years of scientific research [61]. There are various methods to generate droplets [62] that can be divided into two classes: condensation of vapor and disintegration of bulk fluids. The mechanism of the latter method is the Rayleigh instability, although other methods are used, such as cutting a liquid jet by air bubbles for a better control of the size of droplets [63]. The size of the generated droplets ranges from micro to millimeters. The typical size of droplets in a spray ranges from $10 - 100 \mu\text{m}$, and the size of a rain drop is about $5 - 6$ mm.

The study of liquid droplets is of tremendous technological importance in mixing, spraying and chemical processing which leads to applications such as ink-jet printing,

fiber spinning, and microfluidic technology (e.g., miniature bio-chemical reactions on a chip) and self-assembly technology [62, 64, 65, 66]. It is interesting to mention a liquid droplet's capability of self-assembly. The idea originates from a spilled drop of coffee drying on a solid table [67, 68]. The evaporation induces an outward flow inside a coffee droplet sitting on a solid table. The flow brings virtually all the dispersed coffee solids to the edge. The self-assembly technology based on the coffee ring effect has been used for the assembly of nanoparticles, diblock copolymers and even DNA chains [69]. Liquid droplets also attract theorists' attention. For example, the local singular behavior at the initial stage of the snap-off has been intensively studied as a classical finite-time singularity problem [70, 71, 72, 73, 74, 75, 76]. The study of liquid droplets can shed light on other physical and biological systems. For example, the snap-off of liquid droplet is used to understand atom fission [77], while the fusion of cells and the self-assembly of immiscible tissues in embryonic morphogenesis can be analogous to the coalescence of droplets [78]. Furthermore, the study of the impact of liquid droplets may also provide insights into the formation of planets as a result of collision of smaller clusters according to the prevailing protoplanet theory [79].

Our understanding of the liquid droplet system benefits greatly from the concept of surface tension introduced two hundred years by Johann Andreas von Segner, a Hungarian mathematician [80]. In terms of surface tension, much of the behavior of liquid droplets, including statics and dynamics, in different environments, is well understood [60, 65, 81]. Due to surface tension, the surface of a droplet is like an elastic skin and a liquid droplet is perfectly spherical in its free state. The geometry influences the physics of liquid droplets via the Laplace pressure $\Delta P = 2\sigma H$, where the mean curvature $2H = \frac{1}{R_1} + \frac{1}{R_2}$. R_1 and R_2 are the two principal radii of curvature. ΔP is the pressure difference across the liquid interface due to surface tension and mean curvature. For small droplets measured by the capillary length $\sqrt{\frac{\sigma}{\rho g}}$ which is of interest for us, the surface tension dominates over gravity. According to the Navier-Stokes equation, the uneven distribution of Laplace pressure (without other forces)

will induce a flow. The problem of flows in liquid droplets represents the class of free boundary problems in fluid mechanics [82]. In Chapter 5 and 6, we show that the surface tension driven flow is responsible for the Rayleigh and shrinking instabilities of toroidal liquid droplets [83]*. We also demonstrate in Chapter 7 that this flow can be used to drive a liquid droplet on a substrate with pure spatially varying topography [84].

1.3 Poisson-Boltzmann theory and beyond

Colloidal particles, polymers and membranes all carry charges in an aqueous environment [85, 86]. For example, DNA can carry a linear charge density of as high as one unit charge every 0.17 nm [87]. Note that the persistence length of DNA is about 30 – 50 nm [87]. Colloidal particles in solution can be charged as highly as $0.1 - 1 \text{ e/nm}^2$ by chemically decorating their surfaces with dissociable groups such as sulfate or carboxyl groups which easily release ions upon contact with water [88]. The electrostatic interactions can be both attractive, leading to association, and repulsive resulting in dispersion. They provide one of the basic organizing principles in both colloidal suspensions and living biological systems. On the other hand, thermal fluctuations influence the distribution of free ions in solution. The behavior of charged matter is therefore dominated by the interplay of thermal fluctuations and long-range electrostatic effects on different length and time scales, leading to complicated phase diagrams [89].

Solutions of charged objects are tremendously complicated physical systems. Even the standard solvent itself - water- already poses formidable problems. In order to make some predictions about such systems, one may utilize the fact that many interesting features of electrolytes are ultimately a consequence of the presence of charges. Therefore, a good treatment of the electrostatics and crude approximations

* It is interesting to note that dolphins can make toroidal bubbles in water.

for other factors are expected to unveil the behavior of these systems [89] (the lecture by Deserno and Holm). Any quantum mechanical effects are ignored and the solvent is treated as a dielectric continuum. The “dielectric approximation” actually works surprisingly well [89] (the lecture by Jonsson and Wennerstrom).

The Poisson-Boltzmann (PB) equation is an important tool for understanding charged objects in solution. Despite its mean field nature and its limitation in dealing with multivalent ionic solution where ion-ion correlations are important, it has all the length and energy scales, and provides a first step and qualitative picture of electrostatic phenomena in solutions. The derivation of the PB equation is rather straightforward [90]. Consider a solution in contact with an electrolyte reservoir of fixed concentration n_0 . The coions and counterions are in thermal equilibrium with the reservoir. For simplicity we assume only one type of coion and one type of counterion with number densities $n_{\pm}(\vec{r})$. The total charge density is $\rho(\vec{r}) = ez_+n_+(\vec{r}) + ez_-n_-(\vec{r})$ where z_+ (z_-) is the valence of the coions (counterions) and the elementary charge $e > 0$. The PB equation is derived from the following two equations. On one hand, the potential $\psi(\vec{r})$ is determined by the charge distribution, i.e.,

$$\Delta\psi(\vec{r}) = -\frac{4\pi}{\epsilon}\rho(\vec{r}), \quad (1.1)$$

where ϵ is the dielectric constant of the aqueous solution. On the other hand, thermal equilibrium requires that the chemical potential μ_i of the i -th ion $\mu_i = ez_i\psi + T \ln n_i$ is constant [91]. This leads to the Boltzmann distribution

$$n_i = n_0^i e^{-\frac{ez_i\psi}{k_B T}}. \quad (1.2)$$

Combining Eq.(1.2) and (1.1), we obtain the Poisson-Boltzmann equation which determines the potential ψ self-consistently:

$$\Delta\psi(\vec{r}) = -\frac{4\pi}{\epsilon}(z_+n_0^{(+)}e^{-\frac{ez_+\psi(\vec{r})}{k_B T}} + z_-n_0^{(-)}e^{-\frac{ez_-\psi(\vec{r})}{k_B T}}). \quad (1.3)$$

In particular, for a 1:1 electrolyte reservoir (e.g., Na^+Cl^-), $n_0^{(\pm)} = n_0$ and the PB equation becomes

$$\Delta\psi(\vec{r}) = -\frac{8\pi en_0}{\epsilon} \sinh\left(\frac{e\psi(\vec{r})}{k_B T}\right). \quad (1.4)$$

Working in the natural units of potential $k_B T/q$ (q is the absolute value of the charge of ions) and Debye length $\kappa^{-1} = \sqrt{\epsilon k_B T / (8\pi n q^2)}$, the dimensionless Eq.(1.4) becomes

$$\Delta\psi = \sinh \psi. \quad (1.5)$$

There is a subtlety regarding the potential in the derivation for the PB equation. In the electrostatic Poisson equation, the potential $\psi(\vec{r})$ is due to all ions in the system, while in the Boltzmann distribution, the $\psi(\vec{r})$ is the potential at \vec{r} due to all other ions except the one at \vec{r} . In the mean field level, they are treated as equal. Furthermore, it is worth mentioning that the PB equation is compatible with the principle of linear superposition in electrostatics, although it is nonlinear in the potential. An inconsistency does appear when the PB equation is applied to a system where the macroion is identical to some small ion. The consequence of this inconsistency is eliminated when the PB equation is linearized (see the lecture of Jonsson and Wennerstrom in Ref.[89]and the textbook [92]).

In the derivation of the PB equation we make the following assumptions [93]: (i) electrolyte ions are treated as point charges in the electrostatic Poisson equation; (ii) ion-ion correlations are neglected in the Boltzmann equation; (iii) the solvent is treated as a structureless dielectric continuum carrying a uniform dielectric permittivity ϵ ; and (iv) charges on the particle surface are smeared out to give a continuum distribution. An alternative derivation of the PB equation from variational mean field clearly shows that the neglect of ion-ion correlations leads to the PB equation [89] (the lecture by Deserno and Holm and that by Moreira and Nets). The crucial assumption is to replace the N -particle distribution function by a product of N identical one-particle distribution functions. There actually *exists* a density functional which gives the correct free energy according to an important theorem originally due to Hohenberg and Kohn, although it does not specify it. Various local [94, 95, 96, 97] and nonlocal [98, 99, 100] corrections to the PB functional have been suggested. Despite these assumptions, it has been shown in numerous studies that the Poisson-Boltzmann theory is actually quite reliable, especially when applied to problems of

electrostatic interaction of colloidal particles when the surface charge is low [85] and to electrokinetic phenomena [86].

By linearizing the PB equation, Debye and Hückel showed the electrostatic energy of a 1:1 electrolyte solution to go as $E \sim n^{3/2}$ and derived the osmotic pressure [101]. The power 3/2 explains why a virial expansion must fail. An alternative derivation of the electrostatic energy of an electrolyte solution in terms of the correlation function is given in [91]. One significance of the work of Debye and Hückel is the introduction of the Debye length in place of the length scale $(V/N)^{1/3}$, where V is the volume of the system and N is the number of ions. The Debye length takes into consideration thermal fluctuations and can characterize the screening effect of free ions in solution. It has become an important (qualitative) analysis tool since its proposal. In addition, the DH approximation is suitable for the study of flexible molecules due to its simplicity [87].

Debye-Hückel theory works very well for 1:1 electrolytes. However, perceptible deviations occurs for asymmetric electrolytes (the lecture by Kjellander in [89]). The cell model has been proposed to attempt to turn this situation into an advantage. In the highly asymmetric case, a charged macromolecule is surrounded by small counterions. The total solution is therefore partitioned into cells, each containing one macroion. These cells have the same volume and are neutral in charge. Therefore the electrostatic interaction between cells may be ignored. The cell model reduces a many-body system to a one-body problem; the macroions are decoupled. The lecture by Deserno and Holm in Ref.[89] gives detailed introduction to the cell model.

By solving the potential for a planar system from the PB equation, it is found that the counter-ion density is much bigger than the co-ions near the wall. An electric double layer (EDL) is created, one layer is represented by the charged diffuse surface and the other by the excess of the opposite charge extending into the solution (Ref. [102, 103, 104]. See also p6 of Ref.[105] for the history of the EDL theory). Within the Gouy-Chapman model the finite dimensions of the ions are neglected. In more

concentrated electrolyte solutions theory leads to unrealistically high concentrations of counterions near the surface [85]. Therefore Stern [105] tried to alter the model with the division of ions into two populations. One population is considered as a layer of ions adsorbed on the surface and resides close to the charged surface (Stern-layer), while the other population is described as in Gouy-Chapman model. One may refer to Ref.[106] and [107] for recent development of the PB theory taking into consideration ion size.

The ion-ion correlation leads to electrostatic phenomena that is beyond the PB theory. It is quite often observed that multi-valent atomic ions have disastrous effects on living species. This is related to the fact that the ion-ion correlation effect is more prominent in di- and tri-valent ions, which can cause precipitation and coagulation in many colloidal systems. One example is the precipitation of soap by calcium and magnesium ions. As another example, divalent ions like Ca^{++} in some cases induce an attractive interaction between membranes, which may be attributed to the formed structure of ions in the proximity of the charge surfaces (up to a few angstroms away) [90]. Another curious finding is that the electrophoretic mobility of a highly charged colloidal particle can be reversed, if the suspension contains multivalent counterions [108]. The lecture by Jonsson and Wennerstrom in Ref. [89] gives a nice introduction to the ion-ion correlation from theory to experiment. The first clear experimental demonstration of ion-ion correlation was reported in Ref.[109, 110]. Ion-ion correlation can induce like-charge attraction. Its physical origins can be the bridging effect by polyelectrolytes (the lecture by Jonsson and Wennerstrom in [89]) and the fluctuation of ions [111, 112, 113]. The ion-ion induced attraction is typically bigger than the van der Waals interaction, and is independent of chemical details (e.g., the chemical nature of ions). Experimentally it is hard to measure the ion-ion correlation attraction force. The ion-ion correlation effect can be characterized by two dimensionless parameters [114]: $K_1 = \frac{a}{l_B} = \frac{a\epsilon T}{z^2 e^2}$ and $K_2 = \frac{l_B}{\lambda_{GC}} = \frac{\sigma z^3 e^3}{(\epsilon T)^2}$, where a is the size of the system, the Bjerrum length $l_B = \frac{(ze)^2/\epsilon}{T}$, the Gouy-Chapman length $l_{GC} = \frac{e}{z\sigma l_B}$ and σ

is the surface charge density. The ion-ion correlation effect becomes more significant for smaller K_1 and bigger K_2 .

In recent years, theories taking into account the discreteness of the charges and correlations have been developed [115, 116]. A common approach to deal with the nonlinearity, while retaining the simplicity of Debye-Hückel theory, is to apply Manning theory [87]. Despite theoretical objections, Manning theory has proved useful as a simple way to calculate certain ionic effects, for example, colligative properties, at least in specific cases (see a series papers by Manning [117, 118] and a comment paper by [119]). The lecture by Deserno and Holm in Ref. [89] gives an outlook going beyond PB theory by the methods of field theories, integral equation theories and scaling theory and simulation.

In Chapter 8, we study the electric double layer structure about charged spherical interfaces using the PB equation. We derive a formally simple approximate analytical solution to the Poisson-Boltzmann equation for the spherical system *via a geometric mapping*. Its regime of applicability in the parameter space of the spherical radius and the surface potential is determined, and its superiority over the linearized solution is demonstrated. In comparison to the algebraic method, the derivation of the ψ_G solution via the geometric mapping not only reduces the complexity of algebraic calculations, but also reveals how the spherical geometry modifies the equipotential surfaces of a planar system. In addition, the analogy between an electric double layer system and capillary deformation is found [120]. It allows the use of well-developed methods for the calculation of electrostatic interactions in DLVO (Derjaguin-Landau-Verwey-Overbeek) theory in less well-studied lateral capillary interactions between particles adsorbed at a liquid-fluid interface [120].

Chapter 2

Crystalline order on catenoidal capillary bridges

2.1 Introduction

2.1.1 Crystalline order and Euler's theorem

Two-dimensional crystalline order can be realized on a plane, as a plane can be tessellated by hexagons. However, two dimensional spherical crystals composed of pure hexagons can never be realized according to Euler's theorem [2], which states that

$$V - E + F = 2 \tag{2.1}$$

for any polyhedron, where V , E and F are the number of vertices, edges and faces of the polyhedron. One can check that twelve pentagons have to be introduced to construct a 2-dimensional spherical crystal; a football is an excellent example. Here the pentagons are defects (disclinations) in the hexagonal crystal lattice. One can further examine that 5-7 pairs (dislocations) are allowed on a planar two-dimensional crystal. From a planar to a spherical geometry, the crystalline order changes correspondingly. Reversely, by introducing a pentagon or heptagon on a two-dimensional

planar crystal, it will be buckled to reduce the in-plane strain energy and the Gaussian curvature changes [3]. These facts imply the intimate relation between crystalline order and geometry [3, 10].

The topology of the surface on which crystalline order lives imposes *global* constraint for the property of topological defects. A topological charge can be attributed to a disclination whose value is defined as the departure from the ideal coordination number of a two-dimensional planar crystal lattice $q_i = 6 - z_i$, with z_i the coordination number of the lattice point i . So Euler's theorem is written as

$$Q = \sum_i q_i = 6\chi. \quad (2.2)$$

χ is the Euler characteristic. $\chi = 0$ for a cylinder and $\chi = 2$ for a sphere. It explains why we need twelve pentagons on a 2-dimensional spherical crystal. In fact, there can be many defects on a sphere as long as their total topological charge is 12. In addition to the topological constraint, the geometry of the surface can also influence crystalline order. For example, by increasing the radius of a sphere, isolated disclinations in the crystalline order evolves to scars with the total topological charge conserved [121].

2.1.2 Background

Two-dimensional ordered phases of matter on spatially curved surfaces have several features not found in the corresponding phase for planar or flat space systems [10]. For crystalline order on surfaces of spherical topology where disclination defects are required by the topology itself, Gaussian curvature can drive the sprouting of disclination defects from point-like structures to linear grain boundary scars which freely terminate in the crystal [28, 29, 121, 122]. Even for surfaces such as the torus which admit completely defect-free crystalline lattices, the energetics in the presence of Gaussian curvature can favor the appearance of isolated disclination defects in the ground state [123, 124]. For the axisymmetric torus with aspect ratio between 4 and 10, isolated 5-fold disclinations appear near the line of maximal positive Gaussian cur-

vature on the outside and isolated 7-fold disclinations appear near the line of maximal negative Gaussian curvature on the inside [125]. The ground states in these systems are thus distinguished by a defect structure that would be energetically prohibitive in flat space. It is certainly worthwhile to explore as many settings as possible in which there are qualitative changes in the fundamental structure of the ground state, within a given class of order, purely as a consequence of spatial curvature.

The richest confluence of theoretical and experimental ideas in the area of curved two-dimensional phases of matter has been in colloidal emulsion physics in which colloidal particles self-organize at the interface of two distinct liquids, either in particle-stabilized (Pickering) emulsions [126, 127] or charge-stabilized emulsions [128, 129]. Two-dimensional (thin-shell) spherical crystals form at the surface of droplets held almost perfectly round by surface tension. The ordered configurations of particles may be imaged with confocal microscopy and the particles manipulated with optical tweezers [121, 130, 131]. Macroscopic examples of crystalline order on variable positive Gaussian curvature surfaces have been constructed by forming a soap bubble raft on a spinning liquid [132] and the nature of the order has been analyzed theoretically [133].

Glassy liquids on negative Gaussian curvature manifolds have also received considerable attention [134, 135, 136, 137, 138]. The simplest such manifold conceptually is the constant (negative) curvature hyperbolic plane H^2 and it even appears that the hyperbolic plane can be isometrically embedded as a complete subset of Euclidean 3-space, although not differentiably [139]. Physical realizations of negative Gaussian curvature manifolds in condensed matter physics will almost always have variable Gaussian curvature. The inner wall of the axisymmetric torus ($S^1 \times S^1$) has integrated Gaussian curvature equal to -4π , balancing an equal and opposite integrated Gaussian curvature on the outer wall. This is responsible for the novel ground states noted above. Gaussian bumps have regions of both positive and negative Gaussian curvature and the minimal-type surfaces found in bicontinuous phases of amphiphilic

bilayers have spatially extended variable Gaussian curvature that is negative on average [140].

Recently crystalline particle arrays on variable Gaussian curvature surfaces has been studied by assembling poly(methyl methacrylate) (PMMA) particles ($\sim 2 \mu m$) on capillary bridges formed by glycerol in bulk oil spanning two flat parallel plates [35]. The particles interact via a repulsive screened Coulomb interaction. Configurations may be imaged by confocal microscopy and even manipulated with laser tweezers. The interface between the inner fluid of the capillary bridge and the outer bulk fluid is a surface of revolution with a constant mean curvature (CMC) determined by the pressure difference between the two fluids [60, 141]. Capillary bridges minimize the surface area at fixed volume and perimeter and appear in the classical work of Delaunay [142, 143]. The value of the mean curvature and hence the underlying surface may be changed by varying the spacing between the plates.

In this Chapter, we analyze the geometry of capillary bridges observed in experiment and theoretically study the crystalline order on capillary bridge in the frame of continuum elasticity theory [23, 28]. The threshold aspect ratio for the appearance of isolated disclinations is found and the optimal positions for dislocations determined. We also discuss the transition from isolated disclinations to scars as particle number and aspect ratio are varied.

2.2 Geometry of capillary bridges

A liquid droplet between two plates forms a capillary bridge by minimizing the surface area if its size is smaller than capillary length $l_c = \sqrt{\frac{\sigma}{\rho g}}$. A capillary bridge plays essential role in adhesion, antifoaming, repelling coffee-ring effect, understanding the attractive hydrophobic force and so on [68, 144, 145].

2.2.1 A capillary bridge is a CMC surface

In what follows, we will prove that a capillary bridge is a constant mean curvature (CMC) surface.

Consider a liquid droplet of fixed volume with arbitrary shape. Following [146], we define a function $\phi(\vec{x})$ in the three dimensional Euclidean space \mathbb{E}^3 . Let the surface of interest, Γ , be represented by the zero level set of $\phi(\vec{x})$, i.e., $\phi(\vec{x}) = 0$. The unit normal vector is *defined* to be

$$\vec{n} = \frac{\nabla\phi}{|\nabla\phi|}. \quad (2.3)$$

$\phi(\vec{x}) = V_i$ gives contours of the same “electrostatic potential” V_i . The contour of $V_i = 0$ is the shape of the surface concerned. The direction of the gradient of ϕ on this contour (the direction of the “electric field”) is perpendicular to the contour, which is the direction of the normal vector. Note that the definition of the normal vector for an abstract surface requires extra information of how the surface is shaped in the higher dimension space into which it is embedded.

The area of the surface $A[\phi(\vec{x})]$ of fixed volume $f[\phi(\vec{x})] = f_0$ can be minimized by the method of Lagrange multipliers. The action is defined as

$$L = A[\phi] + \lambda(f[\phi] - f_0). \quad (2.4)$$

Its variations with respect to the field ϕ and λ lead to

$$\delta L = \delta A + \lambda \delta f = 0 \quad (2.5)$$

and

$$f[\phi] - f_0 = 0. \quad (2.6)$$

In order to calculate Eq.(2.5), we need to calculate δA and δf respectively. By using the equality

$$\int_{\Gamma} p[\phi] dS = \int_{\Omega} \delta[\phi] p[\phi] |\nabla\phi| dV, \quad (2.7)$$

we finally have

$$\delta A = - \int_{\Gamma} \nabla \cdot \vec{n} \frac{\delta \phi}{|\nabla \phi|} dS, \quad (2.8)$$

and

$$\delta f = - \int_{\Gamma} \frac{\delta \phi}{|\nabla \phi|} dS. \quad (2.9)$$

\vec{n} is the outward unit normal vector on surface Γ . $\delta[\phi]$ and $\delta\phi$ are distinguished as the Dirac delta function and the variation of ϕ . By inserting the expressions for δA and δf into Eq.(2.4), we have

$$\delta L = - \int_{\Gamma} (\nabla \cdot \vec{n} + \lambda) \frac{\delta \phi}{|\nabla \phi|} dS + \delta \lambda (f[\phi] - f_0), \quad (2.10)$$

which leads to the locally stable configurations satisfying

$$\nabla \cdot \vec{n} + \lambda = 0 \quad (2.11)$$

on the surface Γ and

$$f[\phi] - f_0 = 0. \quad (2.12)$$

Since mean curvature $2H = \nabla \cdot \vec{n}$, Eq.(2.11) states that all the locally stable configurations are CMC surfaces. Minimal surfaces with vanishing mean curvature is a special case.

The CMC shape of capillary bridges is also understood in terms of the Laplace pressure. Since the Laplace pressure is proportional to mean curvature, the spatially varying mean curvature will induce a flow inside a capillary bridge leading to a constant mean curvature surface.

2.2.2 The solutions to the shape equation

The shape equation of a capillary bridge as a CMC surface represented by $r(z)$ is

$$H \equiv \frac{1}{R_1} + \frac{1}{R_2} = \frac{-r''}{(1+r'^2)^{3/2}} + \frac{1}{r\sqrt{1+r'^2}} = \text{const.} \quad (2.13)$$

z-axis is the axial of rotational symmetry. Since

$$\left(\frac{1}{\sqrt{1+r'^2}}\right)' = -\frac{r'r''}{(1+r'^2)^{3/2}}, \quad (2.14)$$

the first integration of Eq.(2.13) with respect to z yields

$$\frac{r}{\sqrt{1+r'^2}} = \frac{H}{2}r^2 + c. \quad (2.15)$$

The solution of a minimal surface with vanishing mean curvature is immediately obtained by letting $H = 0$ in Eq.(2.15):

$$r(z) = c \cosh \frac{z}{c}. \quad (2.16)$$

It is recognized as a catenoid. Its parameterized representation is

$$\vec{x}(u, v) = \begin{pmatrix} c \cosh\left(\frac{v}{c}\right) \cos u \\ c \cosh\left(\frac{v}{c}\right) \sin u \\ v \end{pmatrix}.$$

$u \in [0, 2\pi)$ and $v \in (-\infty, \infty)$. The single parameter c controls the shape of a catenoid. The waist (minimum cross section) of a catenoid located on the $z = 0$ plane has radius c . $u = \text{const}$ defines the meridians of surface and $v = \text{const}$ defines the latitude lines. $u \in [0, 2\pi), v \in [-v_m, v_m]$ for capillary bridge between two plates with reflection symmetry about its waist. The basis vectors are $\vec{e}_1 \equiv \vec{e}_u$ and $\vec{e}_2 \equiv \vec{e}_v$.

The metric of a catenoid is defined by

$$ds^2 = c^2 \cosh^2\left(\frac{v}{c}\right) du^2 + \cosh^2\left(\frac{v}{c}\right) dv^2, \quad (2.17)$$

from which we have the nonzero components of the metric tensor as

$$g_{uu} = c^2 \cosh^2\left(\frac{v}{c}\right), \quad (2.18)$$

and

$$g_{vv} = \cosh^2\left(\frac{v}{c}\right). \quad (2.19)$$

The Gaussian curvature of a catenoid is derived as

$$K = -\frac{r''}{r(1+r'^2)^2} = -\frac{1}{c^2} \operatorname{sech}^4\left(\frac{v}{c}\right) = -\frac{1}{g}, \quad (2.20)$$

from [147]

$$K \equiv \frac{1}{R_1} \frac{1}{R_2} = \frac{b}{g}, \quad (2.21)$$

in which

$$b_{ij} = \vec{e}_{i,j} \cdot \hat{n}, \quad (2.22)$$

$$\vec{e}_i = \frac{\partial \vec{x}}{\partial q^i}. \quad (2.23)$$

b is the determinant of b_{ij} . The metric completely determines the Gaussian curvature as expected, because the Gaussian curvature is an intrinsic property of surface. For the part of a catenoid between $z \in [-v_m, v_m]$, the integral of the Gaussian curvature is:

$$\int K dA = -4\pi \tanh\left(\frac{v_m}{c}\right), \quad (2.24)$$

and the surface area is

$$A = \pi c \left(2v_m + c \sinh\left(\frac{2v_m}{c}\right)\right) = \frac{2V}{c}, \quad (2.25)$$

where V is the volume. The nice relation between the area and the volume is seen $V = \frac{1}{2}Ac$. For comparison, we give the volume-area relation of a cylinder $V = \frac{1}{4\pi} \frac{A^2}{h}$ where h is the height of a cylinder. The former one is linear while the latter one is a square law. The plot of $A(c)$ is given in Fig.2.1. $A(c)$ reaches maximum at $c = 0.55$.

For a general CMC surface with nonzero mean curvature, the solution to Eq.(2.15) is [148]

$$x(t) = \alpha + \gamma(E(\theta, t) + F(\theta, t)\cos\theta) \quad (2.26)$$

and

$$y(t) = \gamma\Delta(\theta, t), \quad (2.27)$$

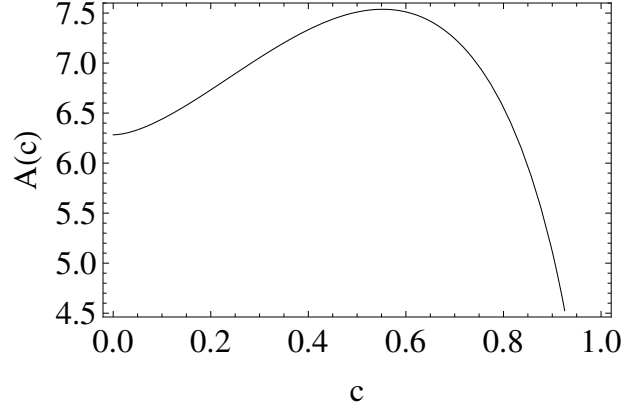


Figure 2.1: The surface area of a catenoid versus its aspect ratio c . The radius of the boundary circular section is $R = 1$.

where the x-axis is the axis of revolution, t is the parameter of the profile curve and $H = -\lambda$.

$$\lambda = -\frac{2}{\gamma(1 + \cos \theta)}, \quad (2.28)$$

$$E(\theta, t) = \int_0^t \Delta(\theta, \tilde{t}) d\tilde{t}, \quad (2.29)$$

$$F(\theta, t) = \int_0^t \frac{1}{\Delta(\theta, \tilde{t})} d\tilde{t} \quad (2.30)$$

and

$$\Delta(\theta, t) = \sqrt{1 - \sin^2 \theta \sin^2 t}. \quad (2.31)$$

γ acts as a scale factor.

The profile curves generated are π periodic in t : having maxima at $t = k\pi$ and minima at $t = (k + 1/2)\pi$ for integer k . The value of θ affects the shape of the profile curve: it forms unduloid for $\theta \in [0, \pi/2)$; nodoid for $\theta \in (\pi/2, \pi)$; and semi-circle with centers and cusps on x-axis for $\theta = \pi$. The shape of either unduloid or nodoid can be parameterized as

$$\vec{x}(u, t) = \begin{pmatrix} \gamma \Delta(\theta, t) \cos u \\ \gamma \Delta(\theta, t) \sin u \\ \alpha + \gamma(E(\theta, t) + F(\theta, t) \cos \theta) \end{pmatrix}.$$

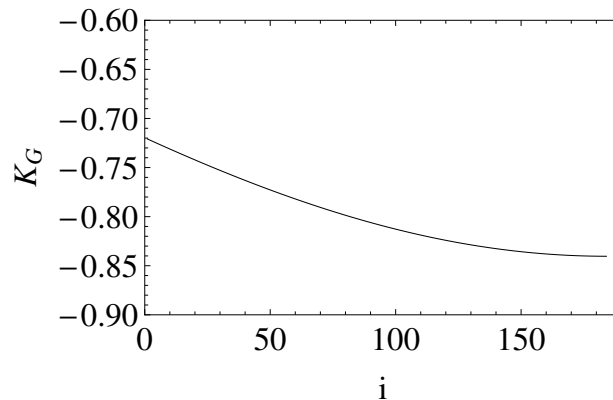


Figure 2.2: The distribution of Gaussian curvature on the capillary bridge in Fig.4i in Ref. [35] versus i . $t = t_0 + i * dt, dt = 10^{-5}\pi$. i increases from 0 on the waist of the capillary bridge towards its ends.

$t \in [t_0, t_1]$. $u \in [0, 2\pi)$. The nonzero components of the metric tensor are

$$g_{tt} = \left(\frac{\gamma \sin t \cos t \sin^2 \theta}{\Delta(\theta, t)} \right)^2 + \gamma^2 \left(\Delta(\theta, t) + \frac{\cos \theta}{\Delta(\theta, t)} \right)^2, \quad (2.32)$$

$$g_{uu} = \gamma^2 \Delta(\theta, t)^2 \quad (2.33)$$

The Gaussian curvature can be calculated by using the parametric form of Eq.(2.20). For the shape of Fig.4 i in Ref. [35], the distribution of Gaussian curvature is shown Fig.2.2. We see that the magnitude of Gaussian curvature reaches maximum at the waist.

In experiment [35], by pulling a capillary bridge, a series of shapes are obtained. In what follows, we will show that these shapes are unduloids/nodoids. Since the waist of the experimental profile is smaller than the contact disk, we consider interfaces that are symmetric about the minimum point $t = \pi/2$. The free parameters are t_0, γ, θ . t_0 is the value of the parameter t at the end of the profile. The latter two gives the scale and the shape of the profile respectively. We need three constraints to fix these three free parameters which are the volume of the capillary bridge vol , the radius R of the contact disk and the distance h between the two plates. These constraints are

formulated as:

$$V = 2\pi \int_{t_0}^{\pi/2} y^2(t) dx, \quad (2.34)$$

$$R = \gamma \Delta(\theta, t_0), \quad (2.35)$$

and

$$h = 2\gamma(E(\theta, \pi/2) - E(\theta, t_0) + \cos\theta(F(\theta, \pi/2) - F(\theta, t_0))). \quad (2.36)$$

We numerically solve these equations. Let the second and third constraints to be satisfied strictly, and then by minimizing $\epsilon \equiv |V - \pi R^2 h_0|/(\pi R^2 h_0)$, in which h_0 is the initial distance of two plates before stretching. The values of the three free parameters can be obtained. The results in comparison with experiment (Fig.4 in Ref. [35]) are as follows:

$h(h_0 = 0.55)$	H	t_0	θ	c/c_{exp}	γ	ϵ
0.56	0.56	1.50	1.169	0.986/n.a.	2.868	$3.2 * 10^{-6}$
0.63	-1.20	1.75	1.930	0.902/0.854	2.909	$4.5 * 10^{-6}$
0.82	-1.51	1.92	1.938	0.742/0.784	2.344	$1.5 * 10^{-8}$
0.92	-1.24	1.91	1.872	0.678/0.687	2.590	$1.9 * 10^{-9}$

The mean curvature in this table is scaled by that of a reference cylinder whose radius is that of the contact disk. The values of h is measured from the images of capillary bridges. From the change of the values of θ , the shape of capillary bridges changes from cylinder to unduloid ($\theta \in [0, \pi/2)$) to nodoid ($\theta \in (\pi/2, \pi)$). And it is expected that between unduloid and nodoid there must be a catenoid, because the value of mean curvature cannot change from positive to negative suddenly. Since $|t_0 - \pi/2| < \pi/2$, the capillary bridge in experiment is a fraction of a complete period.

2.3 Crystalline order on catenoid

Here we study crystalline order on the simplest case of a catenoidal capillary bridge ($H = 0$) in the framework of continuum elasticity theory [23, 28, 59]. For simplicity,

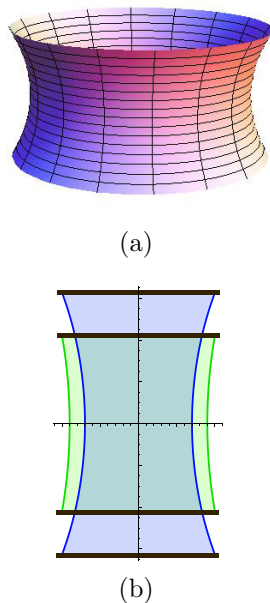


Figure 2.3: (a) The three dimensional shape of a catenoid of aspect ratio $c = 0.85$. (b) A catenoid of aspect ratio $c = 0.9$ (green) deforms to $c = 0.7$ (blue).

we measure all lengths in units of the radius of the contact disk. We treat the topological defects, including dislocations and disclinations, as degrees of freedom rather than all the interacting particles. It greatly reduces the number of degrees of freedom. Starting from the elastic free energy, we derive and discuss the interactions of topological defects on catenoid capillary bridge.

2.3.1 The geometric approach

The topology of the capillary surfaces we study is that of the annulus, with Euler characteristic zero, since the liquid bridge makes contact with the plates at the top and bottom. Such a surface admits regular triangulations with all particles having coordination number 6. Although defects (non 6-fold coordinated particles) are not topologically required they may be preferred in the crystalline ground state for purely energetic reasons since negative Gaussian curvature will favor the appearance of 7-coordinated particles (-1 disclinations). To determine the preferred defect configuration we map the microscopic interacting particle problem to the problem of discrete

interacting defects in a continuum elastic background. The defect free energy F_{el} , in the limit of vanishing core energies, is expressed in the form [31, 59, 133]:

$$F_{el} = \frac{1}{2}Y \int_{x,y} G_{2L}(x,y)\rho(x)\rho(y), \quad (2.37)$$

where Y is the Young's modulus for the 2-dimensional crystal. x and y are position vectors on 2-dimensional surface. The effective topological charge density is

$$\begin{aligned} \rho(x) &= \frac{\pi}{3} \sum_{\alpha} q_{\alpha} \delta(x, x_{\alpha}) - \sum_{\beta} \gamma^{ij} b_i^{\beta} \nabla_j \delta(x - x_{\beta}) - K(x) \\ &= \frac{\pi}{3} q(x) - \gamma^{ij} \nabla_j b_i(x) - K(x). \end{aligned} \quad (2.38)$$

x_{α} and x_{β} are the positions of disclination q_{α} and dislocation \vec{b}^{β} on the 2-dimensional surface. $\delta(x, x_i) = g^{-1/2} \prod_i \delta(x - x_i)$. $K(x)$ is the Gaussian curvature. $G_{2L}(x, y)$ is the Green's function for the covariant biharmonic operator on curved surface.

$$\Delta \Delta G_{2L}(x, y) = \delta(x, y). \quad (2.39)$$

g is the determinant of metric of surface. $\gamma^{ij} = \frac{1}{\sqrt{g}} \epsilon^{ij}$, ϵ^{ij} is the antisymmetric tensor in Cartesian coordinates. The first and second terms in Eq.(2.39) are the charge densities of disclination and dislocation, respectively. So the Gaussian curvature cannot only be screened by disclination (or scar) but also by dislocations (or pleats).

By introducing χ

$$\Delta \Delta \chi(x) = Y \rho(x) \quad (2.40)$$

and using Eq.(2.39), Eq.(2.37) can be written in a more compact form

$$\begin{aligned} F_{el} &= \frac{1}{2} \int_{x,y} \frac{1}{\Delta^2} \delta(x, y) \Delta^2 \chi(x) \rho(y) = \frac{1}{2} \int_x \chi(x) \rho(x) \\ &= \frac{1}{2Y} \int_x \chi(x) \Delta(\Delta \chi(x)) = \frac{1}{2Y} \int_x (\Delta \chi(x))^2, \end{aligned} \quad (2.41)$$

where in the last step the Green's second identity is used: $\int_V (\psi \Delta \phi - \phi \Delta \psi) = \int_{\partial V} (\psi \partial_n \phi - \phi \partial_n \psi)$. $\partial_n = \vec{n} \cdot \nabla$. And the boundary conditions for χ are imposed:

$$\chi|_{\partial} = 0 \quad (2.42)$$

and

$$\vec{n} \cdot \nabla \chi|_{\partial} = 0. \quad (2.43)$$

By introducing

$$\Gamma(x) = \Delta \chi(x), \quad (2.44)$$

we have

$$\Delta \Gamma(x) = Y \rho(x). \quad (2.45)$$

So

$$\frac{\Gamma(x)}{Y} = \int_y G_L(x, y) \rho(y) + U(x) = \int_y G_L(x, y) \left(\frac{\pi}{3} q(y) - \gamma^{ij} \nabla_j b_i(y) \right) - \Gamma_s(x) + U(x) \quad (2.46)$$

in which $\Delta U(x) = 0$.

$$\Gamma_s(x) = \int_y G_L(x, y) K(y), \quad (2.47)$$

which is the reflection of the screening effect of Gaussian curvature. G_L satisfies

$$\Delta G_L(x, y) = \delta(x, y), x \in M \quad (2.48)$$

with the boundary condition

$$G_L(x, y) = 0, x \in \partial_M. \quad (2.49)$$

In order to solve the Green's function, we do coordinates transformation from $\{x, y \equiv (u, v)\}$ to $z = \rho(u, v)e^{iu}$, in which u, v are the parametrization of surface of revolution [31]. $u = \text{const}$ defines the meridians of surface and $v = \text{const}$ defines the latitude lines. $u \in [0, 2\pi), v \in [-v_m, v_m]$ for surface of revolution with reflection symmetry. The mapping from $\{u, v\}$ to the complex plane is conformal as the angle is preserved in the mapping and z is an analytical function of u, v . Working in complex plane, the Green's function can be found as [31]

$$G_L(\vec{x}, \vec{y}) = \frac{1}{2\pi} \ln \left| \frac{\rho_0^{-1} z(\vec{x}) - z(\vec{y})}{1 - \rho_0^{-1} z(\vec{x}) \bar{z}(\vec{y})} \right|. \quad (2.50)$$

where ρ_0 is the radius of the outer circle of the annulus in the complex plane. For a catenoid, the conformal mapping is given by $\rho(u, v) = c \exp(|v|/c)$ and $\rho_0 = c \exp(\text{arcsech}(c))$ (see Appendix A).

2.3.2 Effective disclination charge

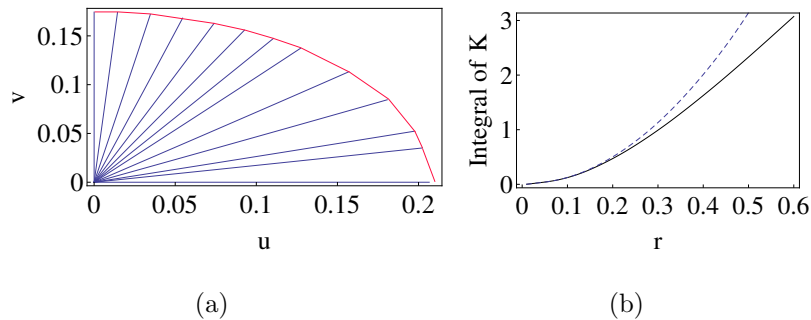


Figure 2.4: (a) A family of geodesics in $\{u, v\}$ coordinates centered at a point on the waist of a catenoid of $c = 0.85$. (b) The $|K(0)|\pi r^2$ (dashed curve) and numerical result (solid curve) of the integrated Gaussian curvature over a geodesic disk of radius r versus r . $c = 1/2$.

Disclinations are expected to appear in the crystalline ground state when the Gaussian curvature is sufficient to support them. Consider therefore a putative isolated disclination of strength $q = -1$ (coordination number 7) at the waist of a catenoid. The curvature condition above requires that there exist a disk of geodesic radius r_c , centered on the 7-disclination, for which [35, 59]

$$\int_{disk} K dA = -\frac{\pi}{3}. \quad (2.51)$$

Clearly r_c must be less than the geodesic distance l from the waist to the boundary [35]. For a given size catenoid c , we calculate l and the integral of the Gaussian curvature over the geodesic disk of radius l . The value of c for which the integrated curvature equals $-\pi/3$ is the critical value of c for the appearance of 7-disclinations. We compute the integral of the Gaussian curvature numerically. We first construct a family of geodesics radiating from the core 7-disclination (at $u = 0, v = 0$) by solving the geodesic equation:

$$\frac{d^2 x^\mu}{d\lambda^2} + \Gamma_{\rho\delta}^\mu \frac{dx^\rho}{d\lambda} \frac{dx^\delta}{d\lambda} = 0, \quad (2.52)$$

in which $x^1 = u, x^2 = v$ and $\Gamma_{\rho\delta}^\mu$ is the Christoffel symbol of the second kind. This second order differential equation has a unique solution given an initial position and an

initial velocity. The initial conditions are $x^1(0) = x^2(0) = 0$, $(dx^1/d\lambda)|_0 = (1/c) \cos \theta$, and $(dx^2/d\lambda)|_0 = \sin \theta$, where θ is the angle of the initial velocity with respect to \vec{e}^u . Given a geodesic radius r , the coordinates of the end point of the geodesic curve can be found. These end points form the boundary of a disk in $\{u, v\}$ coordinates (see Fig.2.4(a)). We then integrate the Gaussian curvature over the prescribed disk numerically. The critical value of c is found to be $c^* = 0.85$ and the corresponding critical radius is $r_c = 0.53$. Note that integrated Gaussian curvature for this critical catenoid is quite large [35]: $\int K dA = -6.6$. The critical value c^* can also be estimated as follows. By introducing Gaussian normal coordinates (r, θ) centered on a 7-disclination at height z_0 above or below the waist of the catenoid, the effective (screened) disclination charge at distance r is given by [7, 28]

$$\begin{aligned} \rho_{eff}(r) &= -\frac{\pi}{3} - \int_0^{2\pi} d\theta \int_0^r dr' \sqrt{g} K(r') \\ &= -\frac{\pi}{3} + \pi \frac{r^2}{c^2} \operatorname{sech}^4\left(\frac{z_0}{c}\right) + \mathcal{O}(r^3). \end{aligned} \quad (2.53)$$

The critical radius is reached when the effective disclination density vanishes: $\rho_{eff}(r_c) = 0$. For a 7-disclination on the waist ($z_0 = 0$) this gives $r_c/c \equiv \theta_c = \sqrt{1/3} \approx 33^\circ$. Now on the catenoid the geodesic length from the waist to the boundary is $\int_0^{z_m} dz \sqrt{1 + (\frac{d\rho}{dz})^2} = \int_0^{z_m} \cosh(v/c) dv = \sqrt{1 - c^2}$. The critical catenoid size c^* is then given by $r_{c^*} = \sqrt{1 - c^{*2}}$. This yields $c^* = \sqrt{3}/2 \approx 0.87$. This estimate for c^* is very close to the numerical value 0.85. Why are these two values so close? In calculating the effective disclination charge, we use $K(0)\pi r^2$ to approximate the integral of the Gaussian curvature over a geodesic disk of radius r . The Gaussian curvature is overestimated as its magnitude is maximum at $r = 0$ (on the waist). On the other hand, since $K(0) = \lim_{r \rightarrow 0} 12(\pi r^2 - A(r))/(\pi r^4) < 0$, the real area $A(r)$ of the disk with geodesic radius r is bigger than πr^2 , i.e., the disk area is underestimated in our approximation. These two approximations tend to cancel each other out. For a typical value of $c = 1/2$, $|K(0)|\pi r^2$ and the numerical result of the integral of the Gaussian curvature versus r is plotted in Fig.2.4(b). As expected the flat space approximation

$K(0)\pi r^2$ is good for small r ($r < 0.2$).

2.3.3 Energetics of topological defects

The information of interactions among topological defects and geometric potential, i.e., the interaction of Gaussian curvature and defects is encoded in Eq.(2.42). Unlike a disclination, a dislocation has orientation. The Burgers vector \vec{b}^α describing a dislocation at position x^α is perpendicular to the 5-7 pair. Eq.(2.42) indicates that the $\vec{b}^\alpha \parallel \vec{e}^1$ orientation of dislocation is preferred in comparison to the orientation $\vec{b}^\alpha \parallel \vec{e}^2$. Throughout this section, we focus on the dislocation with the Burgers vector $\vec{b}^\alpha \parallel \vec{e}^1$.

The elastic free energy associated with the interaction of dislocations can be derived from Eq.(2.42,2.46):

$$F_{dd} = \frac{Y}{2} \int_{x,y,y'} \rho_b(y) G_L(x,y) G_L(x,y') \rho_b(y'). \quad (2.54)$$

By inserting the expression for dislocation density

$$\rho_b = - \sum_{\beta} \gamma^{ij} b_i^\beta \nabla_j \delta(x - x_\beta) \quad (2.55)$$

from Eq.(2.39) and considering that all Burgers vectors are parallel to \vec{e}_1 , we have

$$F_{dd} = \frac{Y}{2} \sum_{\alpha,\beta} b_1^\beta b_1^\alpha \int_{y_1,y_2,y'_1,y'_2,x} \frac{\partial \delta(y - y^\beta)}{\partial y_2} G_L(x,y) G_L(x,y') \frac{\partial \delta(y' - y'^\beta)}{\partial y'_2}. \quad (2.56)$$

A dislocation can "feel" a potential due to the Gaussian curvature, which is called geometric potential. From Eq.(2.37), one may extract the interaction between a dislocation and the Gaussian curvature:

$$F_{dG} = Y \sum_{\beta} b_1^\beta V_{dG}(y^\beta), \quad (2.57)$$

where

$$V_{dG}(y^\beta) = \int_{x,y'} \frac{1}{\sqrt{g}(y_2^\beta)} K(y') G_L(x,y') \frac{\partial G_L(x,y)}{\partial y_2} \Big|_{y_2^\beta}. \quad (2.58)$$

The geometric potential V_{dG} only depends on the position of dislocation. The "self-energy" of dislocations, which is proportional to Yb^2 , is neglected, since it is much smaller than $F_{dG} \sim Yb$. Note that the magnitude of Burgers vector $b \sim a$, the lattice spacing, which is dimensionless as we define the radius of the end cross section of capillary bridge as unit length. By comparing the dislocation-dislocation interaction and geometric potential, we have

$$\frac{F_{dG}}{F_{dd}} \sim \frac{YbV_{dG}}{Yb^2V_{dd}} \sim \frac{Yb^2(V_{dG}/b)}{Yb^2V_{dd}} \sim \frac{(V_{dG})}{V_{dd}} \frac{1}{b} \gg 1, \quad (2.59)$$

where the last step due to the comparability of V_{dd} and V_{dG} . Yb^2 is of the dimension of energy. Therefore, the magnitude of geometric potential is much bigger than the dislocation-dislocation interaction. Similarly the disclination-dislocation, and geometric potential of disclination can also be derived from Eq.(2.42). The geometric potential of disclination at y^D on capillary bridge is

$$F_{DG}(y^D) = \frac{\pi Y}{3} V_{DG}. \quad (2.60)$$

$$V_{DG} = \frac{\pi}{6} \int_x G_L(x, y_D) G_L(x, y_D) + \int_{x, y'} G_L(x, y_D) G_L(x, y') K(y'). \quad (2.61)$$

The disclination-dislocation interaction can be derived from Eq.(2.42,2.46):

$$F_{Dd} = -\frac{\pi Y}{3} b_1 \int_x \frac{1}{\sqrt{g}(y^d)} \frac{\partial G_L(x, y_1^d, y_2^d)}{\partial y_2^d} \Big|_{y_2^d=y_2^d} G_L(x, y^D) \equiv -\frac{\pi Y}{3} b_1 V_{Dd}. \quad (2.62)$$

We study the behavior of topological defects on catenoid capillary bridge by applying the above formalisms about energetics of topological defects Eq.(2.56,2.57,2.60,2.62).

First of all, we show that the critical waist size c^* can also be estimated from energetic arguments. From the free energy of Eq.(2.42) one can analyze the geometric potential describing the interaction between disclinations and the intrinsic Gaussian curvature of the surface. The result is shown in Fig.2.5). We see that the optimal position of a disclination shifts from the boundary to the waist as c decreases. The transition point for the emergence of a disclination in the interior of a catenoidal

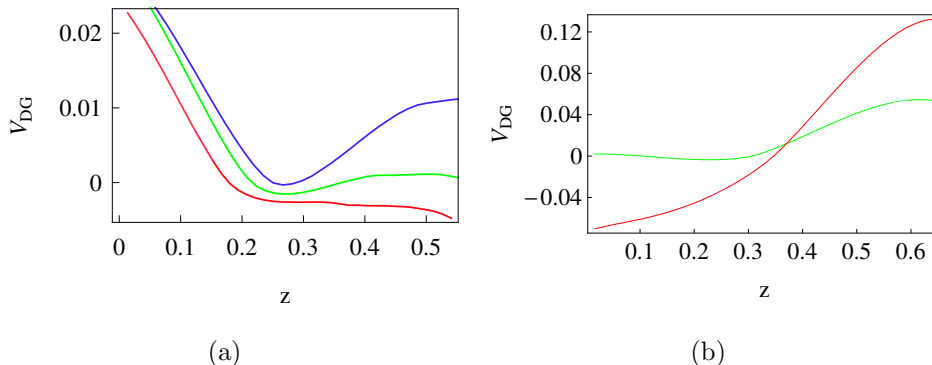


Figure 2.5: (a) The geometric potential of an isolated disclination for three different values of c : $c = 0.8$ (red), $c = 0.75$ (green) and $c = 0.7$ (blue). The optimal position of an isolated disclination moves from the boundary to the waist of the catenoid in the rather narrow window c between 0.8 and 0.75. (b) The geometric potential of an isolated disclination for catenoids with $c = 0.5$ (red) and $c = 0.6$ (green).

capillary bridge is $c^* \approx 0.8$, again consistent with the value obtained above based on geometrical arguments.

Net disclination charges may appear either in the form of point-like isolated disclinations or extended linear grain boundary scars. Scars result from the screening of an isolated disclination by chains of dislocations and typically arise when the number of particles exceeds a threshold value beyond which the energy gained exceeds the cost of creating excess defects [59]. Here we semi-quantitatively construct the phase diagram for isolated disclinations versus scars on a catenoidal capillary bridge characterized by the number of particles and the aspect ratio of the catenoid c .

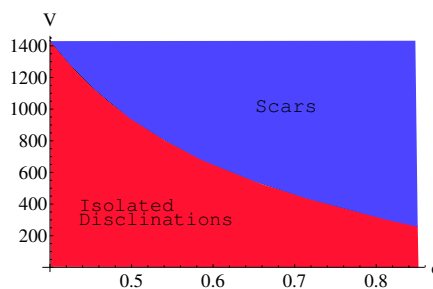


Figure 2.6: The phase diagram in the particle number-aspect ratio plane for isolated disclinations versus scars for $c < c^*$.

Consider a disclination on a capillary bridge (for $c < 0.85$) radiating m grain boundaries (scars). The spacing of neighboring dislocations is $l = a m/s_{eff}$ [28], where a is the lattice spacing. As $s_{eff} \rightarrow 0$, the dislocation spacing within a scar diverges and the grain boundary terminates. If the disclination can be completely screened by Gaussian curvature within a circle of radius $r \approx 3a$, then grain boundaries will not form around the core disclination. The condition for isolated disclinations is therefore $|K_{max}\pi(3a)^2| \sim \pi/3$, where $|K_{max}| = 1/c^2$ is the Gaussian curvature at the waist of the bridge. On the other hand, the number of particles N is related to the surface area A between $z \in [-z_m, z_m]$ via $A(c) = (\sqrt{3}/2)a^2N$. The curve separating isolated disclinations from scars is thus given by $N = 18\sqrt{3} A(c)/c^2$, as plotted in Fig.2.6(a). The phase boundary reveals two basic types of transition in the topological structure of the ground state as the particle number and the geometry (aspect ratio) of the capillary bridge are varies. For a fixed catenoid aspect ratio below the critical value for the appearance of excess 7s in the interior there is a transition from isolated 7s to linear grain boundary scars with one excess 7 as the number of particles increases. For a fixed number of particles above a threshold value ($N_c \approx 300$) there is a transition from isolated disclinations to scars as the capillary bridge gets fatter and the decreasing Gaussian curvature is insufficient to support isolated 7-disclinations.

Disclinations and anti-disclinations attract and may form dipole bound states (7-5 pairs). Such dipole configurations are themselves another type of point-like topological defect in two-dimensional crystals - dislocations. Dislocations on a triangular lattice correspond to two semi-infinite Bragg rows 60° apart both terminating at a common point - the location of the dislocation. Since they are tightly bound states of disclinations the energetics of dislocations may be derived from the governing energetics of disclinations on a curved geometry - Eq.(2.42). Dislocations, unlike disclinations, are oriented. The Burgers vector \vec{b}^α characterizing a dislocation at position x^α is perpendicular to the 5-7 bond. An analysis of Eq.(2.42) shows that the preferred

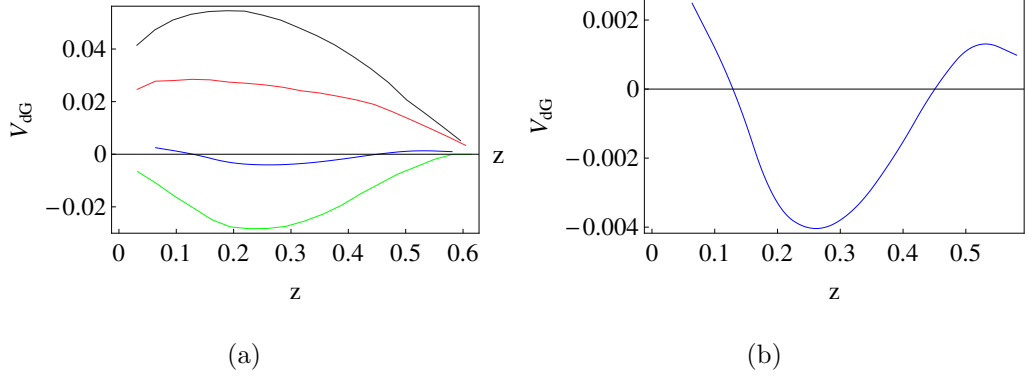


Figure 2.7: (a) The geometric potential of isolated dislocations as a function of height for four different values of c : $c = 0.7$ (black), $c = 0.68$ (red), $c = 0.66$ (blue) and $c = 0.65$ (green). The optimal position moves from near the boundary towards the waist as c decreases. (b) is an enlarged view of the blue curve to show the transition from the red to the green curve.

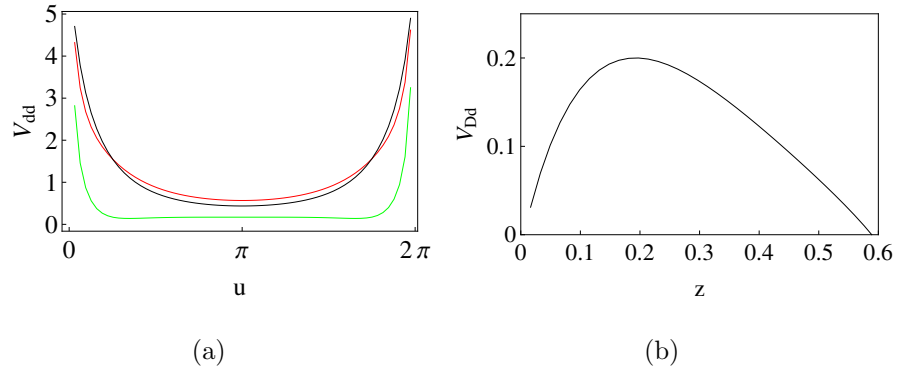


Figure 2.8: The interactions of defects. (a) The dislocation-dislocation interaction V_{dd} of two dislocations along \vec{e}^u at the same height. $z = 0.5 z_m$ (black), $z = 0.3 z_m$ (red) and $z = 0.1 z_m$ (green). (b) The disclination-dislocation interaction V_{Dd} as a function of their longitudinal separation. The disclination is fixed on the waist ($c = 1/2$).

orientation of the Burgers vector is along \bar{e}^u . This is clear from the fact that the 7-disclination has minimum energy when located at the waist with the accompanying 5-disclination in the direction of the boundary where the negative Gaussian curvature drops most rapidly. Thus the 7-5 bond should be along a meridian and the Burgers vector along a line of latitude. From here on we restrict ourselves to this case.

The variable Gaussian curvature of a catenoidal capillary bridge also leads to optimal positions for isolated dislocations. Fig.2.7 shows the geometric potential for isolated dislocations as a function of height above the waist. As the waist radius c decreases the optimal position of an isolated dislocation moves from the boundary to the interior of the capillary bridge since the increasing maximal negative Gaussian curvature increasingly attracts 7-disclinations with their tightly bound 5-disclinations. The boundary-to-interior transition occurs for $c^{**} \approx 0.68$. The corresponding integrated Gaussian curvature $\int K dA \approx -9.0$ [35]. This detachment transition is also observed in experiments with capillary bridges [35] - in the experimental case the capillary bridges are generally nodoids with non-vanishing mean curvature and the analysis is correspondingly more elaborate. The optimal position of a single dislocation for small c , say $c = 0.3$, is $z(c = 0.3) = 0.25z_m$. Thus the optimal position of a single dislocation is far from the waist, even for a strongly curved catenoidal capillary bridge, in contrast to the case of disclinations. This result can be understood in terms of the Peach-Koehler forces acting on the individual positive and negative disclinations that make up a dislocation [35, 149]. While the 7-disclination prefers to be at the waist the 5 prefers to be at the boundary - the competition results in an optimal dislocation position somewhere in between the two extremes. Here we treat only single dislocations but it is possible for chains of dislocations to appear in the form of pleats, as elegantly discussed in Ref.[35].

Finally we turn to the interaction between defects themselves. Fig.2.8 (a) shows the dislocation-dislocation interaction along \bar{e}^u . Two dislocations at the same height feel a short-range repulsion. Note that near the waist shallow local minima appear.

This differs from the interaction in flat space where parallel dislocations always repel to each other with a logarithmic potential [150]. The attractive interaction between a disclination and a nearby dislocation is shown in Fig.2.8(b) with the disclination fixed on the waist.

The influence of spatial curvature and topology on two-dimensional phases of matter continues to yield surprises. The presence of 7-disclinations in negative curvature crystals may offer unique opportunities for functionalization of micron-scale crystallized "superatoms" via chemistry that recognizes the unique crowded environment of a 7-disclination [59, 151].

Appendix 2.A Conformal mapping of catenoid onto complex plane

Any 2-dimensional smooth Riemannian manifold can be equipped with a set of local isothermal (or conformal) coordinates (x, y) s.t., the metric is expressed as

$$ds^2 = w(x, y)(dx^2 + dy^2). \quad (2.63)$$

One the complex plane with $z = \rho e^{i\phi}$, the new metric will be

$$ds^2 = w(z)(d\rho^2 + \rho^2 d\phi^2). \quad (2.64)$$

The conformal factor $w(z)$ can be found by equating the above metric to the original one. For catenoid,

$$ds^2 = \cosh^2\left(\frac{v}{c}\right)(dv^2 + c^2 du^2). \quad (2.65)$$

By equating Eq.(2.64) and (2.65), we have

$$w(z) = \left(\frac{c \cosh(v/c)}{\rho}\right)^2, \quad (2.66)$$

$$\phi = u \quad (2.67)$$

and

$$\frac{d\rho}{dv} = \pm \frac{\rho}{c}. \quad (2.68)$$

The solution to the last equation is

$$\rho = e^{\pm v/c}. \quad (2.69)$$

By mapping the surface of catenoid onto a 2-dim torus with inner radius c (equal to the radius of waist of catenoid) and imposing the reflection symmetry of catenoid about its waist, we have

$$\rho = c e^{|v|/c}. \quad (2.70)$$

Chapter 3

Morphology of nematic and smectic vesicles

3.1 Introduction

Recent experiments on vesicles formed from block copolymers with liquid-crystalline side-chains reveal a rich variety of vesicle morphologies. The additional internal order (“structure”) developed by these self-assembled block copolymer vesicles can lead to significantly deformed vesicles as a result of the delicate interplay between two-dimensional ordering and vesicle shape. The inevitable topological defects in structured vesicles of spherical topology also play an essential role in controlling the final vesicle morphology. Here we develop a minimal theoretical model for the morphology of the membrane structure with internal nematic/smectic order [54]. Using both analytic and numerical approaches, we show that the possible low free energy morphologies include nano-size cylindrical micelles (nano-fibers), faceted tetrahedral vesicles, and ellipsoidal vesicles, as well as cylindrical vesicles. The tetrahedral vesicle is a particularly fascinating example of a faceted liquid-crystalline membrane. Faceted liquid vesicles may lead to the design of supra-molecular structures with tetrahedral symmetry and new classes of nano-carriers.

Amphiphilic block copolymers in water, like natural phospholipids, can self-assemble into various monolayer or bilayer structures, such as micelles and vesicles [152, 153]. In particular, rod-coil block copolymers, with a flexible hydrophilic chain and one or more rod-like hydrophobic blocks, exhibit a rich morphology of structures, and therefore have significant potential to advance fundamental science and drive technological innovations [154, 155, 156, 157, 158, 159, 160, 161, 162, 163]. Among these rod-coil block copolymers, we are especially interested in liquid crystalline (LC) block copolymers in which the hydrophobic block is a nematic or smectic liquid crystal polymer [49, 50, 51, 164, 165, 166, 167, 168]. The in-plane LC order that results from molecular pair interactions in these systems, and the associated defect structure, play very important roles in determining the preferred intermediate and final shapes of vesicles. The tailor-design of both material properties and vesicle morphology by controlling the molecular structures of the block polymers is state-of-the-art research in the fields of polymer science, materials science and chemical engineering.

Some of the structures formed by these LC side-chain block copolymers in aqueous solution are rather counterintuitive, such as faceted vesicles, nanotubes and compact vesicles with tiny inner space [51, 165]. In all these structures, the in-plane smectic order is clearly visible under Cryo-TEM. In this article we develop a theoretical explanation of the geometric structures of vesicles with in-plane nematic or smectic order. We present a simple model free energy as a functional of both the membrane geometry and the in-plane nematic order. Using both analytic and numerical methods, we then analyze the low free energy morphologies in various parameter regimes.

3.2 Model

3.2.1 Free energy

Focusing on their overall shape we first perform a mean-field analysis of the model free energy of a self-assembled monolayer as a functional of their shape and nematic

order parameters [39, 52]:

$$H_m = \frac{1}{2} \int \sqrt{g} d^2x \left[K (\vec{D}\hat{n})^2 + \kappa (H - H_0)^2 \right] \quad (3.1)$$

Here K is the Frank constant in the one-constant approximation, while \vec{D} denotes the covariant derivative. H is the mean curvature and H_0 is the spontaneous curvature, which is determined by the asymmetry in the sizes of the hydrophobic and the hydrophilic parts of the LC block copolymers. We shall choose the normal vector of the monolayer to point from the hydrophobic side to the hydrophilic side. Therefore $H > 0$ means that the hydrophilic side is bending outwards.

All three parameters K, κ, H_0 depend on the chemical structures of the block copolymers as well as their interaction with the solvent in a complicated way. Furthermore, strictly speaking, a nematic membrane is locally anisotropic. Therefore its Frank free energy is characterized by two constants: one for splay (K_1) and one for bend (K_3). Likewise, the bending energy as well as the spontaneous curvature should also be generically anisotropic, characterized by three bending constants and three spontaneous curvature components. Such a model is characterized by 8 independent parameters and is extremely complicated to analyze. For the sake of simplicity, we shall focus on the greatly simplified toy model Eq. (3.1), which captures the essential physics of nematic vesicles which is the competition between the extrinsic bending energy and the two-dimensional Frank free energy.

A more important, conceptual issue is the following: In what sense can the vesicle morphology be understood in terms of minimization of elastic free energy Eq. (3.1)? As is well known, the formation of vesicles is a complicated nonequilibrium process. Whether a certain property of a vesicle is distributed according to Gibbs-Boltzmann depends on the relevant experimental time scale, and on the time scale at which the given property equilibrates. At the stage of vesicle formation, individual molecules on the membrane can diffuse quite efficiently. Motion of liquid crystalline defects, however, requires coherent movement of all polymers on the vesicle, and is usually very slow. Hence we expect that the vesicle morphology achieves a local thermal equi-

librium, where the shape and LC order minimizes the elastic free energy Eq. (3.1) (with appropriate parameters corresponding to the physical conditions under which the self-assembly takes place), subject to global constraints of given vesicle topology and LC defects distribution. We shall then enumerate all possible vesicle topologies and compare these free energy minima. It is interesting to note that in recent experiments by Jia *et. al.* [164], multiple vesicle topologies were often observed using a given preparation method, suggesting that kinetics of self-assembly also played an important role in the selection of vesicle morphology.

Smectic vesicles can also be viewed as nematic vesicles with bending constant much larger than splay constant. On a membrane with in-plane smectic order, therefore, the bending deformation of the nematic director field should vanish everywhere. Mathematically this is equivalent to $\hat{n} \cdot D\hat{n} = 0$, that is, the nematic director locally follows the geodesics. This is always possible, for an arbitrary but prescribed membrane shape, except at the core of nematic disclinations. For these configurations, the Frank free energy becomes independent of the bending constant. Hence Eq. (3.1) is also a toy model for membranes with in-plane smectic order, with the understanding that K is the splay constant and the nematic director strictly follows the local geodesics.

Minimization of the Frank free energy in Eq. (3.1) requires that the covariant derivatives of the nematic director field vanish everywhere on the surface. As is well known in differential geometry, this is possible only if the Gaussian curvature vanishes everywhere, i.e. the surface is a *developable surface*. The family of developable surfaces includes planes, cylinders, cones, and tangent developable surfaces*. On the other hand, minimization of the bending energy in Eq. (3.1) leads to a constant mean curvature H_0 . It is clear that the only geometry minimizing both terms in the free

* Surfaces spanned by tangent lines of a spatial curve: a generic tangent developable surface that is topologically identical to plane is however not expected to be observed in experiments, because it can easily relax to a plane which has bending energy. It is not clear to us whether there exists a tangent developable surface that is topologically different from all the aforementioned structures.

energy in Eq. (3.1) is a cylindrical monolayer with a given radius $1/H_0$. In the recent example of Jia *et. al.* [164], for example, where only aqueous solvent is present at the final stage of assembly, monolayer cylinders with very small radius (nanofibers) are observed. The inner space of the cylinders is completely filled by the hydrophobic parts of the polymers. In order to form monolayer cylinders with larger radius, the inner space has to be filled by solvent (or other polymers) that are friendly to LC blocks. If there is only aqueous solvent, and if $1/H_0$ is not small, monolayer cylindrical structures with favorable spontaneous curvatures cannot pack space and therefore the system should form certain kinds of bilayer structures, where two monolayers with opposite orientation stack together.

The free energy of a symmetric bilayer membrane can be obtained by adding up the free energies for two monolayers on both sides of the bilayer:

$$H_m = \int \sqrt{g} d^2x \left[K (\vec{D}\hat{n})^2 + \kappa H^2 \right] \quad (3.2)$$

We shall focus on the morphology of symmetric bilayers in the remainder of this article. Note that area differences between the inner and outer layer can lead to non-vanishing spontaneous curvature [169, 170]. These effects will not qualitatively change our conclusions.

3.2.2 Lattice model

To implement a deformable lattice model with spherical topology, we first introduce a reference sphere and tessellate it with a triangular mesh along with 12 requisite 5-disclinations. Afterward a dual lattice of the triangular mesh is constructed, each dual site being the center of mass of each plaquette formed by the original triangular lattice. The details of the lattice geometry are illustrated in the supplementary information. Let \hat{m}_α to be the unit vector normal to the plaquette α . A director \hat{n}_α and a projection operator $\hat{N}_\alpha = \hat{n}_\alpha \hat{n}_\alpha$ are defined on each dual site with a constraint that it must be perpendicular to the plaquette normal: $\hat{N}_\alpha \cdot \hat{m}_\alpha = 0$.

Let $d_{\alpha\beta}$ be the bond length connecting two neighboring dual sites α and β , and $S_{\alpha\beta}$ be the area spanned by the bond $\alpha\beta$. The discretized Frank free energy is then given by

$$F_{\text{Frank}} = K \sum_{\langle\alpha\beta\rangle} S_{\alpha\beta} d_{\alpha\beta}^{-2} \text{Tr} [(\hat{N}_\beta - \hat{N}_\alpha)^2] \quad (3.3)$$

The bond lengths $d_{\alpha\beta}$ and the areas $S_{\alpha\beta}$ are introduced to ensure that the lattice model is a proper discretization of the continuum model Eq.(3.2). They insure that, up to errors which scale with the plaquette area $S_{\alpha\beta}$, the lattice free energy is invariant under change of triangulation. The discrete reparametrization invariance is necessary so that the free energy depends only on vesicle shape and not on the specific structure of the mesh. This is implemented for each shape as the vertices are deformed.

The discretized bending energy is given by

$$F_{\text{bending}} = \kappa \sum_{\alpha} S_{\alpha} \text{Tr} \mathbf{K}_{\alpha}^2, \quad (3.4)$$

where \mathbf{K}_{α} is the extrinsic curvature tensor at site α , whilst S_{α} is the area of the plaquette α . The curvature tensor \mathbf{K}_{α} of each plaquette α can be calculated from the following three equations:

$$\begin{aligned} e_{\alpha\beta}^{\parallel} &= \frac{1}{2} \vec{e}_{\alpha\beta}^{\perp} \cdot \mathbf{K}_{\alpha} \cdot \vec{e}_{\alpha\beta}^{\perp} \\ e_{\alpha\gamma}^{\parallel} &= \frac{1}{2} \vec{e}_{\alpha\gamma}^{\perp} \cdot \mathbf{K}_{\alpha} \cdot \vec{e}_{\alpha\gamma}^{\perp} \\ e_{\alpha\delta}^{\parallel} &= \frac{1}{2} \vec{e}_{\alpha\delta}^{\perp} \cdot \mathbf{K}_{\alpha} \cdot \vec{e}_{\alpha\delta}^{\perp}, \end{aligned} \quad (3.5)$$

where $\vec{e}_{\alpha\beta}$ is the vector pointing from vertex α to vertex β , and $e_{\alpha\beta}^{\parallel}$ and $e_{\alpha\beta}^{\perp}$ are its components parallel and perpendicular to the plaquette normal \hat{m}_{α} .

In the MC simulations, the deformable surface consists of 300 vertices, corresponding to 596 directors in all. The initial shape of the surface is a unit sphere and the initial director orientations are random. Each MC sweep consists of trial attempts to rotate each director and to move each vertex. The acceptance or rejection of a MC trial is determined by the standard Metropolis algorithm. All vertices are allowed to

move along the radial direction with the angular positions of the vertices fixed. In order to preserve the total area upon surface deformation, any vertex moves making a total area change larger than 1% are rejected. Finally, once the surface is deformed by vertex moves, the orientations of directors are corrected by projecting them onto the newly deformed plaquette before the new free energy is calculated.

Finally we remark that we have checked carefully that the location of nematic defects is not influenced by the inevitable lattice disclinations associated with spherical topology and present in our meshes as described above.

3.3 Ground state morphologies

3.3.1 Analytical analysis

Without considering the boundary effects, a flat bilayer with uniform nematic order clearly minimizes both terms in Eq. (3.2). The energy cost associated with the boundary, however, increases with the system size, and exceeds that associated with a closed vesicle with nonzero curvature, for sufficiently large systems [171]. Close vesicles therefore must form for sufficiently large bilayer membranes.

The morphology of a bilayer is controlled by the competition between the extrinsic bending energy and the Frank free energy. We shall first limit the discussion to closed vesicles of spherical topology. Since the total Gaussian curvature is nonvanishing, the system is frustrated and the Frank free energy competes with the bending energy. First consider the limiting case $K \ll \kappa$. The dominant contribution to the total energy is then the bending energy: minimizing this leads to a round spherical shape. For a more realistic model where the bending energy is not isotropic, however, the shape will reflect the anisotropy of the bending moduli, leading to ellipsoidal shapes. The exact form of the shape as a function of the bending moduli is rather difficult to calculate, however, and will not be treated in this article. Ellipsoidal vesicles are frequently observed in the experiments of Jia *et. al.* [49], with the smectic layers all

perpendicular to the long axis of the ellipsoid. It can be inferred from this observation that the bending rigidity is higher along the nematic director than perpendicular to the director.

Let us now consider the opposite regime where $K \gg \kappa$. In this case, the system should first minimize the Frank free energy, which leads to developable surfaces with vanishing Gaussian curvature everywhere. This is clearly not possible due to Gauss' *Theorem Egregium*, which states that the total integrated Gaussian curvature of a surface with spherical topology is a topological invariant and equal to 4π . There are faceted polyhedral surfaces, however, for which the Gaussian curvature vanishes everywhere but at a discrete number of (singular) vertices. These vertices are the ideal locations for orientational defects of the LC order (misery loves company) [40]. The total defect strength on a closed surface is also a topological invariant, according to the Gauss-Bonnet theorem. For nematic and smectic orders, this theorem dictates that on a sphere (or any other surface with the same topology), there are three possibilities for the structure of defects: 1) four disclinations each with strength $+1/2$; 2) two defects each with strength $+1$; 3) one strength $+1$ defect and two strength $+1/2$ defects. Now one needs at least four points to span a non-degenerate polyhedron; a tetrahedron in the minimal case. We conclude that in the limiting case $K \gg \kappa$, the ground state morphology of a vesicle with spherical topology is a faceted tetrahedron, with a strength $1/2$ disclination located at each of the four corners. This structure is indeed observed in recent experiments [51, 165], as well as in our simulation, to be discussed in detail below. Note that the faceting observed here has a completely different origin to the well-known buckling of elastic shells where buckling occurs above a critical size $R \sim \sqrt{\kappa/Y}$, with Y the Young's modulus. The free energy Eq.(3.2), on the other hand, is scale free - the ground states are determined solely by the dimensionless ratio K/κ .

It is important to note that not all tetrahedra support a suitable nematic defect configuration. To ensure that the director field has vanishing covariant derivative

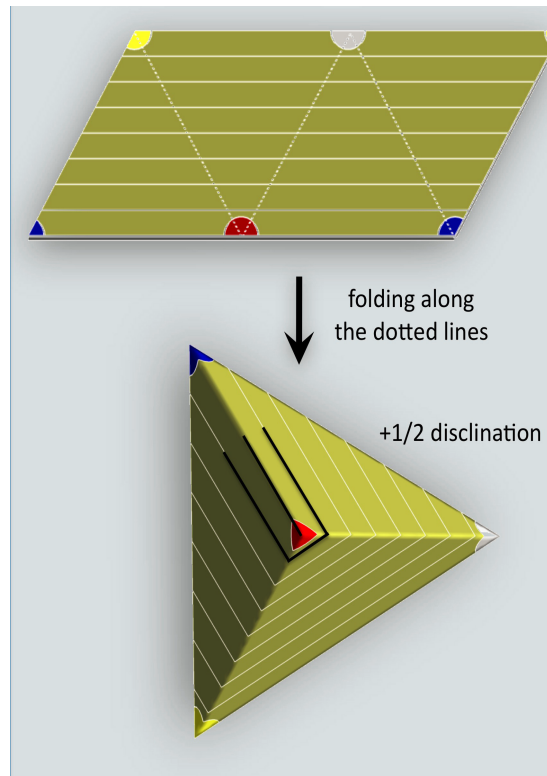


Figure 3.1: Top: A tetrahedron compatible with $+1/2$ disclination on each vertex can be constructed using a parallelogram, by folding along the dashed lines. A constant nematic director field in the unfold parallelogram is shown by the array of parallel straight lines. After folding up, the angles with same color circle around the same vertex. Bottom: The tetrahedron obtained via folding. There is exactly one $+1/2$ disclination on each vertex of the tetrahedron.

everywhere except at the four vertices, but including the six edges, the sum of the three angles surrounding every vertex of the tetrahedron must be 180° . This imposes three constraints on the geometry of the tetrahedron[†]. Since the set of all tetrahedral shapes (up to scaling the overall size) forms a five dimensional space, we see that the set of all fixed-size tetrahedra with vanishing covariant derivative everywhere except the vertices forms a *two dimensional manifold*. Fig.3.1 illustrates how these tetrahedra, together with a nematic director field with vanishing covariant derivative,

[†] Naively we see there are four constraints but the condition for one vertex follows automatically from the constraints for the other three.

can be constructed by folding a parallelogram. These tetrahedra have the special property that all four triangular facets are identical. All these structured smectic vesicles have vanishing Frank free energy. The degeneracy is lifted by different bending energies. The total free energy of the system is given by the sum of the bending energies localized on the six edges and the defect core energies localized at the four vertices. It is rather easy to see that for a given total surface area, the regular tetrahedron has a minimal value for the sum of all edge lengths. Thus *the ground state morphology of a smectic vesicle with spherical topology is a regular tetrahedron when the bending rigidity is vanishingly small*. The transition between different shapes is probably extremely slow, however, as it requires coherent motion of all four nematic disclinations together with the overall smectic layer texture.

The edges and corners cannot be infinitely sharp in a realistic system. They are rounded by either the membrane thickness, the core size of a nematic defect or the small bending rigidity κ . Likewise, the bending energy on the edges must be finite. In a realistic self-assembly process, the bending energy may also be partially relieved by preferential aggregation of large polymers on the outside and smaller polymers on the inside of the membrane near the ridges and corners. Faceted surface structures were studied previously in large viral capsids [172, 173], which are formed by crystalline packing of proteins. There the faceting is energetically favorable because it reduces the in-plane strain energy of the crystalline order formed by the constituent proteins. What we have shown here is that a similar faceting can also be driven by the Frank free energy of LC order, despite their liquid nature.

Another candidate for a low free energy morphology is a long cylinder of double layers (nanotube), for which the Frank free energy also vanishes. The bending energy is approximately given by

$$H_{\text{nanotube}} = \kappa A/a^2, \quad (3.6)$$

where a is the radius of the cylinder. The total bending free energy is therefore linear in the membrane area. The faceted tetrahedron, on the other hand, has the total free

energy

$$H_{\text{tetrahedron}} = 4\kappa L/b, \quad (3.7)$$

where L is the length of ridges and b is the radius of curvature of rounded out ridges. Since the area of a tetrahedron grows quadratically in L , it follows that the total bending energy for a tetrahedron scales as the square root of the membrane area. Large faceted tetrahedral vesicles thus have lower free energy than nanotubes. Both morphologies, however, have been observed experimentally [49, 51, 165]. Selection of vesicle morphology is also affected by kinetics of self-assembly, as we discussed above.

3.3.2 Monte Carlo simulation

In order to quantitatively investigate the ground state morphology of nematic vesicles, we develop a lattice nematic model on a deformable surface with spherical topology and perform energy minimization by the method of simulated annealing Monte Carlo (MC). Details of the discretized form of the free energy, whose continuum limit is given by eq. (3.2), can be found in ref. [174] and the Methods section.

The simulation results for nematic vesicles at various bending rigidities show remarkable morphological transitions, as displayed in Fig.3.2. For convenience we set $K = 1$. This does not change any essential physics since the vesicle morphology depends only on the dimensionless ratio κ/K . As the bending rigidity κ decreases, the vesicles with an isotropic Frank elastic constant undergo substantial shape deformation: 1) the almost spherical morphology is found to be stable at large κ (Fig.3.2a, d); 2) ridges connecting four defects develop as κ becomes smaller than 1 (Fig.3.2b, e); 3) a tetrahedral vesicle forms at a vanishingly small $\kappa = 0.05$ (Fig.3.2c, f). The faceting transition occurs near $\kappa \simeq 1$ [‡]. The stable morphologies are determined by a delicate balance between the in-plane Frank energy and the bending energy as

[‡] We emphasize, however, that these morphological changes are smooth crossovers. There is no real phase transition in the thermodynamic sense.

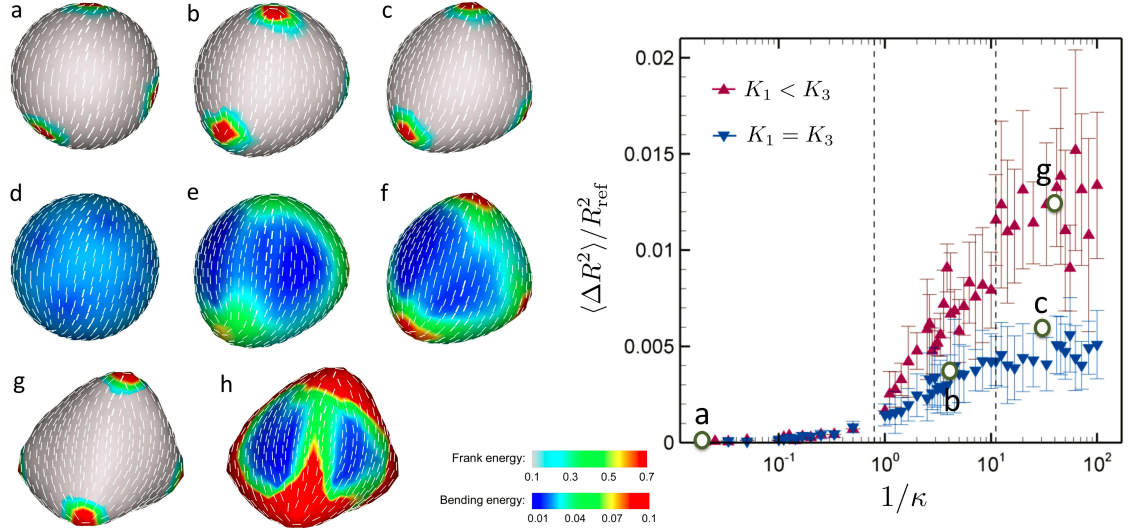


Figure 3.2: Morphology of nematic vesicles at different bending rigidities. Left: The local Frank (a)–(c), (g) and bending (d)–(f), (h) energy contour plots; for a case of $K_1 = K_3 = 1$, (a) and (d), $\kappa = 100.0$; (b) and (e), $\kappa = 0.3$; (c) and (f), $\kappa = 0.05$; for a case of $K_1 \neq K_3$, (g) and (h), $\kappa = 0.04$. The total Frank free energies (in units of $k_B T$) are 62.83, 59.06, 57.1, and 65.27, respectively. The normalized total bending energies (in units of $k_B T$) are 12.55, 16.0, 18.58, and 50.34, respectively. Right: Calculated asphericities of nematic vesicles as a function of the inverse bending rigidity of $1/\kappa$. The inverse triangles are for a case of $K_1 = K_3$ and the triangles are for a case of $K_1 \neq K_3$ ($K_3/K_1 \approx 2.0$). The empty circles represent locations corresponding to the morphologies of (a)(d), (b)(e), (c)(f), and (g)(h).

the surface deforms away from round. Indeed, as κ decreases from 100.0 to 0.05, the Frank free energy falls from 62.83 to 57.1 at the expense of bending energy which increases from 12.55 to 18.58. The Frank energy is localized near the four defects, which consequently induce deformation around the vertices. Our simulations are therefore entirely consistent with our prediction that spherical vesicles are stable in the regime of $K \ll \kappa$, whereas the faceted tetrahedral vesicles become stable in the other extreme $K \gg \kappa$.

We also explore the effect of anisotropy in the Frank elastic constants by studying the regime in which splay dominates over bend. The smectic regime, as noted

earlier, corresponds to the limit $K_3 \gg K_1$. In the current simulation, the anisotropy is estimated to be $K_3/K_1 \simeq 2.0$ (see supplementary information). Although the shape transition trends are qualitatively similar for both the one-Frank constant and anisotropic cases, the anisotropy leads to a more dramatic shape transition, resulting in a considerably more faceted tetrahedral vesicle at a very small $\kappa = 0.04$, as displayed in Figs.3.2g and h. In fact, the splay dominant nematic texture enhances the faceting more than the isotropic case does. This is clearly understood by considering two membranes which possess a +1 disclination defect with pure splay and pure bending nematic textures, respectively. The pure splay always decreases the Frank energy by buckling out-of plane, because it allows the defect to escape into the third dimension and thus better align the nematic directors. On the other hand, such out-of-plane deformation of the pure bending does not alter the Frank energy and therefore, the faceting of pure bending membranes is not favorable upon deformation. Note that we are restricting ourselves here to the case of isotropic bending rigidity.

More prominent shape changes for vesicles with the anisotropic Frank elastic constants are clearly confirmed from a quantitative measurement of the asphericity (i.e., degree of deviation from the reference unit sphere geometry), which is defined as follows:

$$\frac{\langle \Delta R^2 \rangle}{R_{\text{ref}}^2} = \frac{1}{N} \sum_{\alpha} \frac{(R_{\alpha} - R_{\text{ref}})^2}{R_{\text{ref}}^2}, \quad (3.8)$$

where R_{α} is the radial distance of vertex α , R_{ref} is the radius of the reference unit sphere, and N is the total number of vertices. The asphericities are averaged over 10 simulation runs for each κ and plotted in Fig.3.2 as a function of $1/\kappa$. The plot exhibits relatively large deviations from its average values, especially at low bending rigidity. This is mainly attributable to the differences in the asphericity between the three possible ground state morphologies. Although faceted tetrahedral vesicles are expected to be the ground state for large system sizes, we have observed in our simulation three different ground state morphologies, presumably due to its finite system

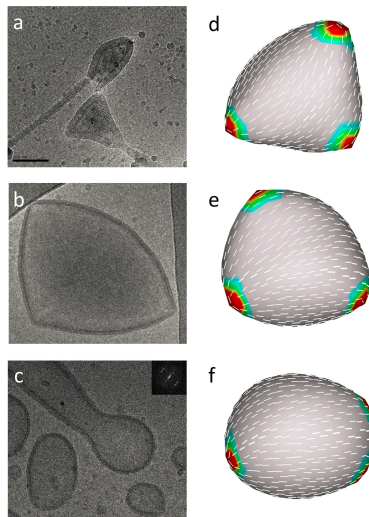


Figure 3.3: Comparison between experimental observations (a)–(c) and computer simulations (d)–(f). Left: Experimental results, (a) a tetrahedron-shape smectic vesicle [51]; (b) a fat tetrahedron-shape smectic vesicle [165]; (c) an ellipsoidal smectic vesicle [49]. Right: Simulation results for a case of $K_3/K_1 \approx 2.0$, (d) $\kappa = 0.04$; (e) $\kappa = 0.1$; (f) $\kappa = 0.5$. The contour plots show the distribution of the local Frank free energy.

size: i) an ellipsoidal vesicle with two closely bounded disclination pairs; ii) a flattened (square cushion-shape) vesicle with four $+1/2$ disclinations located approximately in one plane; and iii) a tetrahedral vesicle with four well separated $+1/2$ defects (see supplementary information). These three morphologies seem degenerate as the differences in their total free energies are within 0.5%. These vesicle shapes can be viewed as the precursors of the extreme morphologies at $\kappa \rightarrow 0$, such as long fibrous cylinders, double layer sheets, and sharply faceted tetrahedrons, respectively. Finally, we briefly compare our simulation results with our recent experimental observations in Fig.3.3.

Complex shape phase diagrams are also possible for fluid vesicles with fixed internal volume [175]. A feature of these morphologies is their non-convex shape. Such non-convexity has not been seen experimentally in the block copolymer systems studied here, leading us to believe that during the formation process solvent can freely enter and leave the system so that the internal volume is not conserved.

In conclusion, we have studied the fascinating morphology of nematic/smectic vesicles, such as the faceted tetrahedron, nanofibers, and ellipsoids using a simple toy model free energy[§]. Our theoretical and numerical studies provide the fundamental understanding of formation of these novel structured vesicles and elucidate the shape-selective mechanisms. It could also pave the way for formulating guiding principles in designing nanocarriers with specific shapes, particularly utilizing the two-dimensional nematic order and the topological defects, which are ubiquitous in closed vesicles.

Appendix 3.A Buckling of a LC membrane

We calculate the energy of a flat LC membrane with *radial* nematic configuration and a buckled one (a cone with cone angle $\pi - 2\theta$).

The Frank free energy is $F_{Frank} = \frac{1}{2}K \int (\nabla \cdot \vec{n})^2 d^2\vec{x}$. The bending energy is $F_{bending} = \frac{1}{2}\kappa \int H^2 d^2\vec{x}$.

The energy of a flat nematic disk with radius R is:

$$F_{flat} = F_{Frank} = \pi K \ln(R/a). \quad (3.9)$$

The energy of a buckled nematic disk is

$$F_{buckled} = F_{Frank} + F_{bending} = \pi K \ln(R/a) \cos \theta + \frac{\pi}{4} \kappa \frac{\sin^2 \theta}{\cos \theta} \ln(R/a). \quad (3.10)$$

By buckling, the Frank free energy decreases by $\cos \theta$ at the price of the bending energy.

From $\frac{d(\delta F)}{d\theta} = 0$ with $\delta F \equiv F_{buckled} - F_{flat}$, we get the optimal value for θ as

$$\cos^2 \theta_{opt} = \frac{\kappa}{4K - 2\kappa}. \quad (3.11)$$

Some calculation shows that only $K > 3\kappa/4$ (or, the bending rigidity is small enough in comparison with K) s.t., buckling is possible. Note: $\cos^2 \theta_{opt} < 0$ for $K < \kappa/2$

[§] We note that other more complicated shapes may arise if we consider a more general model free energy where both bending rigidities and Frank constants are anisotropic.

and $\cos^2 \theta_{opt} > 1$ for $K \in (\kappa/2, 3\kappa/4)$. These are unphysical solutions, indicating that weak K is insufficient to buckle a nematic disk?

One difference between a crystalline membrane and a nematic membrane is that the functional forms of the energy for flat case are different. The former one is proportional to R^2 , while the latter case is proportional to $\ln(R/a)$. In the former case, there exists a critical R , while there is no in the latter case. The ratio of K/κ controls the buckling in a nematic disk.

Appendix 3.B Discrete Frank free energy of 2-dimensional nematic

The free energy density associated with the nematic order in 2-dimensional texture can be written as [11]

$$f = \frac{K}{4s^2} [\partial_k Q_{ij} \partial_k Q_{ij} + \frac{2\epsilon}{s} Q_{ij} \partial_i Q_{kl} \partial_j Q_{kl}], \quad (3.12)$$

where the order parameter tensor for 2-dim nematics is $Q_{ij} = s(n_i n_j - 1/2 \delta_{ij})$ and $\epsilon = (K_3 - K_1)/(K_3 + K_1)$. K_1 and K_3 are the in-plane splay ($\nabla \cdot \vec{n}$) and bend ($\vec{n} \times (\nabla \times \vec{n})$) rigidities. $i, j = 1, 2$. $\vec{n}^2 = 1$.

Eq.(3.12) can be written in terms of the director \vec{n} . By making use of $n_i \partial_k n_i = 0$, $n_i n_i = 1$ and the expression for Q_{ij} , we have

$$\frac{1}{s^2} \partial_k Q_{ij} \partial_k Q_{ij} = 2(\partial_k n_j \partial_k n_j) = 2(\nabla \vec{n})^2 = 2[(\nabla \times \vec{n})^2 + (\nabla \cdot \vec{n})^2]. \quad (3.13)$$

The last step can be proved by expanding $\partial_k n_j \partial_k n_j$ and using the expression $\partial_i n_2 = -\frac{n_1}{n_2} \partial_i n_1$ due to $\vec{n}^2 = 1$. The first term is the bend deformation (as twist vanishes in 2-dim case) and the second one is the splay. This is the one-parameter Frank free energy.

Similarly, we have

$$\begin{aligned} \frac{1}{s^3} [Q_{ij} \partial_i Q_{kl} \partial_j Q_{kl}] &= 2n_i n_j \partial_i n_l \partial_j n_l - \partial_i n_l \partial_i n_l \\ &= 2(\vec{n} \cdot \nabla \vec{n})^2 - [(\nabla \times \vec{n})^2 + (\nabla \cdot \vec{n})^2]. \end{aligned} \quad (3.14)$$

For 3-dim nematics, we have

$$\vec{n} \times (\nabla \times \vec{n}) = \varepsilon_{ijk} n_i (\varepsilon_{jlm} \partial_l n_m) = -\vec{n} \cdot \nabla \vec{n}. \quad (3.15)$$

The 2-dim nematics may be regarded as a special 3-dim nematics with $n_3 = 0$. So Eq.(3.15) holds for 2-dim nematics. Note that the LHS of Eq.(3.15) is the bending of directors, and the RHS is the parallel transport of the director along the curve whose tangent is the director. A nicer derivation for Eq.(3.15): on 2-dim geometry, there is no twisting ($\vec{n} \cdot (\nabla \times \vec{n}) = 0$). If there is no bending ($\vec{n} \times (\nabla \times \vec{n}) = 0$), then $\nabla \times \vec{n} = 0$, i.e., $D_a n_b = D_b n_a$. By using this property, we have $\vec{n} \cdot \nabla \vec{n} = n^a D_a n_b = n^a D_b n_a = 0$ since $D(n^2) = 0$. The independent number of components of the director \vec{n} reduces to zero by the constraints of $n^2 = 1$, $\vec{n} \cdot (\nabla \times \vec{n}) = 0$, $\vec{n} \times (\nabla \times \vec{n}) = 0$. The final configuration of directors free of bending on 2-dim geometry is always along the geodesics.

Eq.(3.15) becomes

$$\frac{1}{s^3} [Q_{ij} \partial_i Q_{kl} \partial_j Q_{kl}] = (\nabla \times \vec{n})^2 - (\nabla \cdot \vec{n})^2. \quad (3.16)$$

By inserting Eq.(3.13,3.16) int Eq.(3.12), we have

$$f = \frac{K}{4} [(2 - 2\epsilon)(\nabla \cdot \vec{n})^2 + (2 + 2\epsilon)(\nabla \times \vec{n})^2]. \quad (3.17)$$

It can be checked that $\epsilon = (K_3 - K_1)/(K_3 + K_1)$. For $K_1 = K_3$ (one parameter Frank free energy), the ground state of nematics on sphere is that the four $+1/2$ defects are equally spaced on the sphere, at the vertices of tetrahedron [40]. For $K_3 \gg K_1$ (smectic regime), the splay deformation will dominate over bending, s.t., the four $+1/2$ defects will be on the equator of sphere [176]. For $K_3 < 0$, the bending deformation will lower the energy, and the ground state would be expected as that the directors compose a hexatic structure.

We will derive the discrete version of the Frank free energy Eq.(3.12). The surface can be represented by N random points $M_i (i = 1, 2, \dots, N)$ composing the simplicial lattice. To each point M_i , we can associate the closed cell C_i of those points which

are nearer to M_i than to any $M_j (i \neq j)$ [177]. The vertices of cells are denoted as a, b, c, \dots composing the dual lattice. Point a lives on the plaquette M_i, M_j, M_k (2-simplex) composing a triangle Δ_{ijk} . Triangle Δ_{ijk} is the approximation of the tangent plane at site a where the directors live.

The local coordinates at site a is defined as $\{\vec{e}_1 = \hat{e}_{ab}, \vec{e}_2 = \hat{e}_{ac}\}$. \hat{e}_{ab} is along $\vec{X}(b) - \vec{X}(a)$, in which $\vec{X}(a)$ is the position vector of site a .

$$\frac{1}{s} \partial_1 Q_{ij} = \frac{Q_{ij}^b - Q_{ij}^a}{d_{ab}}. \quad (3.18)$$

$$\frac{1}{s} \partial_2 Q_{ij} = \frac{Q_{ij}^c - Q_{ij}^a}{d_{ac}}. \quad (3.19)$$

$$\begin{aligned} \frac{1}{s^2} (\partial_k Q_{ij})^2 &= \frac{1}{d_{ab}^2} (n_i^b n_j^b - n_i^a n_j^a)^2 + \frac{1}{d_{ac}^2} (n_i^c n_j^c - n_i^a n_j^a)^2 \\ &= \frac{1}{a^2} [(N_{ij}^b - N_{ij}^a)^2 + (N_{ij}^c - N_{ij}^a)^2] \\ &= \frac{1}{a^2} [(N_{ij}^b - N_{ij}^a)(N_{ji}^b - N_{ji}^a) + (b \rightarrow c)] \\ &= \frac{1}{a^2} (Tr[(N^b - N^a)(N^b - N^a)] + (b \rightarrow c)) \\ &\Rightarrow \frac{2}{a^2} \sum_{\langle a, b \rangle} Tr[(N^b - N^a)(N^b - N^a)]. \end{aligned} \quad (3.20)$$

The sum is over neighboring sites a, b . Tr is over i, j . In the derivation, d_{ab} and d_{ac} are replaced by the average distance a between neighboring sites. It will be recovered later. $N_{ij} = n_i n_j (i, j = 1, 2)$ is a tensor of second order defined on surface.

For $i = 1, j = 2$,

$$\begin{aligned} \frac{1}{s^3} Q_{ij} \partial_i Q_{kl} \partial_j Q_{kl} &= \frac{1}{s^3} Q_{12} \partial_1 Q_{kl} \partial_1 Q_{kl} = N_{12}^a a^{-1} (N_{kl}^b - N_{kl}^a) a^{-1} (N_{kl}^c - N_{kl}^a) \\ &= a^{-2} Tr[(N^b - N^a)(N^c - N^a)]. \end{aligned} \quad (3.21)$$

So the sum over i, j gives rise to:

$$\begin{aligned} \frac{1}{s^3} Q_{ij} \partial_i Q_{kl} \partial_j Q_{kl} &= a^{-2} \left\{ (N_{11}^a - \frac{1}{2} + N_{22}^a - \frac{1}{2}) Tr[(N^b - N^a)^2] + (b \rightarrow c) \right. \\ &\quad \left. + 2N_{12}^a Tr[(N^b - N^a)(N^c - N^a)] \right\} \\ &\Rightarrow \frac{1}{2} \times \frac{2}{a^2} \sum_{\langle a, b, c \rangle} N_{12}^a Tr[(N^b - N^a)(N^c - N^a)]. \end{aligned} \quad (3.22)$$

In the last step, we use $\frac{1}{s}Tr[Q] = N_{11} + N_{22} - 1 = 0$, so the first two terms vanish. $N_{12}^a = \hat{e}_{ab} \cdot N^a \cdot \hat{e}_{ac}$. The prefactor 1/2 in the last expression is due to the double sum of $\langle a, b, c \rangle$ and $\langle a, c, b \rangle$.

Eq.(3.12) can finally be written as a discrete form

$$\int dAf = \frac{K}{4} S_a \left\{ d_{ab}^{-2} \sum_{\langle a, b \rangle} Tr[(N^b - N^a)(N^b - N^a)] + \right. \quad (3.23)$$

$$\left. \epsilon \sum_{\langle a, b, c \rangle} d_{ab}^{-1} d_{ac}^{-1} (\hat{e}_{ab} \cdot N^a \cdot \hat{e}_{ac}) Tr[(N^b - N^a)(N^c - N^a)] \right\}.$$

S_a is the area of plaquette a . The integral of free energy density over the whole surface is converted into the sum of energies associated with plaquette.

For both 2-dimensional and 3-dimensional smectics, we have no twist deformation [178]. The free energy of 2-dim smectics includes two parts: a nematics contribution and a 1-dim solid contribution (the compression/dilation term). The second part will dominate over the first one for large-scaled system ($R \gg a$) by dimensional analysis. So we may forbid compression/dilation of layers (curves in 2-dim case) by requiring that the layer spacing as constant. On the other hand, the ‘‘incompressibility’’ of layers, i.e., $\oint \vec{n} \cdot d\vec{l} = 0$ (the total number of traversed layers by the closed loop is zero) leads to the vanishment of the bending deformation (see Chandrasekhar p310 or Kleman et al p145). Therefore, the Frank free energy of smectics only includes the splay term. In the real calculation, we may let $K_3 = \infty$, s.t., the directors will splay to avoid the bending deformation. By substituting $K_3 = \infty$ into the expression for ϵ , we have $\epsilon = 1$. Note that the splay energy vanishes for $\epsilon = 1$ (see Eq.(3.17)).

Appendix 3.C Discrete bending energy of isotropic vesicles

At high temperature, no order (nematics and smectics) is formed on vesicles and the elasticity of vesicles is isotropic.

The bending energy for isotropic vesicle is

$$E_b = k \int dA (2H)^2, \quad (3.24)$$

where the mean curvature $2H\hat{N} = Tr\vec{K}_{\alpha\beta}$. The curvature tensor on the surface $\vec{K}_{\alpha\beta} = D_\alpha D_\beta \vec{X} = D_\alpha \vec{t}_\beta$, which is proved to be parallel to the normal vector \hat{N} and is a symmetric tensor. Note that \vec{X} is a vector in $E3$, while it is a scalar for the surface.

$$(2H)^2 = (K_\alpha^\alpha)^2 = (D_\alpha D^\alpha \vec{X})^2 = (\Delta \vec{X})^2. \quad (3.25)$$

Note that in the last expression, the Laplacian defined on surface applies on a scalar. $(\Delta \vec{X})^2$ can be expressed in a discretized surface. In what follows, we will derive for the discrete version of the Laplacian applying on a scalar [177]

$$\frac{1}{2d} (-\Delta \varphi)_i = \sum_{j(i)} p_{j,i} \frac{\varphi_i - \varphi_j}{l_{ij}^2}, \quad (3.26)$$

where $p_{j,i} = \frac{1}{2d} \frac{\sigma_{ij} l_{ij}}{\sigma_i}$, $\varphi \in \mathcal{F}_0$, the 0-form (scalar function space) defined on sites M_i ($i = 1, 2, \dots, N$). l_{ij} is the length of bond ij . σ_i is the area of cell C_i . σ_{ij} is the length of edge perpendicular to the link ij . d is the dimension of surface.

A general definition for the Laplacian acting on a p-form is (In Ref.[179] the symbol for d^* is δ ; see also Ref.[177])

$$-\Delta_p = (d^*)d + d(d^*), \quad (3.27)$$

in which d is the exterior differential operator and its “hermitian adjoint” d^* transform a p-form into (p+1)-form and (p-1)-form respectively. Δ_0 is the ordinary Laplacian acting on scalar functions. For example, for $\varphi \in \mathcal{F}_0$, $(d\varphi)_{ij} = \frac{\varphi_i - \varphi_j}{l_{ij}}$, which is just the discrete version of derivative. For $\varphi \in \mathcal{F}_1$, $(d^*\varphi)_i = \frac{1}{\sigma_i} \sum_{j(i)} \sigma_{ij} \varphi_{ij}$. In deriving this equation, we use the duality of \mathcal{F}_p and $\tilde{\mathcal{F}}_{d-p}$, which is defined on the dual lattice (the cells as mentioned above) of the simplicial lattice composed of points M_i, M_j, M_k, \dots . The dual counterpart \tilde{d} of the exterior differential operator d is defined via. $\langle \varphi | \tilde{d}\psi \rangle = \langle d\varphi | \psi \rangle$, where $\psi \in \tilde{\mathcal{F}}_{d-p}$. After some calculation, we get

$$(-\Delta \varphi)_i = \frac{1}{\sigma_i} \sum_{j(i)} \frac{\sigma_{ij}}{l_{ij}} (\varphi_i - \varphi_j). \quad (3.28)$$

By inserting the expression for $p_{j,i}$ we get the more compact expression for $(-\Delta\varphi)_i$ as in Eq.(3.26).

By Eq.(3.26), we can write the bending energy in terms of \vec{X} in discrete form easily (p384 of Ref.[4]):

$$E_b = \frac{\kappa}{2} \int dA (\Delta \vec{X})^2 = \frac{\kappa}{2} \sum_i \frac{1}{\Omega_i} \left[\sum_{j(i)} (\vec{X}_i - \vec{X}_j) \right]^2, \quad (3.29)$$

where Ω_i is the sum of the areas of the surface triangles adjacent to site i . j are the neighbor sites of the site i . We use $N = 72$ (regular) sites to represent the sphere. The discrete bending energy formula gives $E_b = 26.5$, while the analytical result is $E_b = 8\pi = 24.8$ for $\kappa = 1$.

In what follows, we express the bending energy in terms of the normal vector \hat{N} .

$$(2H)^2 = (K_\alpha^\alpha)^2 = [\vec{t}^\alpha \cdot (\partial_\alpha \hat{N})]^2. \quad (3.30)$$

The last step is due to the Weingarten equation [4]

$$\partial_\alpha \hat{N} = K_{\alpha\beta} \vec{t}^\beta. \quad (3.31)$$

The projection of the Weingarten equation on \vec{t}^γ gives

$$\vec{t}^\gamma \cdot \partial_\alpha \hat{N} = K_{\alpha\beta} \vec{t}^\beta \cdot \vec{t}^\gamma = K_{\alpha\beta} g^{\beta\gamma} = K_\alpha^\gamma. \quad (3.32)$$

Eq.(3.30) can be written as a discrete form

$$[\vec{t}^\alpha \cdot (\partial_\alpha \hat{N})]^2 = [\vec{t}^\alpha(a) \cdot \frac{\hat{N}(b) - \hat{N}(a)}{\delta u^\alpha}]^2, \quad (3.33)$$

where point b is near point a in the \vec{t}^α direction, i.e.,

$$\partial_\alpha \hat{N} = \lim_{\delta u^\alpha \rightarrow 0} \frac{\hat{N}(b) - \hat{N}(a)}{\delta u^\alpha}. \quad (3.34)$$

The magnitude of $\hat{N}(b) - \hat{N}(a)$ should be small s.t., the limit converges to a *finite* quantity. Therefore, the dihedral angle θ of plaquette a and b should be big enough, or else the limit will diverge. Since $\hat{N}(b) \cdot \hat{N}(a) = -\cos\theta$, the bending energy is proportional to $\sin^2\theta$, which should be a small quantity. Due to the observation that

the bending energy of the discrete version Eq.(3.33) is invariant for $\theta \rightarrow \theta + \pi$, it can only describe mild bending deformation of discrete vesicle.

In order to characterize the large bending of discrete vesicle, we may *directly* consider a discrete vesicle instead of discretizing a smooth vesicle. Considering that the bending deformation is the tilt (in three dimensional Euclidean space \mathbb{E}^3) of normal vectors, the ansatz bending energy of discrete vesicle may be suggested as proportional to $[\hat{N}(a) - \hat{N}(b)]^2 \propto 1 - \hat{N}(a) \cdot \hat{N}(b)$. Such an ansatz satisfies the following requirements: (1) $\hat{N}(b) \rightarrow -\hat{N}(b)$ leads to different bending energies, (2) the bending energy vanishes as $\hat{N}(a) \parallel \hat{N}(b)$. Therefore, it could describe large bending deformation. In fact, its relation with the mean curvature can be found as follows. By the Weingarten equation Eq.(3.31), we have

$$\begin{aligned}
g^{\alpha\beta} \partial_\alpha \hat{N} \cdot \partial_\beta \hat{N} &= g^{\alpha\beta} (K_{\alpha\gamma} \bar{t}^\gamma) \cdot (K_{\beta\delta} \bar{t}^\delta) = g^{\alpha\beta} g^{\gamma\delta} K_{\alpha\gamma} K_{\beta\delta} \\
&= (g^{\alpha\gamma} g^{\beta\delta} + \gamma^{\alpha\delta} \gamma_{\rho\lambda} g^{\rho\beta} g^{\lambda\gamma}) K_{\alpha\gamma} K_{\beta\delta} \\
&= (g^{\alpha\gamma} K_{\alpha\gamma})^2 + \gamma^{\alpha\delta} \gamma_{\rho\lambda} K_\delta^\rho K_\alpha^\lambda \\
&= (2H)^2 - 2K_G.
\end{aligned} \tag{3.35}$$

In the last step, we use $K_G = \det(K_{\alpha\beta}) = \frac{1}{2} \gamma^{\delta\alpha} \gamma_{\rho\lambda} K_\delta^\rho K_\alpha^\lambda$. $\gamma^{\alpha\beta} = \frac{1}{\sqrt{g}} \varepsilon^{\alpha\beta}$. The discrete version of $g^{\alpha\beta} \partial_\alpha \hat{N} \cdot \partial_\beta \hat{N}$ is:

$$\left(\frac{\hat{N}(b) - \hat{N}(a)}{d_{ab}} \right)^2 = 2(d_{ab})^{-2} (1 - \hat{N}(b) \cdot \hat{N}(a)). \tag{3.36}$$

Chapter 4

Planar sheets meet negative curvature liquid interfaces

In this chapter, we analyze the geometric frustration arising in elasto-capillary systems when planar inextensible elastic sheets are wrapped on negative curvature substrates. We also propose a design for generating negative curvature liquid interfaces. Both concentric wrinkles and eye-like folds are shown to be compatible with negative curvatures. We discuss both types of geometric frustration and the phase diagram controlling their appearance.

4.1 Introduction

Geometric frustration occurs in wrapping a spherical Mozartkugel (“Mozart sphere”) with a planar foil [180, 181, 182]. The geometric incompatibility of a planar sheet and a curved substrate gives rise to ridges in a process whereby energy is lowered by spontaneous condensation into a small region of the total available volume [55]. Recently the frustration of a thin circular elastic sheet of ~ 1 mm size covering the tip of a spherical droplet has been studied [56]. Fine radial wrinkles at the edge of the sheet become unstable to a few localized folds when the size of the spherical

droplet is reduced. The wrinkle-fold transition is analogous to the dislocation/pleat or disclination/scar transition in crystalline order on a capillary bridge as the curvature is increased [35, 57, 58]. The structure of topological defects on positive and negative curvature surfaces are fundamentally different [59]. This suggests a distinct wrinkle/fold structure on a flat sheet when attached to a negative curvature surface; the edge of the sheet is stretched tangentially as opposed to being compressed on spherical geometry. A completely different frustration pattern on the planar sheet is thus expected. In this chapter, we study the wrinkle/fold structure on a flat sheet attached to a negative curvature geometry in an elasto-capillary system.

The system we treat has two parts: a thin elastic hydrophilic sheet and a saddle-like fluid interface with negative curvature. The size of the elastic sheet is taken to be much bigger than the elasto-capillary length $\sqrt{\kappa/\sigma}$, so that surface tension σ dominates over the bending rigidity κ [183]. The thickness of the elastic sheet is taken to be much smaller than $\sqrt{\kappa/Y}$, where Y is the 2-dimensional Young's modulus, in which case it can be regarded as inextensible [184]. Note that a standard sheet of paper has this property and can be used to demonstrate the bending of a thin elastic sheet [185]. When such an inextensible elastic sheet is placed on a negative curvature liquid interface the capillary force pulls the planar sheet into full contact with the liquid interface. In this chapter we first propose a scheme to design a saddle-like fluid interface in a capillary tube and then discuss the possible wrinkle/fold patterns compatible with negative curvature.

4.2 Design a negative curvature surface in a capillary tube

A wetting liquid rises inside a capillary tube, as first observed and recorded by Leonardo da Vinci [60]. The liquid meniscus curves up (down) in a hydrophilic (hydrophobic) capillary tube, respectively. For both cases the curvature of the liquid

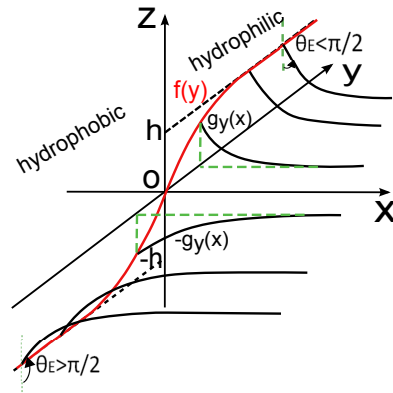


Figure 4.1: A wall made of hydrophilic and hydrophobic materials is immersed in a liquid. The liquid interface curves up in the hydrophilic part and down in the hydrophobic part. In the transition region, the liquid profile on the wall changes smoothly.

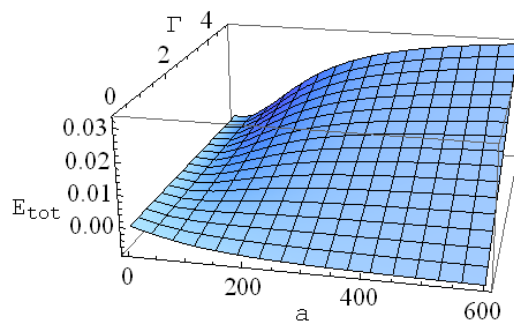


Figure 4.2: The total energy Eq.(4.1) versus the parameter a and the dimensionless quantity Γ . The parameter a indicates the steepness of the liquid profile on the wall in the transition region. Γ controls the competition between the contact energy and the gravitational potential energy.

interface is always positive. We will show that a saddle-like fluid interface can be realized on a capillary tube made of four alternating hydrophilic and hydrophobic slices. In order to illustrate the idea, we first consider a flat Janus wall made of two materials, one hydrophilic and one hydrophobic, immersed in a liquid. Far away from the connecting region the liquid interface will curve up (down) on the hydrophilic (hydrophobic) material, respectively. In the transition region, the liquid profile on the wall changes smoothly as schematically shown in Fig.4.1. The competition between the contact energy of the liquid and the wall and the gravitational potential energy determines the equilibrium shape of the liquid profile. We calculate these energies in the coordinate system indicated in Fig.4.1. The wall is on the $x = 0$ plane; the $y > 0$ ($y < 0$) region is hydrophilic (hydrophobic). The bulk liquid is in the $x > 0$ region, and the asymptotic plane of the liquid is the $z = 0$ plane. The liquid profile on the wall is denoted by $f(y)$ and that away from the wall along the x-direction is denoted by $g_y(x)$ as it is y-dependent. For simplicity, we consider the symmetric case of $\theta_E^- + \theta_E^+ = \pi$, where θ_E^\pm are the contact angles far way from the transition region, as shown in Fig.4.1. The total energy with respect to the reference state of a flat fluid interface is $E_{tot} = E_+ + E_-$, the sum of the energies in the regions of $y > 0$ (E_+) and $y < 0$ (E_-). $E_\pm = -I_\pm A_\pm + W_\pm$, where $I_\pm = \pm\gamma \cos \theta_E^\pm$ are the imbibition parameters, A is the contact area, and W is the gravitational potential energy. $A_+ = \int_0^\infty f(y)dy$, $A_- = \int_{-\infty}^0 (h + f(y))dy$, $W_+ = \frac{1}{2}\rho g \int_0^\infty dx \int_0^\infty dy g_y(x)^2$, and $W_- = -\frac{1}{2}\rho g \int_0^\infty dx \int_{-\infty}^0 dy [h^2 - g_y(x)^2]$. Since the liquid profile decays exponentially away from the wall [60], we may try an ansatz for $g_y(x)$: $g_y(x) = f(y) \exp(-\alpha x/\lambda_c)$, with the parameter α of order one. Here λ_c is the capillary length [60]. By inserting this ansatz into the expression for the total energy and dropping constant terms, we arrive at

$$E_{tot} = - \int_0^\infty \tilde{f}(y)dy + \frac{\Gamma}{h} \int_0^\infty \tilde{f}(y)^2 dy, \quad (4.1)$$

where $\tilde{f}(y) = f(y)/h$. The dimensionless parameter $\Gamma \equiv \rho g \lambda_c h / (4I\alpha)$ controls the competition between the contact energy and the gravitational potential energy. The

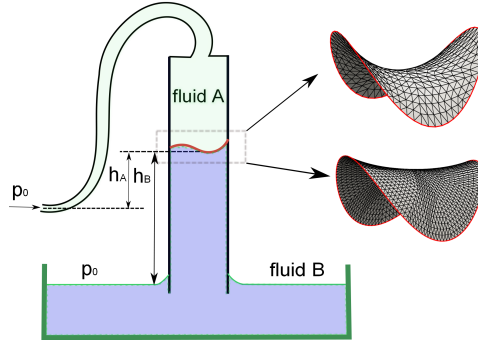


Figure 4.3: Design for generating constant mean curvature liquid menisci by controlling the pressure difference across the liquid interface through adjusting the heights h_A and h_B . Two shapes of liquid interface with vanishing mean curvature (above) and constant mean curvature (below) are shown. These shapes are generated with Surface Evolver [186].

desired $f(y)$ should not only minimize Eq.(4.1) but also smoothly connect the lines $z = \pm h$ and $f(y = 0) = 0$. The ansatz $f(y) = h \tanh(ay)$ nicely satisfies these requirements. The parameter a describes the steepness of the liquid profile on the wall; the profile is steeper for bigger a . Inserting the ansatz for $f(y)$ into Eq.(4.1) gives E_{tot} in terms of a and Γ , as plotted in Fig.4.2. The parameter Γ controls the shape of the liquid interface. For small Γ where the surface energy dominates $a_{optimal}$ is large and so the profile $f(y)$ is very steep. For large Γ where the gravitational potential energy dominates the profile $f(y)$ varies slowly as $a_{optimal}$ is small.

Now consider a capillary tube made of four alternating hydrophilic and hydrophobic slices azimuthally. The liquid profile around the inner wall of such an inhomogeneous capillary tube will curve up, down, up and down in sequence by contacting with the alternating hydrophilic and hydrophobic materials. By tuning the parameter Γ , a saddle-like shaped liquid meniscus with negative curvature can be formed in the capillary tube. Since the heights of points on the curved fluid interface are different, however, the pressure difference across the fluid interface $\Delta p(\vec{x}) = -\rho gh(\vec{x}) = 2\sigma H(\vec{x})$ and thus the mean curvature $H(\vec{x})$ over the fluid interface are spatially dependent [60]. The shape of the fluid interface cannot therefore be precisely controlled.

We propose a method to make constant mean curvature (CMC) liquid interfaces

in capillary tubes, so their shapes can be finely controlled. The idea is illustrated in the schematic plot Fig.4.3. Consider two immiscible fluids of identical density in a capillary tube, so the change of the interface shape does not influence the gravitational potential energy. The boundary of the liquid-liquid interface is anchored by pinning points on the capillary tube [60]. The pressure difference across the interface can be adjusted by tuning the heights h_A and h_B as indicated in Fig.4.3: $\Delta p = \rho g(h_B - h_A) = \rho g \Delta h$. It is a *constant for all points* over the liquid-liquid interface. Therefore, the mean curvature over the interface is constant. A variety of CMC liquid interfaces (including minimal surfaces with vanishing mean curvature) can be formed by adjusting the pressure difference across the fluid interface (via. Δh) and the anchoring profile on the capillary tube. Two typical shapes of $H = 0$ and $H \neq 0$ fluid interfaces with the boundary profile $f(\theta) \sim \cos 2\theta$ are shown in Fig.4.3. In particular, the shape of a minimal surface is uniquely determined by a spatial loop $\Gamma \equiv \vec{x}(\rho = 1, \theta)$ [187]: $\vec{x}(\rho, \theta) = \int_0^{2\pi} K(\rho, \phi - \theta) \vec{x}(\rho = 1, \phi) d\phi$, where the Poisson kernel $K(\rho, \alpha) = \frac{1}{2\pi} \frac{1-\rho^2}{1-2\rho \cos \alpha + \rho^2}$. In comparison to relatively evanescent soap films, the liquid interface made from solid liquids is rather stable [66]. It is therefore an ideal liquid substrate for studying the geometric frustration associated with sheets wrapped on curved surfaces. In addition, pre-designed negative curvature liquid interfaces may have extensive applications in studying the influence of negative curvature on crystalline/liquid crystal order [59], particle interactions [188, 189] and diffusion processes [190].

4.3 Patterns on sheets

4.3.1 Concentric wrinkles

Complete contact between a planar sheet and a curved fluid substrate by capillary forces introduces a wrinkle/fold pattern, which redefines the metric of the planar sheet according to the curvature of the background geometry. The modification of

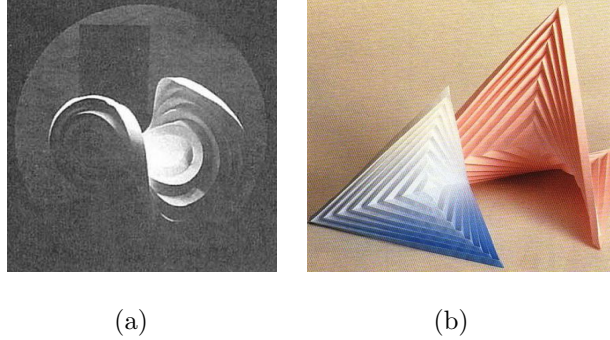


Figure 4.4: Wrinkles of alternating peaks and valleys on a piece of paper redefine the metric, automatically bringing the flat paper to a saddle-like shape. (a) is excerpted from Ref.[191], and (b) is from Ref.[192] where the method to make it is described in detail.

the metric leads to the change of shapes. This concept has been utilized to design responsive buckled surfaces [193]. The curved surface endows its metric to the flat sheet via their full contact. The inherited metric on the flat sheet as well as its elasticity determines the wrinkle/fold structure. Which wrinkle/fold patterns are compatible with negative curvatures? The art of origami provides some inspiration. It is shown in origami that regular concentric or square wrinkles with alternating peaks and valleys on a piece of paper can induce a negative curvature as demonstrated in Fig.4.4.

In what follows, we will prove that the effect of concentric wrinkles is equivalent to inserting a wedge of some angle. The wavelength and amplitude of the concentric wrinkles determine the angle of the wedge. The wrinkled sheet is parameterized as $\vec{x}(r, \theta) = \{r \cos \theta, r \sin \theta, a_k \cos(kr)\}$, where a_k is the amplitude of the wrinkles and k is the wavenumber $k = 2\pi/\lambda$. The nonzero components of the metric tensor are $g_{11} = 1 + x^2 \sin^2(kr)$ and $g_{22} = r^2$, where $x = a_k k$. The imposed wrinkles transform the original wrinkled shell into a new surface denoted by Σ that we take coincident with the curved substrate. On this new surface the metric is redefined such that the geodesic distance (denoted as r) from the center of the disk to the first peak is $r_0 = \lambda$. The corresponding real distance on the original sheet is $l_0 = \int_0^\lambda \sqrt{g_{11}} dr = \frac{1}{k} E(x)$,

where $E(x) = \int_0^{2\pi} dy \sqrt{1 + x^2 \sin^2 y}$. As $a_k \rightarrow 0$, $l_0 \rightarrow \lambda$, as expected. Due to the in-extensibility of the paper model, the mapping from the originally flat sheet to a wrinkled shape is isometric and thus length-preserving. The perimeter of the circle with radius r in the new surface Σ is thus $C(r) = 2\pi l(r) \equiv 2\pi r + r\alpha$, where $l(r) = l_0 k r / (2\pi)$. The angle of the inserted wedge α is:

$$\alpha = \left(\frac{l_0}{\lambda} - 1\right)2\pi > 0. \quad (4.2)$$

The positive sign of α indicates that concentric wrinkles are equivalent to *inserting* a wedge. The inserted wedge buckles a flat disk to a saddle-like shape with negative curvature in 3-dimensional Euclidean space [184], as do concentric wrinkles. These two ways of introducing negative curvature - either inserting material or imposing concentric wrinkles - are related via the expression for $C(r)$. The first method changes the perimeter without changing the radius, while it is the converse for the second method. By expanding the expression for l_0 in terms of small x , one finds $C(r) = 2\pi r + \frac{\pi}{3}k^2x^2r^3 + \mathcal{O}(x)$. By inserting this into $K_G = \lim_{r \rightarrow 0} 3[2\pi r - C(r)]/(\pi r^3)$ [6], the curvature at the center of the surface Σ is found to be

$$K_G = -a_k^2 k^4. \quad (4.3)$$

Eq.(4.3) shows that increasing the amplitude or the frequency of the concentric wrinkles results in greater curvature of the surface, with greater sensitivity to the frequency. The curvature of the background geometry determines the amplitude and wavelength of the concentric wrinkles according to the product $a_k^2 k^4$.

It is worth mentioning that by increasing (“growing”) the radius of a flat disk while keeping the perimeter invariant, we get a positive curvature surface, which may buckle to various patterns depending on its elasticity. This elasticity paradigm explains the phyllotactic patterns of Fibonacci-like sequences on plants [194]. Wrinkles of concentric squares can also buckle a square piece of paper to a beautiful hyperbolic parabola with negative curvature as shown in Fig.4.4(b). Prescribed metrics via the

design of wrinkles transforms a flat piece of paper into a rich variety of structures, including the DNA double helix [195].

4.3.2 Eye-like folds

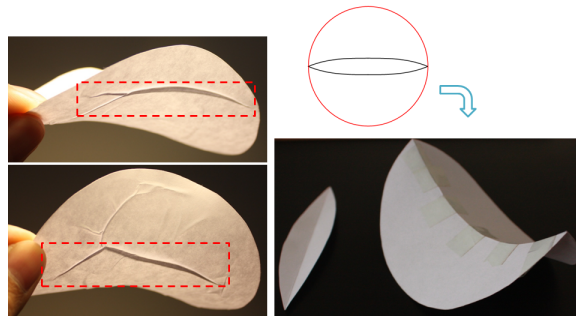


Figure 4.5: A branch-like fold pattern appears on a flat paper disk by wrapping it on a negative curvature surface (left figures). The folds in the red rectangles are equivalent to removing eye-like areas as shown in the upper right figure. The buckled shape (the lower right figure; the leaf-like object therein is the removed material) of a flat disk due to an isolated fold is obtained by “closing the eye”.

In addition to wrinkles, localized folds can also change the metric [57]. By attaching a paper disk onto a negative curvature surface, typical branch-like fold patterns are found as in Fig.4.5 (the left two photos are the same deformed paper disk from different perspectives). A light beam directly illuminates the paper disk from above, so the folds are seen clearly as black curves. The folds on the sheet can be roughly classified as principal ones (in the red rectangles) and fine ones (barely seen above the red rectangle in the left below figure). Their roles in “screening” curvature are similar to disclinations and dislocations in crystalline order on a curved surface, respectively [59]. The feature of the observed folds is that the amount of the folded material decreases towards their ends. Similar folds are also found in the interior side of a bent tube where the curvature is negative [196]. We analyze an isolated fold for illustrating that it is compatible with a negative curvature geometry. The effect

of such folds is to remove an eye-like area from a flat disk. The buckled shape (see the lower right figure in Fig.4.5) due to the fold, or equivalently the removal of an eye-like area, is obtained by “closing the eye”. The curvature of the buckled shape is negative; the disk curves up along the fold and curves down along the orthogonal direction. The removal of an eye-like area is equivalent to inserting a wedge, because more material is removed at the center than on the edge. The profile of the eye-like fold can be determined by the curvature of the background geometry. The perimeter of a circle with geodesic radius r on a disk with an eye-like area removed is estimated as $C(r) \approx 2\pi r + 4(h(0) - h(r))$, where $2h(r)$ is the width of a fold. For a small-sized fold (in comparison with $\sqrt{1/|K_G|}$), $h(r) = h(0) + \frac{\pi}{12}K_G r^3$ by inserting $C(r)$ into the expression for the Gaussian curvature. From $h(r = L/2) = 0$, we derive the length of the fold $L = 2(\frac{12h(0)}{\pi|K_G|})^{1/3}$ as controlled by the curvature. In contrast, it is interesting to notice that reversed eye-like folds are found in one’s palms. It seems that the two main lines - head line and heart line following the terminology of palmistry - are compatible with positive curvatures as the width of these lines increases from the center to the edge of a palm.

4.3.3 Phase diagram

In what follows, we study the transition between the wrinkle and fold solutions. In the regime of large surface tension (in comparison with the bending rigidity), the ground state of an elasto-capillary system is dominated by the surface energy difference before and after a planar sheet is attached to the liquid interface: $F = \sigma_{LA}A_{sheet} + \sigma_{LS}A_{coverage} - \sigma_{LA}A_{substrate} = -\sigma_{LS}A_{coverage} + \text{const.}$ σ_{IJ} is the surface tension between phases I and J with L, A and S standing for liquid, air and elastic sheet respectively. $A_{coverage}$ is the area of the liquid substrate occupied by the elastic sheet, which is smaller than the area of the sheet A_{sheet} due to its deformation. $A_{substrate}$ is the sum of the occupied and unoccupied substrate areas, which is a constant. The surface energy turns out to depend only on $A_{coverage}$; the larger it

is, the smaller the energy is. Unlike a planar sheet on a positive curvature surface, the deformation at the edge of a planar sheet on a negative curvature surface may be ignored. Therefore, the optimal contour shape of a deformed sheet on the liquid substrate is the one that maximizes the coverage area while keeping the perimeter fixed. This is exactly the classical isoperimeter problem, on a negative curvature surface in this case. For constant curvature surfaces, the classical isoperimetric solution in the Euclidean plane is also valid with the circle in \mathbb{E}^2 being replaced by a geodesic circle [197]. On a general surface with varying negative curvature, there is no exact mathematical result available. The physical picture, however, is rather interesting: a deformed sheet fully attached on a curved liquid substrate will migrate to the region where it can extend as far as possible to maximize the contact area; the driving forces are the capillary force and the release of the bending energy in this curvature-driven migration process. We resort to numerical methods to solve the isoperimetric problem on a general slightly curved surface which is represented by $z(x, y) = \alpha x^2 - \beta y^2$. The solution space of the isoperimetric problem consists of contours of deformed in-extensible sheets on the liquid substrate. These contour shapes can be generated by projecting planar loops in the x-y plane onto the surface $z(x, y)$. For the slightly curved liquid substrate, the planar generating loops are slightly deviated from a circle, which is represented by ellipses $x^2/a^2 + y^2/b^2 = 1$. The solution to the isoperimetric problem is therefore characterized by the parameters $\{a, b\}$ for given $\{\alpha, \beta\}$ which characterize the shape of the liquid substrate. Note that a and b are not independent due to the isoperimetric constraint; the solution space is therefore one-dimensional for a given substrate geometry.

The two distinct deformed states, folds and wrinkles, on a sheet can be distinguished by the isometry condition as follows. The in-extensibility of a sheet sets an upper limit $2R$, the diameter of the planar sheet, as the maximal geodesic distance between two arbitrary points on a sheet contour. If the determined sheet contour has the maximum geodesic diameter equal to (smaller than) $2R$, then the sheet is

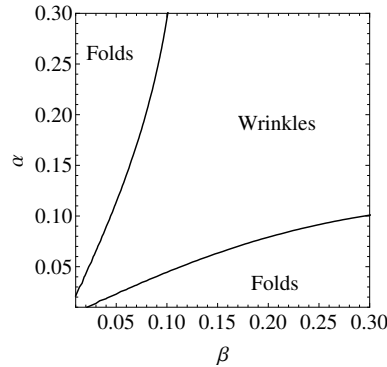


Figure 4.6: The phase diagram of a deformed sheet on a negative curvature surface. Wrinkles on the sheet occur near the isotropic region ($\alpha/\beta \approx 1$) while folds are found in the highly anisotropic regions (α/β far from unity). The smallness of α and β as measured by the radius of the sheet guarantees that the surface is only slightly curved.

recognized as having folds (wrinkles) on it. An isotropic Gaussian curvature ($\alpha = \beta$, since $K_G = f(\alpha x^2 + \beta y^2)$ [6]) imposes either isotropic tangential stretching or isotropic radial compression on the sheet, which is expected to result in wrinkles. As the Gaussian curvature grows increasingly anisotropic (the ratio α/β deviates from unity), the imposed anisotropic stretching and compression on the sheet are expected to generate folds which are themselves anisotropic objects. These expectations are verified in the numerical calculation which is summarized in the phase diagram in Fig.4.6. This shows that wrinkles occur near the isotropic region while folds arise in the highly anisotropic regions.

4.4 Conclusion

In conclusion, we study the curvature-driven wrinkle/fold pattern on a flat sheet. We analyze the geometric feature of concentric wrinkles and eye-like folds on planar sheets that are compatible with negative curvature liquid substrates, and discuss the transition of these two states driven by the anisotropy of the background geometry. The ability of wrinkles/folds to deform a plane to a curved surface may find potential

applications. Consider a flat sheet with a pre-designed wrinkle/fold pattern like lines on a palm. By controlling the on/off status of the wrinkles/folds, a planar sheet can be programmed to buckle to a desired shape. It may lead to potential applications in maximizing the sunshine harvest by designing the shape of ultrathin flexible solar cells [198]. Our study also sheds light on the reverse problem of attaching a curved shell onto a flat substrate, e.g., the adhesion of a cell onto a flat substrate [199].

Chapter 5

The instabilities of toroidal droplets. I: Rayleigh instability

Motivated by the recent beautiful experiment on toroidal liquid droplets [200], we theoretically study the instabilities of toroidal droplets. In that experiment, toroidal liquid droplets of different aspect ratios are made which are immersed into another distinct liquid. It is observed that, about 10 seconds after being prepared, fat toroidal liquid droplets shrink to a single spherical bead, while thin toroidal droplets are divided into a certain number of evenly distributed beads, which is determined by the aspect ratio, before shrinking to a single bead. The latter phenomenon can be well understood as Rayleigh instability, since the local geometry of thin torus approaches that of cylinder [201] [202]. In this chapter, we discuss the Rayleigh instability for thin tori and in the next chapter we discuss the shrinking mode.

5.1 Introduction

Liquid droplets are ubiquitous in nature and technology: rain, clouds, paint, lubricant, ink, dye, oil and so on [60, 203]. Our understanding of the liquid droplet system benefits greatly from the concept of surface tension introduced two hundred years by

Johann Andreas von Segner, a Hungarian mathematician [80]. In terms of surface tension, much of the behavior of liquid droplets, including statics and dynamics in different environments, is well understood [60, 65, 81]. The existence of surface tension not only minimizes the area of liquid droplet to reduce the surface energy, but also supports the propagation of an elastic mode: capillary wave [81]. External perturbations excite capillary waves propagating on the liquid surface. For example, a breeze or a toss of a stone ripple a water surface. The excited capillary wave will either grow or decay with time. The system becomes unstable for the former case. The underlying mechanism of such capillary instability originates from the surface tension-driven flow. If the flow amplifies the amplitude of the excited capillary wave, then the system becomes unstable [204]. For small perturbations, the excited capillary wave can be linearly decomposed into Fourier modes. The fastest growing mode of the capillary wave is exactly the most unstable one. The capillary instability of a liquid droplet has been of great scientific interest [61, 77], and it has extensive applications in industry [205].

Many factors influence the capillary instability of liquid droplet. For example, the wavelength of capillary wave, the viscosity of bulk liquid, the geometry of interface and so on. Experience tells us that the ripples on a flat surface will fade away sooner or later. In contrast, ripples on a curved surface may divide the bulk liquid droplet into sections. For example, water streams on the shield window of a car are observed to be broken into many droplets. One may wonder: how do different modes of capillary wave grow in time? What is the surface tension-driven flow like? How does the viscosity of fluid get involved in? In what way the geometry of interface plays a role? We will address these questions in this chapter and the following one.

The capillary instability of liquid droplets has attracted physicists' interest dating back to the beginning of the 19th century [61]. For experimental development and numerical simulation about the capillary instability, one may refer to Ref. [61, 205, 206, 207, 208]. The instability phenomenon of liquid droplet was distinctly noticed by

Savart. Later, following the earlier work by Plateau who showed that a long cylindrical liquid is unstable to disturbances with wavelengths greater than its circumference, Rayleigh explored theoretically the instability of a long cylindrical column of an incompressible fluid of both ideal and viscous without surrounding fluids based on a linearized stability analysis [201, 209]. Rayleigh solved for the dispersion relation, from which the fastest growing mode was predicted. Rayleigh's theory is linear that is applicable for perturbation of very small amplitude. And both the inertial effect of liquid and the external fluid are ignored. The more general case of a perturbed cylindrical liquid droplet immersed in another viscous liquid was studied by Tomotika by adopting the same scheme as Rayleigh: solving the Navier-Stokes equation under boundary conditions of velocities and forces [202]. The relation of fastest growing mode and the ratio of viscosities of the two fluids is obtained. The prediction for the fastest growing mode agrees with experiment very well, although it is based on linear theory which works near the onset of instability. This fact implies that the most unstable mode has been locked by the system from the very beginning of the occurrence of instabilities.

Although the fastest growing mode of the cylindrical interface separating two viscous fluids has been found by Tomotika, more detailed information about the dynamics of the system is not available in Tomotika's theory, such as the flow pattern in two fluids, the structure of vorticity field, and the information of how different processes (undulation of interface and shear dissipations in two fluids) compete to give rise to the fastest growing mode. While, for example, the information of flow pattern in fluids is important theoretically and practically. Theoretically, with the knowledge of flow in fluids one can calculate relevant physical quantities (for example, the vorticity field) and better understand how the system responds to external perturbations. Practically, with the velocity field known, one can better control the system. It is of vital importance for the design of microfluidic devices [210].

In this chapter, we propose a new scheme based on the principle of energy con-

servation to address the surface tension-driven instability of liquid droplets. Due to the approved validity of linear theory in the instability analysis of liquid droplets, we only concern perturbations of small amplitude. In order to simplify the problem, we work in the Stokes flow regime, which will be discussed later. According to the new scheme, the system gains energy from the unstable modes which is converted into kinetic energy and heat (due to shear dissipation). In the Stokes flow regime, the rate of change of the kinetic energy can be ignored. By equating the change rate of surface energy and the dissipation rate, we obtain the dispersion relation of the system and the most unstable mode. We will see that the principle of energy conservation will guide the system to evolve along the trajectory of maximum gain of surface energy and minimum dissipation.

5.2 Free energy

The thermodynamic property of the interface of two immiscible fluids is completely characterized by the surface tension σ . The increase of the free energy of an interface is

$$\Delta F(k) = \sigma \Delta A, \quad (5.1)$$

where $\Delta A = A - A_0$ is the difference of the area of perturbed and unperturbed interfaces, and k is the wavenumber of the perturbation. If $\Delta F(k)$ is positive, then the corresponding mode is stable: the perturbed interface prefers to recovering its original unperturbed shape. Or else the mode is unstable. In order to obtain the change of the area of an interface, we will examine its geometry.

5.2.1 Geometry of toroidal interfaces

The 3-dimensional toroid is characterized by $\{u^1 = \alpha, u^2 = \theta, u^3 = r\}$. α is the angle around the tube, θ is the angle around z-axis, and R_2 is the radial length. A point in

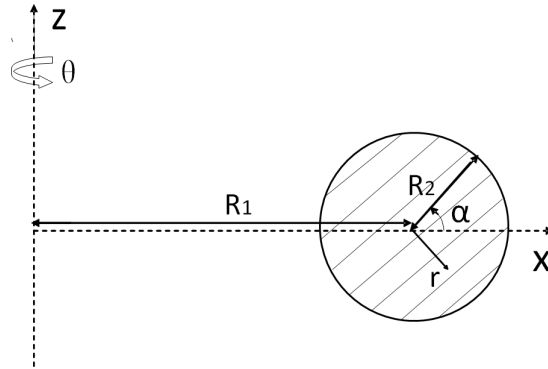


Figure 5.1: The geometric characterization of torus. A torus is produced by rotating the circle around the vertical axis.

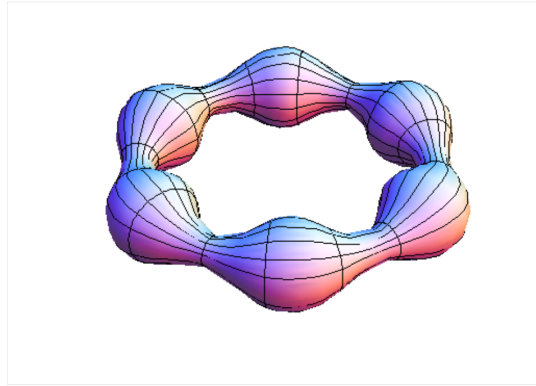


Figure 5.2: A perturbed torus.

3-dimensional space is

$$\vec{x}(\alpha, \theta, r) = \begin{pmatrix} (R_1 + r \cos \alpha) \cos \theta \\ (R_1 + r \cos \alpha) \sin \theta \\ r \sin \alpha \end{pmatrix}.$$

Fig.5.1 shows the x-z plane. $\theta = 0$ for the half $x > 0$ plane. The non-zero components of metric tensor of torus are

$$g_{11} = r^2, \quad g_{22} = (R_1 + r \cos \alpha)^2, \quad g_{33} = 1, \quad (5.2)$$

based on which the surface area and volume of the toroid can be derived.

For generality, we consider a toroidal interface with non-circular cross-section, so R_{20} becomes α dependent. With the metric of torus given, we can calculate the volume of toroid

$$V = \int R_2(R_1 + R_2 \cos \alpha) d\alpha d\theta dR_2 = 2\pi R_1 \int \frac{1}{2} R_{20}^2(\alpha) d\alpha + \frac{2\pi}{3} \int R_{20}^3(\alpha) \cos \alpha d\alpha \quad (5.3)$$

Note that the integration interval for R_2 is from $R_2 = 0$ to $R_2 = R_{20}(\alpha)$. The surface area of the torus surface is

$$A = \int R_2(R_1 + R_2 \cos \alpha) d\alpha d\theta = 2\pi R_1 \int R_{20}(\alpha) d\alpha + 2\pi \int R_{20}^2(\alpha) \cos \alpha d\alpha \quad (5.4)$$

The first terms for V and A are the corresponding volume and surface area of cylinder of length $2\pi R_1$. The second terms arise due to distinct geometry of torus. For circular cross section $R_{20}(\alpha) = R_{20}$, $V = 2\pi^2 R_1 R_{20}^2$ and $A = 4\pi^2 R_1 R_{20}$.

An axial perturbation about z-axis of small amplitude u_k ($u_k \ll a$) can be represented by

$$R_2(\alpha) = a + u_k \cos(n\alpha), \quad (5.5)$$

where n is an integer due to the toroidal geometry (see Fig.5.2). The wavenumber is $k \equiv n/R$. Note that the value of a differs from the radius of the tube for unperturbed torus R_{20} . The volume of the perturbed torus is $V = \int \sqrt{g} dr d\theta d\phi = (2a^2 + u_k^2)\pi^2 R$, where g is the determinant of the metric tensor g_{ij} ($i, j = 1, 2, 3$) of the volume. The volume of the unperturbed torus is $V_0 = 2\pi^2 R_1 R_{20}^2$. The conservation of volume during the deformation of torus modifies a : $a = R_{20}(1 - \frac{u_k^2}{4R_{20}^2})$. The surface area of perturbed torus is $A = \int \sqrt{g} d\theta d\alpha$, in which g is the determinant of metric tensor g_{ij} ($i, j = 1, 2$) of the interface. We expand \sqrt{g} with respect to the small perturbation amplitude u_k as $\sqrt{g} = c_0 + c_1 u_k/R_{20} + c_2 u_k^2/R_{20}^2 + \mathcal{O}(u_k^3/R_{20}^3)$. The integration of the first three terms gives $4\pi^2 R/R_{20}$, 0 and $u_k^2(-1 + \frac{k^2 R R_{20}}{\sqrt{(R/R_{20})^2 - 1}})\pi^2 R/R_{20}^3$, respectively. Since the area of unperturbed torus is $A_0 = 4\pi^2 R R_{20}$, the change of surface area $\Delta A = A - A_0$ of torus due to the perturbation u_k by Eq.(5.5) is

$$\Delta A = \pi^2 \frac{R_1}{R_{20}} \left(-1 + \frac{k^2 R_1 R_{20}}{\sqrt{(R_1/R_{20})^2 - 1}}\right) u_k^2 + \mathcal{O}(u_k^4). \quad (5.6)$$

For comparison, we will also discuss the geometry of a cylindrical surface. Note that as $R_1/R_2 \rightarrow \infty$, a toroidal surface becomes cylindrical locally. From the cylindrical coordinates $\{u^1 = r, u^2 = \theta, u^3 = z\}$, we have the non-zero components of the metric tensor:

$$g_{11} = 1, g_{22} = r^2, g_{33} = 1, \quad (5.7)$$

from which the surface area and the volume can be derived. The change of surface area for a cylinder with length L which is subject to perturbation $r(z) = a + u_k \cos(kz)$ is

$$\Delta A = \frac{\pi L}{2 r_0} (-1 + k^2 r_0^2) u_k^2 + \mathcal{O}(u_k^4). \quad (5.8)$$

It is shown that as $R_1/R_2 \rightarrow \infty$ Eq.(5.6) becomes Eq.(5.8) by inserting $L = 2\pi R$.

In the shrinking process, R_1 decreases from R_1 to R'_1 by ΔR_2 , while R_{20} increases from R_{20} to R'_{20} . Due to volume conservation,

$$R'_{20} = R_{20} \sqrt{\frac{R_1}{R_1 - \Delta R_2}} > R_{20}. \quad (5.9)$$

The reduction of free energy can be calculated as

$$\Delta F = \sigma \Delta A = 4\pi^2 \sigma (R'_1 R'_{20} - R_1 R_{20}) = 4\pi^2 \sigma R_1 R_{20} \left(\frac{R_{20}}{R'_{20}} - 1 \right) < 0, \quad (5.10)$$

since $R_{20}/R'_{20} < 1$. Therefore, the toroidal liquid droplet with circular cross section always tends to shrink to reduce the free energy.

5.2.2 Limitation of the free energy argument

The static analysis of the toroidal liquid droplet indicates the existence of the Rayleigh modes and the shrinking mode. However, the free energy argument is inadequate of giving the fastest growing Rayleigh mode, the shrinking speed and so on, since there is no time scale in the free energy. For example, by letting $\Delta F(k) > 0$ in Eq.(5.1), we get all the unstable modes that satisfy

$$k R_{20} < \left(\frac{R_1^2 - 1}{R_1^2} \right)^{1/4}. \quad (5.11)$$

The R.H.S. is approaching one as R_1/R_{20} approaches infinity, which is the cylinder case. Eq.(5.11) indicates that all long wavelength perturbations are unstable. In order to identify the most unstable Rayleigh mode, we will have to employ the Navier-Stokes equation to analyze the hydrodynamics involving in these instabilities.

5.3 Rayleigh instability of thin toroidal droplets

5.3.1 A new scheme in the Stokes flow regime

The most unstable mode for a cylindrical liquid thread immersed in another viscous liquid has been studied [202]. In Ref. [202] the velocity fields of the inside and outside fluids are obtained by solving the Navier-Stokes equation. By matching the boundary condition on the interfacial surface, the dispersion relation is obtained and the most unstable mode is found. However, more detailed information about the dynamics of the system is not available in Tomotika's theory, such as the flow pattern in two fluids, the structure of vorticity field, and the information of how different processes (undulation of interface and shear dissipations in two fluids) compete to give rise to the fastest growing mode. The lack of these pieces of information prevents us from further understanding how the system reacts to perturbation via. surface tension-driven flow.

Therefore, we turn to another scheme which is based on energy conservation. The principle of energy conservation must be obeyed in the process of perturbation. From the unstable mode the system gains surface energy which is converted into kinetic energy and heat due to shear dissipation. In the regime of $\rho \rightarrow 0$ (its meaning will be elaborated immediately), the kinetic energy can be ignored since it scales as $\sim \rho v^2$. It will be seen that the rate of change of the surface energy is proportional to $u_k \dot{u}_k$, while the shear dissipation is proportional to u_k^2 , in which u_k stands for the amplitude of the perturbation with wavenumber k . By equating the rate of change of the surface energy and the shear dissipation rate, one can get the growth rate

of the amplitude of the perturbation \dot{u}_k/u_k , by which the most unstable mode can be obtained [211]. The principle of energy conservation will guide the system to evolve along the trajectory with maximum gain rate of surface energy and minimum dissipation rate for maximizing the growth rate.

The surface energy can be obtained from the form of the perturbed interface. For example, they are Eq.(5.6,5.8) for toroidal and cylindrical interfaces respectively. On the other hand, the shear dissipation rate is [81]

$$\dot{E}_{visc} = - \int dV \sigma'_{ij} \nabla^i v^j, \quad (5.12)$$

which is an integral about the gradient of velocity field. σ'_{ij} is the viscous stress. The velocity field must be calculated to compute the shear dissipation rate.

We solve the Navier-Stokes equation for the velocity field in bulk fluids driven by perturbation of the interface. The Navier-Stokes equation is

$$\rho(\partial_t \vec{v} + \vec{v} \cdot \nabla \vec{v}) = -\nabla p + \eta \Delta \vec{v}. \quad (5.13)$$

In the regime of small Reynolds number where we have interest, the convective term $\vec{v} \cdot \nabla \vec{v}$ can be ignored, and the Navier-Stokes equation becomes linear:

$$\rho \partial_t \vec{v} = -\nabla p + \eta \Delta \vec{v}. \quad (5.14)$$

The requirement of $\rho \rightarrow 0$ such that the kinetic energy can be ignored is equivalent to large Ohnesorge number $Oh^{-2} \equiv \frac{\rho L \sigma}{\eta^2} \ll 1$. Note that the value of Oh^{-2} in the experiment performed by E.Pairam and A.Fernández-Nieves [200] is very small, around 5×10^{-4} (for silicone oil). It can be shown that

$$\frac{\dot{E}_{kin}}{\dot{E}_{visc}} \propto \frac{\rho L \sigma}{\eta^2}. \quad (5.15)$$

The rate of change of the kinetic energy scales as $\dot{E}_{kin} \sim \rho V^2 L^3 / t_p$, where $t_p \sim \eta L / \sigma$ is the time scale for the system to be obviously disturbed originating from the competition of the surface tension σ and the viscosity η . On the other hand, the dissipation rate scales as $\dot{E}_{visc} \sim \eta (V/L)^2 L^3 = \eta V^2 L$ by referring to Eq.(5.12). Now

it becomes clear that the more precise statement of $\rho \rightarrow 0$ is that $Oh^{-2} \equiv \frac{\rho L \sigma}{\eta^2} \ll 1$. In the regime of large Ohnesorge number, it can be further shown that the inertial term in Navier-Stokes equation can also be ignored. By checking the ratio of the inertial term to the viscous term, we have

$$\frac{\rho \partial_t v}{\eta \Delta v} \propto \frac{\rho L \sigma}{\eta^2} \ll 1 \quad (5.16)$$

by inserting t_p . Furthermore, we also have

$$\frac{\rho \vec{v} \cdot \nabla \vec{v}}{\eta \Delta v} \propto \frac{\rho L \sigma}{\eta^2} \ll 1 \quad (5.17)$$

by inserting t_p . Therefore, in the regime of large Ohnesorge number, what is really small is the density instead of the velocity.

Before trying to solve the Navier-Stokes equation for velocity field, we may first do a scaling analysis of the time scales of processes in the system. The time scale for the interface being significantly disturbed has been introduced above as t_p . Vortices will emerge near the perturbed interface [211]. And the time scale for a vortex to diffuse a distance L , is denoted as t_{diff} . The diffusion equation for the motion of vorticity can be derived by taking curl on both sides of Eq.(5.14):

$$\partial_t \vec{\Omega} = \frac{\eta}{\rho} \Delta \vec{\Omega}, \quad (5.18)$$

from which we have $t_{diff} \sim \rho L^2 / \eta$. The vorticity field $\vec{\Omega} = \nabla \times \vec{v}$. The ratio of the diffusion time scale t_{diff} to the perturbation time scale t_p is

$$\frac{t_{diff}}{t_p} \propto \frac{\rho L \sigma}{\eta^2} \ll 1. \quad (5.19)$$

Since vortices moves together with flow [212], the above relation shows that the velocity field in bulk fluid responds to the interface dynamics almost instantaneously. In this sense, we can ignore the inertial term in Navier–Stokes equation. We may also compare the times scales in inviscid and viscous fluids. In the regime of small viscosity such that the dissipation of kinetic energy is much slower than its propagation, the viscous term in Navier-Stokes equation drops out of the problem but the convective

term is retained. One relevant time scale emerges in this regime $t_{conv} \sim \sqrt{\frac{\rho L^3}{\sigma}}$. Its physical meaning is the time scale for the interface to be substantially deformed in an inviscid liquid. We may compare the perturbation time in inviscid liquid t_{conv} to that in viscous liquid t_p :

$$\frac{t_{conv}}{t_p} \sim \sqrt{\frac{\rho L \sigma}{\eta^2}} \ll 1. \quad (5.20)$$

It indicates that the relevant time scale in viscous fluid is longer than that in inviscid liquid. The dynamic process slows down due to viscosity.

Let us go back to the Navier-Stokes equation, by removing the inertial term in the regime of large Ohnesorge number, we obtain the Stokes equation

$$\nabla p = \eta \Delta \vec{v}, \quad (5.21)$$

which describes Stoke flow. The Stokes equation is symmetric under time reversion. The dynamics of the system is brought by the temporally varying boundary. If we time-reverse the boundary condition, the velocity field induced in the bulk is also time-reversed. By taking curl on both sides of Eq.(5.21), we have

$$\Delta(\nabla \times \vec{v}) = 0, \quad (5.22)$$

in which we have switched Δ and curl since they commute. For incompressible fluid, we have

$$\nabla \cdot \vec{v} = -\partial_t \rho = 0, \quad (5.23)$$

from which we can introduce a vector potential $\vec{\psi}$, such that $\vec{v} = \nabla \times \vec{\psi}$. We can fix $\vec{\psi}$ by imposing the transverse gauge $\nabla \cdot \vec{\psi} = 0$. By replacing \vec{v} for $\nabla \times \vec{\psi}$ in Eq.(5.22), we have

$$\Delta[\nabla \times (\nabla \times \vec{\psi})] = -\Delta^2 \vec{\psi} = 0. \quad (5.24)$$

The calculation of the velocity field is thus reduced to solving the bi-harmonic equation of vector potential $\vec{\psi}$.

According to the vorticity field

$$\vec{\Omega} = \nabla \times \vec{v} = \nabla \times (\nabla \times \vec{\psi}) = -\Delta \vec{\psi}, \quad (5.25)$$

the solutions to the bi-harmonic equation Eq.(6.33) can be classified into irrotational ($\Delta \vec{\psi} = 0$) and rotational ($\Delta^2 \vec{\psi} = 0$, but $\Delta \vec{\psi} \neq 0$) types. For irrotational solution,

$$\nabla p = \eta \Delta (\Delta \times \vec{\psi}) = \eta \Delta \times (\Delta \vec{\psi}) = 0, \quad (5.26)$$

and the viscous force on unit volume of fluid $\eta \Delta \vec{v} = 0$ for the irrotational solution.

As has been shown that in the regime of Stoke flow (i.e., in the large Ohnesorge number regime), the dynamics of the interface completely determines both the rate of change of surface energy and the velocity field in the bulk liquid, from which the shear dissipation can be computed by Eq.(5.12). By equating the rate of change of surface energy to the shear dissipation rate, we can obtain the dispersion relation, from which the most unstable mode can be deduced. Such a formalism applies for interfaces of general geometries. Consider an arbitrary interface separating two bulk fluids which is characterized by $\vec{R}(t)$. Given $\vec{R}(\vec{x}, t)$ and its time derivative $\dot{\vec{R}}(\vec{x}, t)$ (\vec{x} is the coordinates of points on the interface), the velocity field is obtained by solving the Stokes equation. Since the Stokes equation is linear, the dissipation rate can be written as

$$\dot{E}_{visc}[\vec{R}, \dot{\vec{R}}] = -\frac{1}{2} \int_{\vec{x}, \vec{y}} \dot{\vec{R}}(\vec{x}, t) \cdot K(\vec{x}, \vec{y}; \vec{R}) \cdot \dot{\vec{R}}(\vec{y}, t), \quad (5.27)$$

in which K is a second order tensor. The surface energy is

$$E_{\sigma}[\vec{R}] = \sigma \int_{\vec{x}} dA[\vec{R}, \vec{x}]. \quad (5.28)$$

The Laplace force acted on the boundary surface is

$$F_L = -\frac{\delta E_{\sigma}[\vec{R}]}{\delta \vec{R}}. \quad (5.29)$$

And the viscous force is

$$F_V = -\frac{\delta E_{visc}[\vec{R}, \dot{\vec{R}}]}{\delta \vec{R}} = -\frac{\delta \dot{E}_{visc}[\vec{R}, \dot{\vec{R}}]}{\delta \dot{\vec{R}}} = \int_{\vec{y}} K(\vec{x}, \vec{y}; \vec{R}) \cdot \dot{\vec{R}}(\vec{y}, t). \quad (5.30)$$

Their balance leads to

$$\frac{\delta E_\sigma[\vec{R}]}{\delta \vec{R}} = \int_{\vec{y}} K(\vec{x}, \vec{y}; \vec{R}) \cdot \dot{\vec{R}}(\vec{y}, t), \quad (5.31)$$

from which we can get the dispersion relation. Note that the equation is of first order in time. Since this equation is derived from the principle of force balance, it applies to arbitrary geometry, including those being strongly perturbed. For example, it can be applied to do analysis on the pinch-off process of a liquid column. Note that in the above analysis of force balance the acceleration term is ignored, because on one hand the boundary surface, as a geometry surface, has no thickness and on the other hand we concern the regime $\rho \rightarrow 0$.

There is another representation of the dissipation rate Eq.(5.12), which is related to the velocity field. It should be equal to Eq.(5.27), i.e.,

$$- \dot{E}_{visc} = \int dV \sigma'_{ij} \nabla^i v^j = \frac{1}{2} \int_{\vec{x}, \vec{y}} \dot{\vec{R}}(\vec{x}, t) \cdot K(\vec{x}, \vec{y}; \vec{R}) \cdot \dot{\vec{R}}(\vec{y}, t). \quad (5.32)$$

So the kernel K is also determined by the velocity field. In fact, since the velocity field for Stokes flow is determined by the dynamics of boundary surface, K is essential dependent on $\vec{R}(\vec{x}, t)$.

In the linear regime where the deformation of the interface is small, the surface area $A[\vec{R}]$ can be approximated as quadratic:

$$A[\vec{R}] = \int_{\vec{x}} \sqrt{1 + (\nabla \vec{R}(\vec{x}, t))^2} \approx A_0 + \frac{1}{2} \int_{\vec{x}} (\nabla \vec{R}(\vec{x}, t))^2. \quad (5.33)$$

By putting Eq.(5.33) into Eq.(5.31) and, to the leading order approximation, setting \vec{R} in the kernel K to the unperturbed shape \vec{R}_0 , we obtain a linear integro-differential equation for the evolution of the interface:

$$- \sigma \Delta \vec{R}(\vec{x}, t) = \int_{\vec{y}} K(\vec{x}, \vec{y}; \vec{R}_0) \cdot \dot{\vec{R}}(\vec{y}, t) \quad (5.34)$$

5.3.2 Velocity and vorticity fields

In this section, we will solve the Navier-Stokes equation for a very thin toroidal liquid droplet system. In the limit of large aspect ratio $R_1/R_2 \rightarrow \infty$, a torus can be treated

as a cylinder locally. The interfacial surface of the two fluids is disturbed like

$$r(z, t) = r_0 + u(z, t) + o(u^2), \quad (5.35)$$

in which we only keep up to the linear term of $u(z, t)$ in our linear theory. Note that the radius of the cylinder is defined to be one. $u(k, t) = \sum_k u_k(t)e^{ikz}$. Since the perturbation depends on z in the form e^{ikz} , the velocity field and the pressure also depend on z in the same way. The problem is to find out how the growth rate $g_r = \frac{\dot{u}_k}{u_k}$ depends on the wavenumber k , i.e., the dispersion relation of the system.

We will solve the biharmonic equation Eq.(6.33) for the vector potential. Due to the symmetry of the system, the velocity field is $\vec{v} = v_i \vec{e}^i = \{v_r, v_\theta = 0, v_z\}$. The velocity field is related to the vector potential by $\vec{v} = \nabla \times \vec{\psi}$. It is explicitly written in cylindrical coordinates

$$v_r = \frac{1}{r} \partial_z \psi, \quad (5.36)$$

and

$$v_z = -\frac{1}{r} \partial_r \psi. \quad (5.37)$$

It can be checked that $\nabla \cdot \vec{v} = 0$. For the cylindrical geometry, the form of the vector potential $\vec{\psi}$ is

$$\vec{\psi} = -\frac{\psi(r)}{r} e^{ikz} \hat{e}_\theta. \quad (5.38)$$

So $\Delta \vec{\psi} = -\frac{1}{r} D \psi(r) e^{ikz} \hat{e}_\theta$. $\psi(r)$ is the stream function, \hat{e}_θ is a unit vector and $D \equiv \partial_r^2 - k^2 - \frac{1}{r} \partial_r$. With this ansatz for the vector potential, the biharmonic equation Eq.(6.33) becomes

$$DD\psi(r) = 0. \quad (5.39)$$

The corresponding vorticity field in cylindrical coordinates is

$$\vec{\Omega} = \frac{1}{r} D \psi(r) e^{ikz} \hat{e}_\theta. \quad (5.40)$$

The boundary conditions are:

$$v_r(r = r_0^+) = v_r(r = r_0^-) = \dot{u}(z, t), \quad (5.41)$$

$$v_z(r = r_0^+) = v_z(r = r_0^-), \quad (5.42)$$

$$\vec{v}(r = \infty) = 0, \quad (5.43)$$

$$v_r(r = 0) = 0, \quad (5.44)$$

$$\sigma_{rz}(r = r_0^+) = \sigma_{rz}(r = r_0^-). \quad (5.45)$$

The first boundary condition is due to the assumption that fluid particles on the interfacial surface move together with the surface. And the non-slip boundary condition in Eq.(5.42) for v_z is applied [211]. The Eq.(5.44) is due to the symmetry of system. The last boundary condition is the continuity of the tangential stress across the boundary.

By integrating over a contour on the boundary, the non-slip boundary conditions of velocities can be obtained by the integral forms of $\nabla \times \vec{v} = \vec{\Omega}$ and $\nabla \cdot \vec{v} = 0$. We may invoke an analogy of a velocity field to an electric field. For the electric field, $\nabla \times \vec{E} = -iw\vec{B}$ and $\nabla \cdot \vec{E} = 0$. The source term $-iw\vec{B}$ is the counterpart of the vorticity field $\vec{\Omega}$. One difference between the electric field and the velocity field is: velocity gradient will induce a stress field due to the viscous nature of bulk fluid, while no stress field exists in an electric medium since there is no induced charges.

In what follows, we will derive the velocity field by solving the biharmonic equation in cylindrical coordinates Eq.(5.39) under the boundary conditions Eqs.(5.41)-(5.45). Eq.(5.39) is a fourth order differential equation, so there are four independent solutions, two of them are irrotational type and the other two are rotational type. We will first find the two irrotational solutions by solving the homogeneous second order differential equation $D\psi = 0$. By writing $\psi = rf(r)$ (the time-dependence is ignored

without any misunderstanding since D is time-irrelevant), we get the differential equation for $f(r)$:

$$r^2 \partial_r^2 f + r \partial_r f - (1 + k^2 r^2) f = 0, \quad (5.46)$$

which is recognized as the Modified Bessel equation of order one. The solution is the linear superposition of the modified Bessel function of the first kind $I_1(kr)$ and that of the second kind $K_1(kr)$. So the solution to $D\psi = 0$ is $\psi = axI_1(x) + bxK_1(x)$, in which $x = kr$. We can derive the other two solutions of rotational type to Eq.(5.39) by the recurrence relations of Modified Bessel function. With $x \equiv kr$, the operator D becomes $D = k^2(\partial_x^2 - 1/x\partial_x - 1)$. If we try $\psi = x^n I_n(x)$, then

$$D\psi = k^2(\partial_x^2 - \frac{1}{x}\partial_x - 1)(x^n I_n(x)) = k^2((2n - 1)I_{n-1}(x) - \frac{2n}{x}I_n(x) - I_{n+1}(x)) \quad (5.47)$$

where we have used the following recurrence relations of Modified Bessel functions:

$$\partial_x I_n(x) = \frac{n}{x} I_n(x) + I_{n+1}(x), \quad (5.48)$$

and

$$I_n(x) = \frac{2(n+1)}{x} I_{n+1}(x) + I_{n+2}(x). \quad (5.49)$$

For $n = 1$, the RHS of Eq.(5.47) equals to zero by Eq.(5.49). For $n = 2$, the RHS of Eq.(5.47) equals to $2k^2 x I_1(x)$ by Eq.(5.49). It has been shown that $D(xI_1(x)) = 0$. So two solutions to Eq.(5.39) are found to be $\psi = \{xI_1(x), x^2 I_2(x)\}$. The first solution has been found by solving $D\psi = 0$. The second solution is one rotational solution. We can also try $\psi = x^n K_n(x)$. By using the recurrence relations of Modified Bessel functions of the second kind, we find that $D\psi = 0$ if $n = 1$ and $D\psi = -2k^2 x K_1(x)$ if $n = 2$. Since $D(xK_1(x)) = 0$, $DD\psi = 0$ if $n = 2$. So we get the other two independent solutions to Eq.(5.39): $\psi = \{xK_1(x), x^2 K_2(x)\}$. The second solution is a rotational solution. Therefore the general solution to Eq.(5.39) is the linear combination of the four independent solutions

$$\psi = axI_1(x) + bxK_1(x) + cx^2 I_2(x) + dx^2 K_2(x). \quad (5.50)$$

The first two terms ($axI_1(x)$, $bxK_1(x)$) are corresponding to the irrotational flow while the last two ($cx^2I_2(x)$, $dx^2K_2(x)$) describe the rotational component of the flow.

We construct a proper solution for inside and outside fluids by boundary conditions: ψ/r for inside fluid must be finite at $r = 0$ and ψ/r for outside fluid must vanish as $r \rightarrow \infty$. Therefore, stream functions for inside and outside fluids are:

$$\psi_{in} = axI_1(x) + cx^2I_2(x), \quad (5.51)$$

and

$$\psi_{out} = bxK_1(x) + dx^2K_2(x). \quad (5.52)$$

The velocities can be derived from the stream functions by Eqs.(5.36,5.37). The velocity field in inside fluid is:

$$v_r(r; a, c) = ik^2(aI_1(kr) + ckrI_2(kr)), \quad (5.53)$$

$$v_z(r; a, c) = -k^2(aI_0(kr) + ckrI_1(kr)). \quad (5.54)$$

And the velocity field in outside fluid is:

$$v_r(r; b, d) = ik^2(bK_1(kr) + dkrK_2(kr)), \quad (5.55)$$

$$v_z(r; b, d) = k^2(bK_0(kr) + dkrK_1(kr)). \quad (5.56)$$

The tangential stress [81]

$$\sigma_{rz}(r) = \eta(\partial_r v_z + \partial_z v_r) \quad (5.57)$$

in inside fluid is

$$\sigma_{rz}(r; a, c) = 2\eta_i k^3(-c k r I_0(kr) + (c - a)I_1(kr)), \quad (5.58)$$

and in outside fluid is

$$\sigma_{rz}(r; b, d) = -2\eta_o k^3(d k r K_0(kr) + (b + d)K_1(kr)). \quad (5.59)$$

The four indefinite coefficients a, b, c, d can be determined by the four boundary conditions, i.e., by solving the linear equation $\mathbf{A}\mathbf{x} = \mathbf{B}$, where

$$\mathbf{A} = \begin{pmatrix} I_1(kr_0) & 0 & kr_0 I_2(kr_0) & 0 \\ 0 & K_1(kr_0) & 0 & kr_0 K_2(kr_0) \\ I_0(kr_0) & K_0(kr_0) & kr_0 I_1(kr_0) & kr_0 K_1(kr_0) \\ -2\eta_i(kr_0)^3 I_1(kr_0) & 2\eta_o(kr_0)^3 K_1(kr_0) & [-(kr_0)^4 \eta_i (I_1(kr_0) + I_2(kr_0))] & [2(kr_0)^3 \eta_o (kr_0 K_0(kr_0) + K_1(kr_0))] \end{pmatrix},$$

$$\mathbf{x} = \begin{pmatrix} a & b & c & d \end{pmatrix}^{-1},$$

$$\mathbf{B} = \begin{pmatrix} \frac{\dot{u}_k}{i(kr_0)^2} & \frac{\dot{u}_k}{i(kr_0)^2} & 0 & 0 \end{pmatrix}^{-1}.$$

The four coefficients a, b, c, d are:

$$a = \frac{N_a(k)}{D(k)}, \quad (5.60)$$

$$b = \frac{N_b(k)}{D(k)}, \quad (5.61)$$

$$c = \frac{N_c(k)}{D(k)}, \quad (5.62)$$

$$d = \frac{N_d(k)}{D(k)}, \quad (5.63)$$

where

$$\begin{aligned} \frac{N_a(k)}{-ikr_0 \dot{u}_k} &= [kr_0 \left(\frac{\eta_i}{\eta_o} - 1\right) I_0(kr_0) - \left(\frac{\eta_i}{\eta_o} - 2\right) I_1(kr_0)] K_0^2(kr_0) + [kr_0 \left(2\frac{\eta_i}{\eta_o} - 1\right) I_0(kr_0) \\ &+ 2\left(1 - \frac{\eta_i}{\eta_o}\right) I_1(kr_0)] K_0(kr_0) K_1(kr_0) + kr_0 \left(\frac{\eta_i}{\eta_o} - 1\right) [-kr_0 I_0(kr_0) + I_1(kr_0)] K_1^2(kr_0), \end{aligned}$$

$$\begin{aligned} \frac{N_b(k)}{-ikr_0\dot{u}_k} &= [kr_0\left(\frac{\eta_i}{\eta_o} - 1\right)I_1^2(kr_0)(kr_0K_0(kr_0) + K_1(kr_0)) + I_0(kr_0)I_1(kr_0)[kr_0\left(\frac{\eta_i}{\eta_o} - 2\right)K_0(kr_0) \\ &\quad + 2\left(\frac{\eta_i}{\eta_o} - 1\right)K_1(kr_0)] + kr_0I_0^2(kr_0)[kr_0\left(1 - \frac{\eta_i}{\eta_o}\right)K_0(kr_0) + \left(1 - 2\frac{\eta_i}{\eta_o}\right)K_1(kr_0)], \end{aligned}$$

$$\begin{aligned} \frac{N_c(k)}{i\dot{u}_k} &= I_0(kr_0)K_1(kr_0)^2 + I_1(kr_0)[kr_0\left(\frac{\eta_i}{\eta_o} - 1\right)K_0(kr_0)^2 + \left(2\frac{\eta_i}{\eta_o} - 1\right)K_0(kr_0)K_1(kr_0) \\ &\quad + kr_0\left(1 - \frac{\eta_i}{\eta_o}\right)K_1(kr_0)^2], \end{aligned}$$

$$\begin{aligned} \frac{N_d(k)}{-ikr_0\dot{u}_k} &= \left(\frac{\eta_i}{\eta_o} - 1\right)I_0(kr_0)^2K_1(kr_0) - \left(\frac{\eta_i}{\eta_o} - 2\right)I_0(kr_0)I_1(kr_0)K_1(kr_0) + I_1^2(kr_0)\left[\frac{\eta_i}{\eta_o}K_0(kr_0) \right. \\ &\quad \left. + kr_0\left(1 - \frac{\eta_i}{\eta_o}\right)K_1(kr_0)\right], \end{aligned}$$

$$\begin{aligned} \frac{D(k)}{(kr_0)^2} &= -kr_0I_0^2(kr_0)K_1^2(kr_0) + 2I_0(kr_0)I_1(kr_0)K_1^2(kr_0) + I_1^2(kr_0)\left[\frac{\eta_i}{\eta_o}kr_0K_0^2(kr_0) + \right. \\ &\quad \left. 2\frac{\eta_i}{\eta_o}K_0(kr_0)K_1(kr_0) + kr_0\left(1 - \frac{\eta_i}{\eta_o}\right)K_1^2(kr_0)\right]. \end{aligned}$$

We see from the above expressions for velocities that only the ratio of viscosities enters into the formalism. And the dynamics is brought by the time derivative of $u_k(t)$, the perturbation amplitude, as expected for Stokes flow. In order to get a picture of how the flow looks like, we give the stream plot of the velocity field for inside and outside fluids in Fig.5.3 with $\eta_i/\eta_o = 1$. We can clearly how the surface tension-driven flow breaks the cylindrical liquid droplet. The vortices are shown in Fig.5.3(b). For comparison, we only take the irrotational part of the velocity field in outside fluid by letting $d = 0$ in Eq.(5.55,5.56). The stream plot of the irrotational velocity field in outside fluid is shown in Fig.5.3(c).

Since the cylindrical interface can be approximated as flat locally in the small wavelength limit, we expect that the large k behavior of the cylindrical interface system will be approaching that of flat interface. The evolution of perturbed flat interface separating two fluids of different viscosities is studied in Appendix A. Two features of a flat interface system are: (1) vanishing of σ_{rz} on boundary; (2) vanishing of v_z on boundary. It is expected that these two features for flat geometry will emerge

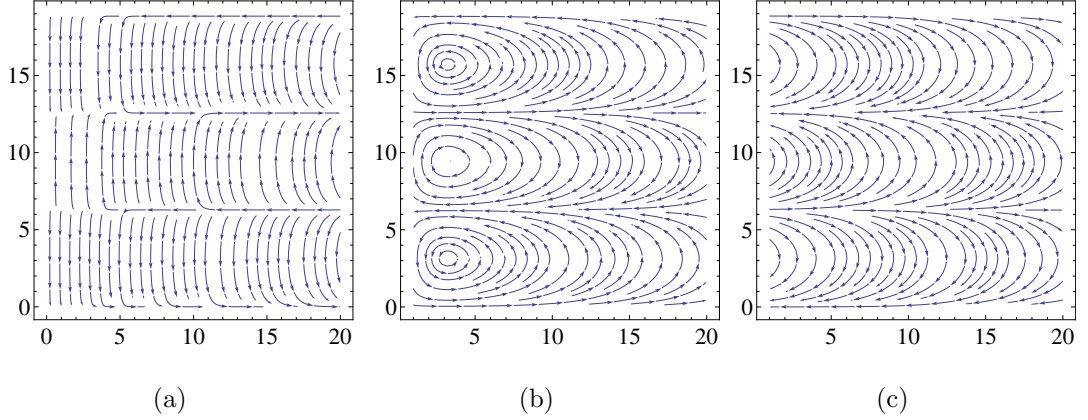


Figure 5.3: (a, b) The plot of velocity field in inside and outside fluids. (c) is the irrotational component of the velocity field in outside fluid. $\frac{\eta_i}{\eta_o} = 1, k = 1/(2r_0)$. The horizontal coordinate is r , and the vertical is z . The plot range of r for inside fluid is $r = [0, 1]$ and for outside fluid $r = [1, 20]$. $z = [0, 20]$ for both fluids.

for the cylindrical interface system with the wavenumber k approaching infinity. For simplicity, we consider the case of $\eta_i/\eta_o = 1$. The asymptotic expression for $v_z(r = r_0^-)$ as $k \rightarrow \infty$ is

$$v_z(r = r_0^-) = \frac{1}{2kr_0} + \mathcal{O}((kr_0)^{-5}). \quad (5.64)$$

And that for $\sigma_{rz}(r = r_0^-)$ at $k \rightarrow \infty$ is

$$\sigma_{rz}(r = r_0^-) = \frac{3}{2kr_0} + \mathcal{O}((kr_0)^{-3/2}). \quad (5.65)$$

It is seen that both $v_z(r = r_0^-)$ and $\sigma_{rz}(r = r_0^-)$ decays to zero in power law $\sim 1/(kr_0)$ as $kr_0 \rightarrow \infty$. Note that such asymptotic behavior holds for any values of η_i and η_o , since these viscosities only determine the numerical factors. Therefore, our solution is connected to that of flat boundary surface.

We may further examine the velocity field v_z and tangential stress σ_{rz} near the boundary on the inside fluid side as $kr_0 \rightarrow \infty$. We first expand $v_z(r)$ and $\sigma_{rz}(r)$ at $kr_0 \rightarrow \infty$, and then take the leading terms. After some calculation, it is found that

$$v_z(r; kr_0 \rightarrow \infty) \sim e^{k(r-r_0)}, \quad (5.66)$$

and

$$\sigma_{rz}(r; kr_0 \rightarrow \infty) \sim \frac{r/r_0 - 1}{\sqrt{r/r_0}} e^{k(r-r_0)} \sim (r/r_0 - 1) e^{k(r-r_0)}. \quad (5.67)$$

These asymptotic expressions for $k \rightarrow \infty$ hold near $r \lesssim r_0$. It shows that short wavelength modes decay exponentially away from the boundary. Alternatively, the longer wavelength modes can propagate further. Such asymptotic behavior of v_z and σ_{rz} are well connected to that of the flat boundary surface.

Vortices emerge near the interface when it is perturbed (see the photos of evolution of vorticity in jets in [213]). Mathematically, as an indispensable part of the general solution to the bi-harmonic Eq.(5.39), the rotational part of the stream function can guarantee the consistency of the number of boundary conditions and that of indefinite coefficients in Eqs.(5.53-5.56). We may check the flat interface case in Appendix A. It is found that irrotational flow does not exist, i.e., the boundary conditions require the indefinite coefficients in Eq.(5.117,5.118) to be zero if we remove the rotational solution.

Now we will show that the tangential stress on the boundary can be related to the vorticity field. The vectorial vorticity field $\vec{\Omega}$ is along \vec{e}_θ direction by Eq.(5.40), so

$$\Omega_\theta = (\nabla \times \vec{v})_\theta = \partial_z v_r - \partial_r v_z, \quad (5.68)$$

from which we get

$$\partial_r v_z = \partial_z v_r - \Omega_\theta. \quad (5.69)$$

By putting Eq.(5.69) into the expression for tangential stress Eq.(5.57), we have

$$\sigma_{rz} = \eta(2\partial_z v_r - \Omega_\theta) = \eta(2ikv_r - \Omega_\theta). \quad (5.70)$$

We see from Eq.(5.70) that the tangential stress is completely determined by the radial velocity field and the vorticity field. In fact, the viscous tangential stress emerges due to the relative motion of fluid particles. In Eq.(5.70), the first term (\sim

$\partial_z v_r$) describes the relative translational motion, while the second term ($\sim \Omega_\theta$) is the relative rotational motion, since vorticity is proportional to the angular velocity [212].

From Eq.(5.70) and employing the non-slip boundary condition of v_r Eq.(5.41), we have

$$\sigma_t \left(\frac{1}{\eta_o} - \frac{1}{\eta_i} \right) = \Omega_\theta(r = r_0^-) - \Omega_\theta(r = r_0^+), \quad (5.71)$$

in which σ_t is the tangential stress on boundary $\sigma_t = \sigma_{rz}(r = r_0^+) = \sigma_{rz}(r = r_0^-)$. For $\eta_i = \eta_o$, $\Omega_\theta(r = r_0^-) = \Omega_\theta(r = r_0^+)$. We will see that as $kr_0 \rightarrow \infty$, σ_t vanishes as in the flat interface case.

From Eq.(5.51,5.52), we get the vorticity field in inside and outside fluids

$$\Omega_{in} = 2(kr_0)^3 c I_1(x), \quad (5.72)$$

and

$$\Omega_{out} = -2(kr_0)^3 d K_1(x). \quad (5.73)$$

By inserting Eq.(5.62,5.63) into the above two equations, we get

$$\begin{aligned} \Delta\Omega_\theta = & \{2i \left(\frac{\eta_i}{\eta_o} - 1 \right) [-kr_0 I_0(kr_0) K_1(kr_0) + I_1(kr_0) (kr_0 K_0(kr_0) \\ & + K_1(kr_0))] \} / \{ -kr_0 I_0^2(kr_0) K_1^2(kr_0) + 2I_0(kr_0) I_1(kr_0) K_1^2(kr_0) \\ & + I_1^2(kr_0) \left(\frac{\eta_i}{\eta_o} kr_0 K_0^2(kr_0) + 2 \frac{\eta_i}{\eta_o} K_0(kr_0) K_1(kr_0) + \left(1 - \frac{\eta_i}{\eta_o} \right) kr_0 K_1^2(kr_0) \right) \}, \quad (5.74) \end{aligned}$$

in which $\Delta\Omega_\theta \equiv \Omega(r = r_0^-) - \Omega(r = r_0^+)$. By Taylor expanding Eq.(5.74), we find that $\Delta\Omega_\theta$ vanishes as $\sim 1/(kr_0)$ as $kr_0 \rightarrow \infty$. So σ_t vanishes by Eq.(5.71), which is the case of flat interface. Also we see that $\Delta\Omega_\theta = 0$ for $\frac{\eta_i}{\eta_o} = 1$, which is consistent with Eq.(5.70).

Intuitively, the vorticity field is corresponding to the relative rotational motion of fluid particles, heat will be produced in a viscous fluid. In this sense, vortices seem like serving as a mechanism of dissipating energy. However, by checking the expression for viscous dissipation rate Eq.(5.12), we find that

$$\dot{E}_{visc} = - \int dV \sigma'_{ij} \nabla^i v^j = -2\eta \int dV [(\nabla_i v_j)^2 - A_{ij}^2] = -2\eta \int dV S_{ij}^2, \quad (5.75)$$

in which A_{ij} and S_{ij} are the antisymmetric and symmetric part of $\nabla_i v_j$ respectively. $A_{ij} = 1/2(\nabla_i v_j - \nabla_j v_i)$, which is recognized as the vorticity field. $S_{ij} = 1/2(\nabla_i v_j + \nabla_j v_i)$. In the derivation, we use the fact that the product of anti-symmetric and symmetric tensors of the second order is zero. Note that the velocity field is completely determined by boundary conditions, so is the vorticity. From Eq.(5.75), we see that only the symmetric part of $\nabla_i v_j$ contributes to viscous dissipation. And the vorticity, which is the anti-symmetric part of $\nabla_i v_j$, has no contribution to dissipation. It is very similar to that the free energy of elasticity is independent of the anti-symmetric part of $\nabla_i u_j$, in which u_j is the deformation field.

We will calculate the proportion of vorticity field by comparing the ratio of the rotational component of the stream function ($cx^2 I_2(x)$) to the full stream function Eq.(5.51) in the inside fluid

$$r_i \equiv \left| \frac{cx^2 I_2(x)}{ax I_1(x) + cx^2 I_2(x)} \right| \quad (5.76)$$

and in the outside fluid

$$r_o \equiv \left| \frac{dx^2 K_2(x)}{bx K_1(x) + dx^2 K_2(x)} \right|. \quad (5.77)$$

Note that r_i approaches zero as $r \rightarrow 0$ by the expansion of $I_n(x)$ in small x . r_o approaches one as $r \rightarrow \infty$, since asymptotically $K_n(x) \sim e^{-x}$ as $x \rightarrow \infty$ for $n \in \mathbb{Z}$. The plot of r_i and r_o versus r is given in Fig.5.4 for different values of $\frac{\eta_i}{\eta_o}$. It shows that in outside fluid the proportion of rotational component decreases with the increase of its viscosity. In inside fluid the rotational flow is ignorable for high $\frac{\eta_i}{\eta_o}$. It indicates that the rotational flow mainly occurs in the less viscous fluid. In fact, the conclusion that "vorticity favor less viscous fluid" is in agreement with the experimental observation of flow past a cylinder for various Reynolds numbers [212]. In that experiment, vortices appear behind the cylinder only if the Reynolds number, which is inversely proportional to the viscosity, exceeds some threshold value, i.e., if the viscosity is small enough.

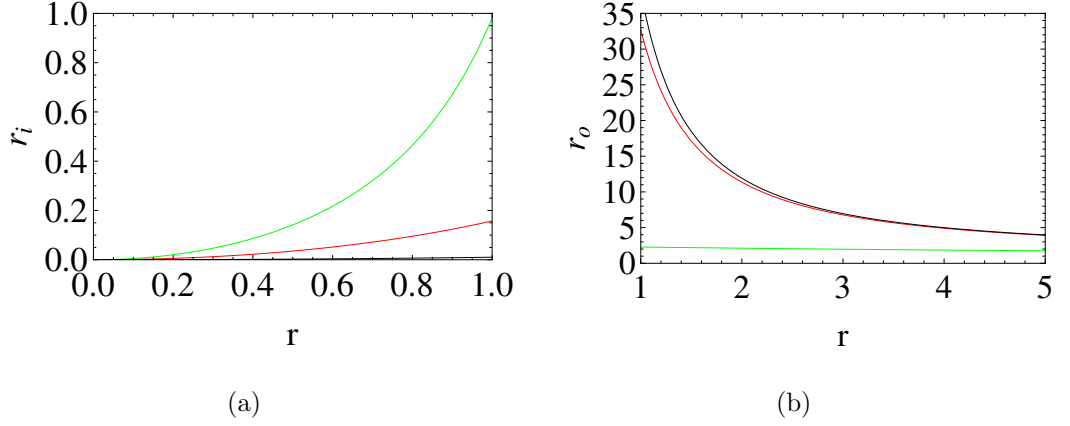


Figure 5.4: The ratio of the rotational part to the full of stream functions for inside (a) and outside (b) fluids for different viscosity ratios. $kr_0 = 1/5$. Green curve: $\frac{\eta_i}{\eta_o} = 0.001$; red curve: $\frac{\eta_i}{\eta_o} = 1$; black curve: $\frac{\eta_i}{\eta_o} = 1000$. It clearly shows that vorticity field locates in the less viscous fluid. Note that the green curve in (b) is approaching one if the plot along r is extended.

The velocity field for $\frac{\eta_i}{\eta_o} = 1$ plotted in Fig.5.3 can be understood by Fig.5.4. For $\frac{\eta_i}{\eta_o} = 1$, Fig.5.4 indicates that the vorticity field in outside fluid is much stronger than that in inside fluid. Such a picture is vividly shown in Fig.5.3: we can see obvious vortices in outside fluid. In addition, we also see from Fig.5.4 that the vorticity field decays away from the boundary. It is consistent with Fig.5.3, which shows that vortices only appear near the boundary.

5.3.3 The fastest growing mode via energy conservation

With the obtained velocity field, we can derive the shear dissipation rate by Eq.(5.12), which is duplicated as

$$\dot{E}_{visc} = - \int dV \sigma'_{ij} \nabla^i v^j, \quad (5.78)$$

σ'_{ij} is the viscous stress tensor [81] and $\nabla^i v^j$ is the contravariant derivative of the velocity field. Under the approximation of very thin torus, the dissipation rate in a toroidal interface system can be approximated by that for the cylindrical interface.

The expression for shear dissipation rate in cylindrical coordinates is (see Appendix)

$$\dot{E}_{visc} = -2\eta \int dV [(\partial_r v_r)^2 + (\partial_z v_z)^2 + \frac{1}{2}(\partial_r v_z + \partial_z v_r)^2 + (\frac{v_r}{r})^2]. \quad (5.79)$$

We can use Eq.(5.79) to calculate the dissipation rate per unit length along the z-direction. Since the z-dependence of the integrand in Eq.(5.79) is like $\cos^2(kz)$, the integration with respect to z from $z = 0$ to $z = \lambda$ is $\frac{\int_0^\lambda \cos^2(kz) dz}{\lambda} = 1/2$. $\lambda = 2\pi/k$. So the integration of z in Eq.(5.79) only provides a constant. By further integrating over r from zero to one, we finally get an analytical expression for dissipation rate in inside fluid per unit length as

$$\begin{aligned} \dot{E}_i = & -2\pi\eta_i(kr_0)^4 \{ [2c(c-a)(kr_0)^2 I_0^2(kr_0) - 2kr_0[a^2 - 3ac \\ & + c^2(3 + (kr_0)^2)] I_0(kr_0) I_1(kr_0) + [(a-2c)^2 + c(kr_0)^2(-2a+3c)] I_1^2(kr_0) \}, \end{aligned} \quad (5.80)$$

in which a, b, c, d are given in Eq.(5.60-5.63). Since these four coefficients are proportional to \dot{u}_k , \dot{E}_i is proportional to \dot{u}_k^2 . The expression for the dissipation rate in outside fluid \dot{E}_o can also be obtained, which is expressed in terms of the Meijer G functions. It is much more complicated than the expression for \dot{E}_i . So we will solve for the most unstable mode by numerical method except some limiting cases.

The rate of change of the surface energy for a toroidal interface is obtained by taking the time derivative of Eq.(5.8)

$$\dot{E}_{surf} = 2\pi^2 \frac{R_1}{R_{20}} \left(-1 + \frac{k^2 R_1 R_{20}}{\sqrt{(R_1/R_{20})^2 - 1}} \right) u_k(t) \dot{u}_k(t). \quad (5.81)$$

In comparison, the rate of change of the surface energy for a cylindrical interface per unit length is obtained by taking time derivative of Eq.(5.8)

$$\dot{E}_{surf} = \pi(-1 + (kR_{20})^2) u_k(t) \dot{u}_k(t). \quad (5.82)$$

Notice that the rate of change of the surface energy is proportional to $u_k \dot{u}_k$ and the dissipation rate is proportional to \dot{u}_k^2 . So the rate of change of the surface energy and the dissipation rate can be formally written as

$$\dot{E}_{surf} = \sigma S(k) u_k \dot{u}_k \quad (5.83)$$

and

$$\dot{E}_{vis} = -[\eta_i V_i(k) + \eta_o V_o(k)] \dot{u}_k^2. \quad (5.84)$$

By equating the rate of change of the surface energy \dot{E}_σ and the shear dissipation rate \dot{E}_{vis} , we have

$$\sigma S(k) u_k \dot{u}_k = [\eta_i V_i(k) + \eta_o V_o(k)] \dot{u}_k^2, \quad (5.85)$$

from which the growth rate of the perturbation amplitude is obtained as

$$g_r(k; \frac{\eta_i}{\eta_o}) = \frac{\dot{u}_k(t)}{u_k(t)} = \frac{\sigma S(k)}{\eta_i V_i(k) + \eta_o V_o(k)}. \quad (5.86)$$

$u_k(t)$ is the perturbation amplitude of wavenumber k . The dispersion relation for both cylindrical and toroidal interfaces can be written uniformly like Eq.(5.86). We see from Eq.(5.86) that the effect of viscosity reduces the growth rate while the surface tension accelerates the growth rate. The geometry of the interface is encoded in the $S(k)$ function. Eq.(5.86) also shows that the competition of shear dissipation and surface energy leads to the fastest growing mode. In order to maximize the growth rate of the perturbation amplitude, the system selects a mode that can reduce both the surface energy and the dissipation rate as much as possible. We also see from Eq.(5.86) that it is the ratio $\frac{\eta_i}{\eta_o}$, instead of individual η_i or η_o , that determines the most unstable mode.

In order to get a picture of how the denominator in Eq.(5.86) changes with k , we give the plot of V_i and V_o versus k with $\frac{\eta_i}{\eta_o} = 1$ in Fig.5.5. The existence of the minimum points in the curves can be traced back to the competition of the $(v_r/r)^2$ term and gradient terms (the first three terms in Eq.(5.79)). For smaller k mode, the flow can propagate further, and the further the velocity field extends, the bigger the $(v_r/r)^2$ term in Eq.(5.79) can contribute to the dissipation and the smaller the gradient term can contribute to it. Conversely, the gradient term would dominate. These two terms cannot be minimized simultaneously. Their competition leads to the minimum points in Fig.5.5.

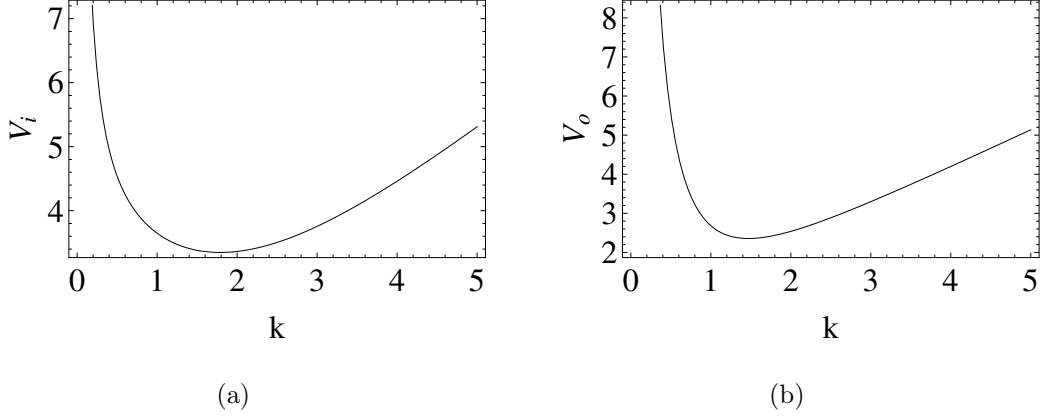


Figure 5.5: $V_i(k)$ and $V_o(k)$ versus k for inside (a) and outside (b) fluid. $\frac{\eta_i}{\eta_o} = 1$. Minimum points exist for these two functions.

In what follows, we will discuss some limiting cases. Taking $\frac{\eta_i}{\eta_o} = 1$, V_i prefers $kR_{20} \approx 1.5$ and V_o prefers $kR_{20} \approx 1.8$ for maximizing the growth rate. On the other hand, by Eq.(5.82), the surface energy term in the numerator of Eq.(5.86) always prefers $k = 0$ to guarantee the largest energy gain. Their mutual competition leads to the fastest growing mode $k_{max}R_{20} = 0.56$ (to be shown later), which is a number between.

In the limit $\frac{\eta_i}{\eta_o} \gg 1$, the dissipation in the outside fluid can be ignored, and the expressions for the coefficients a and c in Eq.(5.53,5.54) are simplified

$$a = -i\dot{u}_k \frac{kR_{20}I_0(kR_{20}) - I_1(kR_{20})}{(kR_{20})^2 I_1^2(kR_{20})}, \quad (5.87)$$

and

$$c = i\dot{u}_k \frac{1}{(kR_{20})^2 I_1(kR_{20})}. \quad (5.88)$$

By Eq.(5.80) and Eq.(5.82), we get analytical expression for the growth rate

$$\begin{aligned} g_r(k) &= \frac{\sigma}{\eta_i} \cdot \frac{\left(1 - \frac{(kR_{20})^2 R_1}{R_{20} \sqrt{(R/R_{20})^2 - 1}}\right)}{2[1 + (kR_{20})^2 - (kR_{20})^2 \left(\frac{I_0(kR_{20})}{I_1(kR_{20})}\right)^2]} \\ &= \frac{\sigma}{2\eta_i} \cdot \frac{\left(1 - \frac{(kR_{20})^2 R_1}{R_{20} \sqrt{(R/R_{20})^2 - 1}}\right)}{3 + (kR_{20})^4/48 + \mathcal{O}((kR_{20})^6)}. \end{aligned} \quad (5.89)$$

The last equality is obtained by expanding $(\frac{I_0(kR_{20})}{I_1(kR_{20})})^2$ in small kR_{20} . It clearly shows that the mode $k_{max} = 0$ has the maximum growth rate in the limit $\frac{\eta_i}{\eta_o} \gg 1$. This result is consistent with the expansion of $(\frac{I_0(kR_{20})}{I_1(kR_{20})})^2$ in terms of small kR_{20} . Note that Eq.(5.90), the expression for growth rate in the limit of $\frac{\eta_i}{\eta_o} \gg 1$, is exactly the same as in Tomotika's paper [202] (Eq.36 therein).

For $\frac{\eta_i}{\eta_o} \ll 1$, the dissipation in the inside fluid can be ignored, and the coefficients in Eq.(5.55,5.56) are simplified as

$$b = i\dot{u}_k \frac{kR_{20}K_0(kR_{20}) + K_1(kR_{20})}{(kR_{20})^2 K_1^2(kR_{20})}, \quad (5.90)$$

and

$$d = -i\dot{u}_k \frac{1}{(kR_{20})^2 K_1(kR_{20})}. \quad (5.91)$$

We obtain an analytical expression for the dissipation rate in outside fluid per unit length as

$$\dot{E}_o = -2\pi\eta_o [1 + (kR_{20})^2 - (kR_{20})^2 (\frac{K_0(kR_{20})}{K_1(kR_{20})})^2]. \quad (5.92)$$

By Eq.(5.82,5.92), we get an analytical expression for the growth rate in the limit $\frac{\eta_i}{\eta_o} \ll 1$

$$\begin{aligned} g_r(k) &= \frac{\sigma}{\eta_o} \cdot \frac{(1 - \frac{(kR_{20})^2 R}{R_{20} \sqrt{(R/R_{20})^2 - 1}})}{2[1 + (kR_{20})^2 - (kR_{20})^2 (\frac{K_0(kR_{20})}{K_1(kR_{20})})^2]} \\ &\sim \frac{(1 - \frac{(kR_{20})^2 R}{R_{20} \sqrt{(R/R_{20})^2 - 1}})}{1 + (kR_{20})^2 + o((kR_{20})^4)}. \end{aligned} \quad (5.93)$$

The last equality is obtained by expanding $(\frac{K_0(kR_{20})}{K_1(kR_{20})})^2$ in small kR_{20} . It shows that $kR_{20} = 0$ mode has the fastest growing rate. This result is also consistent with the expansion in small kR_{20} since $k_{max} = 0$. Also Eq.(5.94) is exactly the same as in Tomotika's paper [202] (Eq.37 therein).

Now we study the general case for arbitrary values of $\frac{\eta_i}{\eta_o}$. The plot of $k_{max}R_{20}$ versus $\frac{\eta_i}{\eta_o}$ is given in Fig.5.3.3. The blue curve is for the cylindrical case, while the

red curve is for the toroidal case with $R_1/R_{20} = 10$. They are almost overlapped, because a torus with aspect ratio 10 is a rather thin one. Fig.5.3.3 shows that $k_{max} = 0$ in the two limiting cases $\frac{\eta_i}{\eta_o} \gg 1$ and $\frac{\eta_i}{\eta_o} \ll 1$. For $\eta_i/\eta_o = 1/30$ as in the experiment [200], the plot of $g_r(k; \eta_i/\eta_o)$ versus kR_{20} is shown in Fig.5.7. It is found that $k_{max}R_{20} = 0.5$. This result is close to the experimental value $k_{max}R_{20} = 0.57$. For $\eta_i/\eta_o = 1/30000$, we predict $k_{max}R_{20} = 0.10$, from which we get the number of resultant spherical droplets $n = k_{max}R = 1$, which agrees with experiment. Note that this mode is distinguishable with the shrinkage mode although the number of resultant spherical droplets is the same (see Fig.4 in [200]).

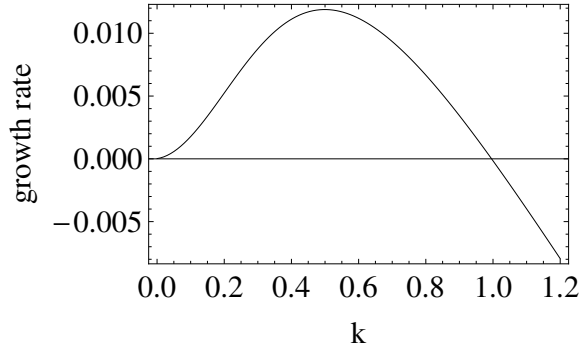


Figure 5.6: The growth rate of perturbation amplitude versus wavenumber kR_{20} . $kR_{20} = 2\pi/\lambda$. The radius of the torus is $R_1/R_{20} = 10$. $\frac{\eta_i}{\eta_o} = 1/30$ as in experiment [200]. The competition of dissipation rate and surface energy gives rise to the most unstable mode $kR_{20} = 0.5$, which is comparable to experimental value $kR_{20} = 0.57$.

5.3.4 Discussion

In deriving for the dissipation rate, we essentially treat a thin toroidal liquid droplet as a cylinder. The toroidal geometry, however, will restrict the possible modes by imposing the quantization condition $2\pi R = n\lambda$, where R is the radius of a ring. In solving for the number of beads a toroidal droplet will finally break up, the value of $n = k_{max}R$ cannot be guaranteed to be an integer unless the quantization condition

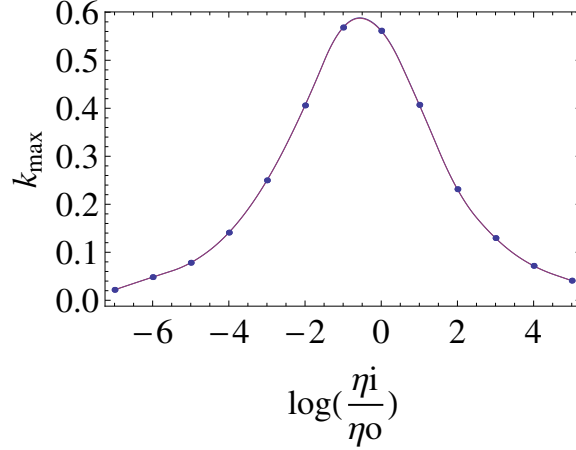


Figure 5.7: The most unstable mode versus $\log_{10}(\frac{\eta_i}{\eta_o})$. The theoretical predictions for the most unstable modes are the dots in the figure, who are fit by smooth curves for cylindrical and toroidal cases respectively. The blue curve: for cylindrical droplets. The red curve: for toroidal droplet with $R_1/R_{20} = 10$. They are almost overlapped. The curve for the case of cylindrical liquid droplet is identical to Tomotika's [202]. Note that for toroidal interface kR_{20} can only take discrete values, since the allowed wavelengths of capillary waves on torus are quantized (see Eq.(5.5)).

is satisfied. The way for a toroidal droplet to meet the quantization condition is to shrink a little bit before the Rayleigh instability occurs such that the value of n reaches an integer. This effect is observed in the experiment[200] and will be discussed in detail in the next chapter.

By comparing our result which is summarized in Fig.5.3.3 and that of Ref. [202] (see Fig.2 based on Eq.(38) therein), it is found that these two results are exactly the same. We will show the equivalence of the two approaches.

In order to obtain the velocity field, Ref. [202] and we start from different differential equations for the stream function. We start from Stokes equation without the inertial term, while Tomotika keeps the inertial term in the Navier-Stokes equation, although it is removed later. So we solve $DD\psi = 0$ and Ref. [202] solves $DD_1\psi = 0$ for stream function. $D_1 = D - \frac{in\rho}{\mu}$. Note that in [202], the stream function is named as the current function.

In fact, according to the scheme Ref. [202] adopts to solve for the most unstable mode, the inertial term cannot be removed from the beginning, or else the number of indefinite coefficients and that of boundary conditions becomes inconsistent.

In what follows, we will show that Tomotika' solutions are essentially identical to ours at the small density limit. By employing the commutation of the operators D and D_1 , Tomotika solves the fourth order differential equation $DD_1\psi = 0$ for its four independent solutions, which are

$$\{rI_1(kr), rK_1(kr), rI_1(r\sqrt{k^2 + (\frac{in\rho}{\mu})^2}), rK_1(r\sqrt{k^2 + (\frac{in\rho}{\mu})^2})\}. \quad (5.94)$$

Because

$$D \begin{pmatrix} rI_1(kr) \\ rK_1(kr) \end{pmatrix} = (\partial_r^2 - \frac{1}{r}\partial_r - k^2) \begin{pmatrix} rI_1(kr) \\ rK_1(kr) \end{pmatrix} = 0,$$

$$[\partial_r^2 - \frac{1}{r}\partial_r - (k^2 + (\frac{in\rho}{\mu})^2)] \begin{pmatrix} rI_1(r\sqrt{k^2 + (\frac{in\rho}{\mu})^2}) \\ rK_1(r\sqrt{k^2 + (\frac{in\rho}{\mu})^2}) \end{pmatrix} = 0.$$

Let $(\frac{in\rho}{\mu})^2 \equiv \alpha$. Expanding the above equation with respect to α , we have

$$[\partial_r^2 - \frac{1}{r}\partial_r - k^2 - \alpha] \begin{pmatrix} rI_1(kr) + rI_1'(kr)\frac{\alpha r}{2k} + o(\alpha^2) \\ rK_1(kr) + rK_1'(kr)\frac{\alpha r}{2k} + o(\alpha^2) \end{pmatrix} = 0.$$

By taking derivative with respect to α , and then let α to be zero, we have

$$(\partial_r^2 - \frac{1}{r}\partial_r - k^2) \begin{pmatrix} r^2 I_1'(kr) \\ r^2 K_1'(kr) \end{pmatrix} = \begin{pmatrix} 2kr I_1(kr) \\ 2kr K_1(kr) \end{pmatrix}.$$

If we act the operator D on the RHS of the above equation, it becomes zero. So under $\rho \rightarrow 0$ limit the linear superposition $\{r^2 I_1'(kr), r^2 K_1'(kr)\}$ can satisfy the differential equation $DD_1\psi = 0$. Therefore, the solution to $DD_1\psi = 0$ under the limit $\rho \rightarrow 0$ is

found to be the linear combination of $\{rI_1(kr), rK_1(kr), r^2I_1'(kr), r^2K_1'(kr)\}$. In addition, by applying the recurrence relation of the Modified Bessel function Eq.(5.48), we have

$$\begin{pmatrix} x^2 I_1'(x) \\ x^2 K_1'(x) \end{pmatrix} = \begin{pmatrix} x^2 I_2(kr) + x I_1(x) \\ x^2 K_2(kr) + x K_1(x) \end{pmatrix}.$$

Therefore, under the limit $\rho \rightarrow 0$, the solution for stream function found by Tomotika is identical to ours.

Although both Tomotika and we can predict exactly the same most unstable mode for a cylindrical system, our approach has its advantage. For example, in our representation for the stream function, we can distinguish its rotational and irrotational components. And by the expression for the growth rate via the energy conservation, we can clearly see how various processes (the change of the interfacial surface and the dissipation in bulk fluids) compete to give rise to the most unstable mode.

The most severe problem in Tomotika's paper may be the action of taking limit $\rho \rightarrow 0$ (from Eq.(33) to (34) in [202]). Problems emerge if we take such a limit on the stream function.

The stream functions for inside and outside fluid are given in Eq.(16,19) in [202]. They are copied as

$$\psi_{in} = [A_1 r I_1(kr) + A_2 r I_1(k_1' r)] e^{i(nt+kz)}, \quad (5.95)$$

and

$$\psi_{out} = [B_1 r K_1(kr) + B_2 r K_1(k_1 r)] e^{i(nt+kz)}, \quad (5.96)$$

in which $k_1^2 = k^2 + \frac{i n \rho}{\mu}$, $k_1'^2 = k^2 + \frac{i n \rho'}{\mu'}$. Note that $\mu' \equiv \eta_i$ and $\mu \equiv \eta_o$. ρ and ρ' are for outside and inside fluid respectively. If we set ρ, ρ' to be zero, then the stream functions for inside and outside fluid in Tomotika's paper becomes

$$\psi_{in} = A_1 r I_1(kr) + A_2 r I_1(k_1' r) = A r I_1(kr), \quad (5.97)$$

and

$$\psi_{out} = B_1 r K_1(kr) + B_2 r K_1(k_1 r) = Br K_1(kr), \quad (5.98)$$

in which $A = A_1 + A_2$ and $B = B_1 + B_2$. The z and t dependence of stream function is ignored. On the other hand, under the limit $\rho, \rho' \rightarrow 0$ the boundary condition for continuous velocity (the first two equations in Eq.31 in Tomotika's paper) becomes

$$AI_1(ka) - BK_1(ka) = 0, \quad (5.99)$$

and

$$AI_0(ka) + BK_0(ka) = 0. \quad (5.100)$$

The solution for these two equation is $A = 0, B = 0$. It means that if $\rho, \rho' = 0$, then the stream function vanishes. In fact, the leading term in stream function is linear in density which can be seen from Eq.(5.97,5.98) by Taylor expanding $I_1(k_1' r)$ and $K_1(k_1 r)$ in terms of the density.

Another problem is that the vorticity field is greatly suppressed in [202] in the limit $\rho, \rho' \rightarrow 0$. It is shown as follows. The vorticity fields calculated from the stream functions Eq.(5.95,5.96) are

$$\Omega_{in} = \frac{1}{r} D\psi_{in} = 2A_2 k I_1(kr) \delta k', \quad (5.101)$$

and

$$\Omega_{out} = \frac{1}{r} D\psi_{out} = 0, \quad (5.102)$$

in which $\delta k' = \frac{in\rho'}{2k\mu'}$, and it is up to the linear term of the density. If we input the experimental values, $\delta k' = \frac{in\rho'}{2k\mu'} \sim 10^{-6}$ [200]. By comparing the vorticity field in inside fluid Eq.(5.101) in [202] and that from our method denoted as Ω , we have

$$\Omega_{in}/\Omega \sim \delta k' \sim 10^{-6}. \quad (5.103)$$

Therefore, the effect of vorticity is greatly suppressed in [202].

5.4 Rayleigh instability of fat toroidal droplets

The unstable modes of the Rayleigh instability of a cylindrical liquid column can be found by free energy argument [8]. However, we cannot find the *most* unstable mode from the pure free energy argument. We will have to resort to the hydrodynamics of the bulk fluid to identify the most unstable mode by applying either the force balance condition [202] or energy conservation. In both schemes, we get both the most unstable mode and the velocity field in bulk fluids. However, for fat toroidal droplets, no analytical solution is available for the Stokes equation until now. If we only concern about identifying the most unstable mode, can we simplify the calculation without solving for the velocity field? In this section, we propose a method in terms of the Laplace pressure to identify the most unstable Rayleigh mode of fat toroidal droplets.

The Rayleigh instability can be understood in terms of the Laplace pressure. Across a liquid interface with surface tension σ , the pressure difference $\Delta P = 2\sigma H$, where the mean curvature $2H = \frac{1}{R_1} + \frac{1}{R_2}$. R_1 and R_2 are the two radii of principal curvatures. On a cylindrical liquid droplet, a perturbation u_k induces a distribution of the Laplace pressure $P = P_0 + \Delta P$, where the pressure outside is assumed to be a constant P_0 . For a perturbation of long wavelength, the mean curvature is dominated by the local radius of the cylinder. The pressure where the local radius of cylinder is minimum (valleys of the perturbation) is bigger than the pressure where the local radius is maximum (peaks of the perturbation). The pressure gradient drives the fluid to flow from the thin section to the thick section of the cylindrical droplet, amplifying the original perturbation. Similar analysis indicates that a perturbation of short wavelength can be diminished by the induced pressure gradient.

Since the pressure drives the flow, we propose a conjecture that *the variation of the Laplace pressure near a peak of the perturbation should be maximum for the most unstable mode*. We check this conjecture on a cylindrical liquid column. In the linear

regime, we pick up a mode k from the perturbation

$$R_2(z) = a + u_k \cos(kz). \quad (5.104)$$

The mean curvature can be derived as

$$H = \frac{1}{2a} - \frac{(1-x^2) \cos(kz)}{2a^2} u_k + \mathcal{O}(u_k^2), \quad (5.105)$$

where $x = ka$. The difference of the Laplace pressure at the peak $z = 0$ and a point nearby at $z = \delta z$ is

$$\delta p = \sigma u_k \frac{(1-x^2) k^2 \delta z^2}{2a^2} + \mathcal{O}(u_k^2) \propto x^2(1-x^2). \quad (5.106)$$

For an unstable mode, δp must be positive to drive the flow towards the peak thinning the neck. It is equivalent to $|x| < 1$, a same result from the free energy argument. The plot of δp vs ka is in Fig.5.8. We suggest that the most unstable mode is the one with the maximum pressure variation near the peak δp . It can be easily identified from Eq.(5.106) as

$$x_c = \sqrt{2}/2 \approx 0.71. \quad (5.107)$$

It is close to the result by Rayleigh $x = 0.69$ by solving the NS equation[201]. Thus we identify the most unstable mode by only taking into consideration the shape of interfaces. The simplicity of our method should come from the neglect of solving for the velocity field.

We will use this method to find the most unstable Rayleigh mode of fat toroidal liquid droplet. The form of perturbation is assumed to be

$$R_2(\theta) = a + u_k \cos(n\theta), \quad (5.108)$$

where n is the number of beads the toroidal liquid droplet will finally break up. After some calculation, we get the expression for the difference of the Laplace pressure near the peak of a perturbed solid torus as

$$\delta p = p(\theta = \delta\theta) - p(\theta = 0) \propto n^2(1 - n^2 + \phi^2 + 2\phi \cos \alpha + \cos(2\alpha)), \quad (5.109)$$

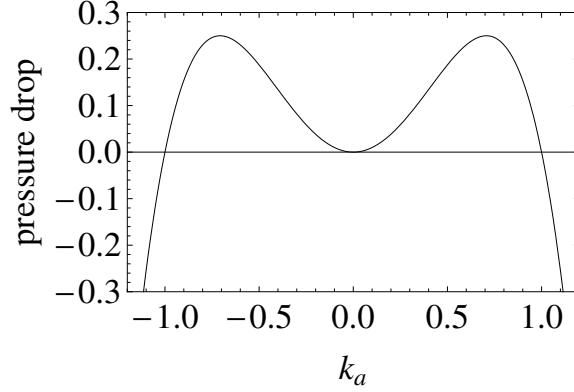


Figure 5.8: The Laplace pressure drop versus ka . The most unstable mode occurs at the peaks. The region of $|x| > 1$ is stable.

where $\phi = R_1/a$ is the aspect ratio of the torus. Considering that a Rayleigh instability mode must be accommodated by the inner circle of a torus with radius $2\pi(R_1 - R_2)$, we specify $\alpha = \pi$ in Eq.(5.109). By taking derivative of Eq.(5.109) with respect to n , we have the most unstable mode

$$n_c = \sqrt{\frac{(\phi - 1)^2 + 1}{2}}. \quad (5.110)$$

As $\phi \rightarrow \infty$, $n_c \rightarrow \phi/\sqrt{2}$, which is the cylindrical case. $(n_c)_{min} = 1$ when $\phi = 2$. Note that n_c must be an integer due to the periodic condition of toroidal geometry. ϕ will be adjusted to produce an integer n_c by the shrinking mode that is always there for both fat and thin torus. The shrinking mode will be discussed in the next chapter. Note that by inserting the instability condition $\delta p > 0$ into Eq.(5.109), we have

$$\phi > \sqrt{n^2 - 1} + 1 \geq 1, \quad (5.111)$$

since $n \geq 1$ for Rayleigh instability. It is compatible with the geometric constraint $\phi \geq 1$.

Appendix 5.A Velocity field in flat interface system

We will solve the biharmonic equation of stream function Eq.(6.41) for the velocity field in the flat interface system.

Consider two liquids separated by a flat interface at $z = 0$. The slightly perturbed interface is characterized by $u(x, t) = \sum_k u_k(t)e^{ikx}$. The motion of the interface induces flow in the bulk fluids. Due to the symmetry of the system, the y component of the velocity field vanishes, and the velocity field is independent of y . The ansatz for the vector potential is

$$\vec{\psi} = \phi(z)e^{ikx}\hat{y}. \quad (5.112)$$

$\phi(z)$ is the stream function. Obviously, $\nabla \cdot \vec{\psi} = 0$. By substituting Eq.(5.112) into the biharmonic equation of stream function Eq.(6.41), we have

$$D_f^2\phi(z) = 0, \quad (5.113)$$

in which $D_f = \partial_z^2 - k^2$. The four linearly independent solutions to the fourth order differential equation Eq.(5.113) can be easily found.

In the upper half fluid $z > 0$, only two of them are relevant due to boundary conditions at infinity:

$$\phi_1(z) = k^{-1}e^{-kz}, \quad \phi_2(z) = ze^{-kz}. \quad (5.114)$$

$\phi_1(z)$ is corresponding to the irrotational type of solution, while $\phi_2(z)$ is the rotational type.

The velocity field in the bulk fluid can be obtained by solving $\vec{v} = \nabla \times \vec{\psi}$. In the upper half fluid, the irrotational component of the velocity field is

$$v_{1x} = e^{-kz+ikx}, \quad v_{1z} = ie^{-kz+ikx}, \quad (5.115)$$

and the rotational component is

$$v_{2x} = (-1 + kz)e^{-kz+ikx}, \quad v_{2z} = ikze^{-kz+ikx}. \quad (5.116)$$

So the complete velocity field in the upper half fluid is the linear combination of these two components:

$$\vec{v} = C_1 \vec{v}_1 + C_2 \vec{v}_2. \quad (5.117)$$

Similarly, we can derive the velocity field in the lower half fluid as

$$\vec{v}' = C'_1 \vec{v}'_1 + C'_2 \vec{v}'_2, \quad (5.118)$$

in which \vec{v}' is given by

$$v'_{1x} = -e^{kz+ikx}, \quad v'_{1z} = ie^{kz+ikx}, \quad (5.119)$$

$$v'_{2x} = -(1+kz)e^{kz+ikx}, \quad v'_{2z} = ikze^{kz+ikx}. \quad (5.120)$$

We can fix the four indefinite coefficients C_1, C_2, C'_1 and C'_2 by imposing the following boundary conditions:

$$v_z(x, 0, t) = v'_z(x, 0, t), \quad v_x(x, 0, t) = v'_x(x, 0, t), \quad (5.121)$$

and

$$\eta(\partial_x v_z + \partial_z v_x)|_{z=0} = \eta'(\partial_x v'_z + \partial_z v'_x)|_{z=0}. \quad (5.122)$$

The first two boundary conditions represent the continuity of velocities, and the last boundary condition is the continuity of tangential stress across the boundary. Note that in Cartesian coordinates, the stress tensor is given by $\sigma_{ij} = -p\delta_{ij} + \eta(\partial_i v_j + \partial_j v_i)$. By matching the velocity field Eq.(5.117,5.118) to these boundary conditions, we have

$$C_1 = C_2 = C'_1 = -C'_2. \quad (5.123)$$

It is found that the boundary conditions impose so strong constraint on the velocity field that the tangential velocity vanishes on the interface. In addition, the tangential stress also vanishes on the interface. On the basis of adiabatic continuity, it is expected that these two features of flat interface also applies to the case of curved interface when considering the short wavelength behavior.

Appendix 5.B Derivation of the dissipation rate in cylindrical coordinates

The general expression for shear dissipation rate is [81]

$$\dot{E}_{visc} = - \int dV \sigma'_{ij} \nabla^i v^j, \quad (5.124)$$

which is an integral about the gradient of velocity field. σ'_{ij} is the viscous stress. We will derive the expression for shear dissipation rate in cylindrical coordinates.

We work in the non-unit basis, i.e., $\{\vec{e}_r, \vec{e}_\theta, \vec{e}_z\}$. $\vec{e}_i \equiv \frac{\partial \vec{x}}{\partial u^i}$. Ref. [81] gives expressions for the viscous stress tensor in cylindrical coordinates under the unit basis, i.e., $\{\hat{e}_r, \hat{e}_\theta, \hat{e}_z\}$. The expressions for viscous stress in [81] can be converted into the ones in the non-unit basis. They are

$$\sigma'_{\theta\theta} = 2\eta(\partial_\theta v_\theta + r v_r), \quad (5.125)$$

$$\sigma'_{rz} = \eta(\partial_r v_z + \partial_z v_r), \quad (5.126)$$

$$\sigma'_{rr} = 2\eta \partial_r v_r, \quad (5.127)$$

$$\sigma'_{zz} = 2\eta \partial_z v_z. \quad (5.128)$$

In the system concerned, $v_\theta = 0$ and the velocity field is independent of θ , so both $\sigma'_{z\theta}$ and $\sigma'_{r\theta}$ vanish. The components σ'_{rr} , σ'_{rz} and σ'_{zz} in the non-unit basis are the same as in [81], because $g_{rr} = g_{zz} = 1$ and $g_{\theta\theta} = r^2$.

$\nabla^i v^j$ can also be expressed in cylindrical coordinates. In general,

$$\nabla^i v^j = g^{li} g^{mj} \nabla_l v_m = g^{li} g^{mj} (\partial_l v_m - \Gamma_{lm}^k v_k). \quad (5.129)$$

The components of \vec{v} are defined by $\vec{v} = v_i \vec{e}^i = v^i \vec{e}_i$. Note that the components of \vec{v} here are different from those in [81], which are expressed in the unit basis. The

Christoffel symbol is $\Gamma_{ij}^m = \frac{1}{2}g^{km}[(\partial_j g_{ik}) + (\partial_i g_{jk}) - (\partial_k g_{ij})]$. The non-zero components of the Christoffel symbol are

$$\Gamma_{\theta z}^r = -r, \quad (5.130)$$

$$\Gamma_{r\theta}^\theta = \Gamma_{\theta r}^\theta = 1/r. \quad (5.131)$$

Finally we obtain the expression for the shear dissipate rate in cylindrical coordinates:

$$\begin{aligned} \dot{E}_{visc} = - \int dV \sigma'_{ij} \nabla^i v^j = -2\eta \int dV [(\partial_r v_r)^2 + (\partial_z v_z)^2 \\ + \frac{1}{2}(\partial_r v_z + \partial_z v_r)^2 + (\frac{v_r}{r})^2]. \end{aligned} \quad (5.132)$$

Chapter 6

The instabilities of toroidal droplets. II: Shrinking instability

In addition to the Rayleigh instabilities akin to those of a thin toroidal droplet there is a shrinking instability that is unique to the topology of the torus and dominates in the limit that the aspect ratio is near one (fat tori)[200]. Unlike the Rayleigh instability which is due to *external* perturbations, the shrinking mode of toroidal liquid droplet is a pure geometric, and thus an *intrinsic* effect. It can be seen by checking the variation of the free energy in the shrinking process:

$$\frac{dF}{dR_1} = 2\pi^2\sigma R_2 > 0, \quad (6.1)$$

where R_1 and R_2 are the two radii of a torus as in Fig.5.1. Eq.(6.1) shows that toroidal liquid droplets shrink to reduce the free energy and the shrinking mode exists for toroidal liquid droplet of arbitrary aspect ratio. It explains the shrinking of a thin toroidal droplet before the Rayleigh instability occurs as discussed in the previous chapter. Although this static analysis reveals the shrinking mode, the free energy alone does not provide a complete description of the system. In particular, determining the shrinking rate requires a study of droplet hydrodynamics.

In this chapter, we will study the shrinking instability in the Stokes flow regime. We first find an analytic expression for the pressure distribution inside the droplet.

We then determine the velocity field in the bulk fluid, in the Stokes flow regime, by solving the biharmonic equation for the stream function. The flow pattern in the external fluid is analyzed qualitatively by exploiting symmetries. This elucidates the detailed nature of the shrinking mode and the swelling of the cross-section following from incompressibility. Finally the shrinking rate of fat toroidal droplets is derived by energy conservation.

6.1 Pressure driving the flow

6.1.1 Laplace pressure

The distribution of Laplace pressure on the interface between the inner and outer fluids

$$p - p_0 = \sigma H, \quad (6.2)$$

where H is the mean curvature $H = \frac{R_1 + 2R_2 \cos \alpha}{R_2(R_1 + R_2 \cos \alpha)}$. For simplicity, we first consider the external pressure p_0 as constant. The Laplace pressure drop from the exterior ($\alpha = 0$) to the interior ($\alpha = \pi$) of the torus is given by $P(\alpha = 0) - P(\alpha = \pi) = 2\sigma \frac{1}{R_2} \frac{\phi}{\phi^2 - 1}$ and is a measure of the asymmetry of the torus. Since $\phi > 1$, the Laplace pressure on the exterior of the toroid is always bigger than on the interior. One also sees that the asymmetry is more pronounced for a fat torus with aspect ratio ϕ approaching one. In the limit $\phi \rightarrow \infty$, a toroid approaches a solid cylinder and the asymmetry as well as the shrinking mode disappear. The presence of the rotational symmetry about the cross section of a cylindrical liquid droplet prohibits the shrinking mode. Note that for the opposite case of constant pressure in the inner fluid, the pressure in the outer fluid will fall from the interior to the exterior of the torus. The outer fluid will therefore flow outward and the inner fluid will correspondingly flow inward, shrinking the droplet. Shrinking is thus a universal feature of one toroidal fluid inside another.

6.1.2 Pressure in bulk fluid

The typical speed in the system concerned is much smaller than that of sound, so we regard the fluid as incompressible [81], i.e.,

$$\nabla \cdot \vec{v} = -\partial_t \rho = 0. \quad (6.3)$$

Taking the divergence of the Navier-Stokes equation for an incompressible fluid shows that the pressure must be harmonic

$$\Delta p(r, \alpha) = 0. \quad (6.4)$$

The boundary condition is given by the distribution of Laplace pressure on the interface between the inner and outer fluids. The problem of solving for the pressure distribution in the bulk fluid is then reduced to solving Laplace's equation, Eq.(6.4), with the specified boundary condition. Due to the rotational symmetry, the pressure is independent of θ , the angle about z-axis. Laplace's equation for the pressure Eq.(6.4) separates in the coordinates $\{\rho, \varphi, \theta\}$ [214, 215] defined by

$$\vec{x}(\rho, \varphi, \theta) = \begin{pmatrix} \frac{a \sinh \rho \cos \theta}{\cosh \rho - \cos \varphi} \\ \frac{a \sinh \rho \sin \theta}{\cosh \rho - \cos \varphi} \\ \frac{a \sin \varphi}{\cosh \rho - \cos \varphi} \end{pmatrix},$$

where $a = r \sinh \rho$. $\{\varphi, \theta\}$ characterizes a conformally flat 2-dim surface. $\{\rho, \varphi, \theta\}$ are defined as follows: θ is the angle around the ring; φ is defined via

$$\cos \alpha = \frac{\phi(r) \cos \varphi - 1}{\phi(r) - \cos \varphi} \quad (6.5)$$

and

$$\cos \varphi = \frac{\phi(r) \cos \alpha + 1}{\phi(r) + \cos \alpha}, \quad (6.6)$$

where $\phi(r)$ is the aspect ratio R_1/r . $\varphi \in [0, 2\pi]$. ρ is defined as

$$\cosh \rho = \phi(r), \quad (6.7)$$

such that $\rho = \ln(\phi + \sqrt{\phi^2 - 1})$. In the new toroidal coordinates $\{\rho, \varphi, \theta\}$, by inserting

$$p = p_1 \sqrt{\cosh \rho - \cos \varphi} \quad (6.8)$$

into the Laplace's equation for pressure, we have the general solution [215]:

$$p = \sqrt{\cosh \rho - \cos \varphi} \sum_{p,q \in \mathbb{Z}} \{P_{p-1/2}^q(\cosh \rho), Q_{p-1/2}^q(\cosh \rho)\} \times \{\sin p\varphi, \cos p\varphi\} \times \{\sin q\theta, \cos q\theta\}. \quad (6.9)$$

The expressions in the curly bracket denotes the linear combination. $P_{p-1/2}^q(x)$ and $Q_{p-1/2}^q(x)$ are the Associated Legendre functions of the first and the second kinds respectively. The parameters p and q are integers due to the periodicity of system with respect to φ and θ . Note that another ansatz for pressure is [216]

$$p = p_2 / \sqrt{\frac{a \sinh \rho}{\cosh \rho - \cos \varphi}}. \quad (6.10)$$

This form of ansatz is convenient for situations where the boundary conditions do not involve φ . In our system, the boundary condition is φ -dependent, so we adopt the ansatz Eq.(6.8). In what follows, we will identify the particular solution to our problem from the general solution by imposing the constraints of symmetry, boundary conditions and asymptotic behaviors near the reference circle (the central circle of torus).

Due to the rotational symmetry around the torus, we can immediately set $q = 0$. The Associated Legendre functions degenerate to Legendre functions. The reflection symmetry of torus selects the $\cos p\varphi$ in the general solution. Physically it is required that the pressure near the reference circle must be finite. In order to satisfy this asymptotic condition, we will examine the asymptotic behavior of Legendre functions as $r \rightarrow 0$ or equivalently $\rho \rightarrow \infty$ by Eq.(6.7). As $x \rightarrow \infty$ only $\sqrt{x} \text{Re}[Q_{p-1/2}(x)]$ ($p \in \mathbb{Z}$) converges. It converges to $\pi/\sqrt{2}$ if $p = 0$ and zero if $p \neq 0$. And we can exclude the Legendre function of the first kind from the general solution, because it diverges as $\rho \rightarrow \infty$.

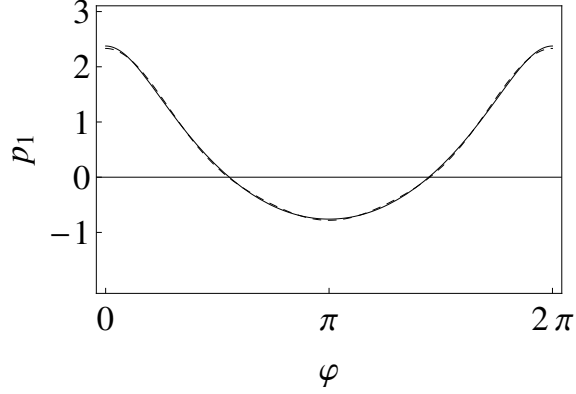


Figure 6.1: Determine the values of A_p in Eq.(6.12) by fitting the boundary condition $f(\varphi)$ in Eq.(6.13). The black solid curve is $f(\varphi)$, which is the boundary condition. The dashed curve is for p_1 defined in Eq.(6.8).

By taking into consideration of the above constraints, we finally obtain the physically acceptable solution:

$$\begin{aligned} p(\rho, \varphi) &= \sqrt{\cosh \rho - \cos \varphi} \sum_{p \in \mathbb{Z}} \alpha_p \operatorname{Re}[Q_{p-1/2}(\cosh \rho)] \cos(p\varphi) \\ &\equiv \sqrt{\cosh \rho - \cos \varphi} \left[\frac{A_0(\rho)}{2} + \sum_{p \neq 0} A_p(\rho) \cos(p\varphi) \right]. \end{aligned} \quad (6.11)$$

This form of solution satisfies the Laplace's equation, and both the rotational and reflection symmetries of system, and it guarantees that the pressure near the reference circle is finite. We proceed to determine the coefficients A_p by fitting the boundary condition Eq.(6.2). On the boundary ($r = R_2$),

$$\frac{A_0}{2} + \sum_{p \neq 0} A_p \cos(p\varphi) = f(\varphi), \quad (6.12)$$

in which $f(\varphi)$ is related to the mean curvature:

$$f(\varphi) = \frac{c_1 + c_2 \cos \varphi}{\sqrt{\phi(R_2) - \cos \varphi}}. \quad (6.13)$$

So

$$\pi A_0 = \int_0^{2\pi} f(\varphi) d\varphi. \quad (6.14)$$

$$\pi A_p = \int_0^{2\pi} f(\varphi) \cos(p\varphi) d\varphi. \quad (6.15)$$

Note that both c_1 and c_2 have contribution to A_0 (i.e., α_0) due to the denominator in Eq.(6.13).

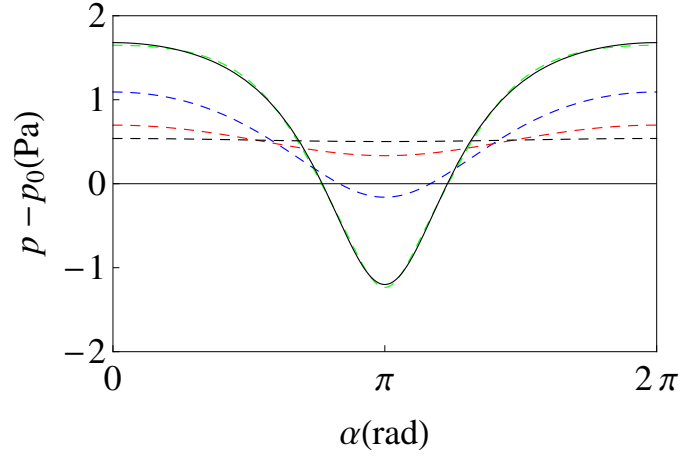


Figure 6.2: The pressure $p(r, \alpha)$ vs. angle α at different radial distances away from the reference circle for $R_1 = 5$ mm and aspect ratio $\phi = R_1/R_2 = 1.5$. The solid black curve is the pressure distribution on the boundary $p = \sigma H$. Green curve: $r = R_1/1.5$ (boundary). Blue curve: $r = R_1/3$. Red curve: $r = R_1/10$. Dashed Black curve: $r = R_1/100$. The green curve fits the exact pressure on the boundary very well.

Numerical calculation shows that cutting the value of p at $p_{max} = 3$ is sufficient to fit the boundary condition as shown in Fig.6.1). The values of parameters are: $\phi(R_2) = 1.5$, $\sigma = 4 \times 10^{-3}$ N/m, and $R_1 = 5$ mm. σ and R_1 are the experimental values [200]. The values of A_p with p from zero to 3 are: $\{0.94597, 1.4671, 0.30283, 0.089182\}$. The values of α_p can be calculated from the values of A_p :

$$\alpha_0 = \frac{A_0/2}{Re[Q_{0-1/2}(\phi(R_2) = 1.5)]}, \quad (6.16)$$

and for $p = 1, 2, 3$,

$$\alpha_p = \frac{A_p}{Re[Q_{p-1/2}(\phi(R_2) = 1.5)]}. \quad (6.17)$$

The pressure distribution is finally obtained

$$p(\rho, \varphi) = \sqrt{\cosh \rho - \cos \varphi} [\alpha_0 \operatorname{Re}[Q_{0-1/2}(\cosh \rho)] + \sum_{p=1}^3 \alpha_p \operatorname{Re}[Q_{p-1/2}(\cosh \rho)] \cos(p\varphi)], \quad (6.18)$$

where $\alpha_0 = 0.23427$, $\alpha_1 = 3.7315$, $\alpha_2 = 2.6709$, $\alpha_3 = 2.4628$. Note that we only take positive p because $\cos(p\varphi) = \cos(-p\varphi)$ and $\operatorname{Re}[Q_{p-1/2}(z)] = \operatorname{Re}[Q_{-p-1/2}(z)]$. By expressing Eq.(6.6, 6.7) and Eq.(6.19) in terms of r and α , we plot the distribution of the pressure over the cross section of a toroidal droplet in Fig.6.2. The pressure clearly drops from the exterior ($\alpha = 0, 2\pi$) to the interior ($\alpha = \pi$). This pressure gradient drives the fluid towards the center of the toroid. As r decreases the pressure distribution becomes more isotropic (α -independent). The symmetric function curve about $\alpha = \pi$ in Fig.6.2 is due to the reflection symmetry of the system.

Now we will discuss the pressure distribution near the reference circle. It has been pointed out that only the $p = 0$ mode in Eq.(6.11) does not vanish as $r \rightarrow 0$, i.e., only this mode contributes to the pressure on the reference circle. This enables us to study the behavior of the fluid near the reference circle analytically.

The pressure near the reference circle has the asymptotic form

$$p(r \rightarrow 0) = \sqrt{\cosh \rho - \cos \varphi} [\alpha_0 \operatorname{Re}[Q_{0-1/2}(\cosh \rho)]]. \quad (6.19)$$

α_0 is determined by the boundary condition. By inserting Eq.(6.19) into the Stokes equation

$$-\nabla \times \vec{\Omega} = \Delta \vec{v} = \frac{1}{\eta} \nabla p, \quad (6.20)$$

we have

$$\partial_\alpha \Omega_\theta = -\frac{\sqrt{g}}{\eta} \partial_r p(\rho, \alpha) = -\frac{\sqrt{g}}{\eta} \partial_r p(\rho, \alpha) \partial_r \rho = \frac{\alpha_0 \pi r}{2\sqrt{2}\eta} \cos \alpha, \quad (6.21)$$

and

$$\partial_r \Omega_\theta = \frac{\sqrt{g}}{\eta R^2} \partial_\alpha p(\rho, \alpha) = \frac{\alpha_0 \pi}{2\sqrt{2}\eta} \sin \alpha, \quad (6.22)$$

in which $\sqrt{g} = r(R_1 + r \cos \alpha)$. In the last equalities of the above two equations, the limit $r \rightarrow 0$ is imposed. The solution for vorticity can be found:

$$\Omega_\theta = \frac{\alpha_0 \pi r}{2\sqrt{2}\eta} \sin \alpha + c, \quad (6.23)$$

in which c is a constant. The reflection symmetry requires $c = 0$. Therefore, vorticity vanishes near the reference circle. So a potential theory is sufficient to describe the behavior of fluid in this region. Furthermore, since $r < R_2 \ll R_1$, we can work in cylindrical coordinates $\{u^1 = \alpha, u^2 = z = R_1\theta, u^3 = r\}$, after some calculation we have

$$\Omega_2 = \frac{g_{22}}{\sqrt{g}} [\partial_3 (-\frac{g_{11}}{\sqrt{g}} \partial_3 \psi_2) - \partial_1 (\frac{g_{33}}{\sqrt{g}} \partial_1 \psi_2)], \quad (6.24)$$

in which the stream function $\vec{\psi} = \psi_2 \vec{e}^2$ and the vorticity $\vec{\Omega} = \Omega_2 \vec{e}^2$. By letting $\Omega_2 = 0$ in the region of $r \sim 0$, we have

$$\partial_r \psi_2 + R \partial_r^2 \psi_2 + \frac{1}{r} \partial_\alpha^2 \psi_2 = 0. \quad (6.25)$$

Solving it by variable separation, we have the physically acceptable solution

$$\psi_2 = \sum_{k \in \mathbb{Z}^+} c_k r^k e^{ik\alpha}. \quad (6.26)$$

The velocity field (in the unit basis) near the reference circle can thus derived via. $\vec{v} = \nabla \times \vec{\psi}$ as

$$v_\alpha = - \sum_{k \in \mathbb{Z}^+} c_k k r^{k-1} e^{ik\alpha}, \quad (6.27)$$

and

$$v_r = \sum_{k \in \mathbb{Z}^+} ik c_k r^{k-1} e^{ik\alpha}. \quad (6.28)$$

By taking into the physical consideration that the velocity field near the reference circle should be finite and non-vanishing and the reflection symmetry for v_r and the mirror symmetry for v_α , we finally have

$$v_\alpha = c \sin \alpha, \quad (6.29)$$

and

$$v_r = -c \cos \alpha. \quad (6.30)$$

In the $\{x, z\}$ coordinates (see Fig.5.1), the velocity field near the reference circle is expressed as

$$v_x = v_\alpha \sin \alpha - v_r \cos \alpha = c \quad (6.31)$$

and

$$v_z = v_\alpha \cos \alpha + v_r \sin \alpha = 0. \quad (6.32)$$

Therefore, the velocity field near the reference circle is uniform towards the center of torus.

6.2 Velocity field

We now turn to the velocity distribution in a viscous toroidal liquid droplet. The complete velocity field can be obtained by solving the biharmonic vectorial equation

$$\Delta^2 \vec{\psi} = 0. \quad (6.33)$$

Due to the rotational symmetry of the torus system, only the θ -direction component of the vector potential $\vec{\psi}$ does not vanish, i.e., $\vec{\psi} = \psi_\theta \vec{e}^\theta$. Without confusion with $\vec{\psi}$, we define the stream function $\psi \equiv \psi_\theta$. The vectorial biharmonic equation Eq.(6.33) is simplified to a scalar differential equation which is expressed in the new toroidal coordinates $\{\rho, \varphi, \theta\}$ [217]

$$E^2(E^2\psi) = 0, \quad (6.34)$$

where ψ , the stream function, is the only non-zero component ψ_θ of the vector potential $\vec{\psi}$ and the second-order partial differential operator E is given by

$$E^2 = wh^2[\partial_\rho(\frac{1}{w}\partial_\rho) + \partial_\varphi(\frac{1}{w}\partial_\varphi)], \quad (6.35)$$

$$w = \frac{a \sinh(\rho)}{\cosh(\rho) - \cos(\varphi)}, \quad (6.36)$$

and

$$h = \frac{\cosh(\rho) - \cos(\varphi)}{a}. \quad (6.37)$$

The general solution to Eq.(6.34) is found by variables separation [217]

$$\psi = \frac{a \sinh \rho}{(\cosh \rho - \cos \varphi)^{3/2}} \sum_{\nu \in \mathbb{Z}} \{\cos(\nu\varphi), \sin(\nu\varphi)\} \{P_{\nu-3/2}^1(\cosh \rho), P_{\nu+1/2}^1(\cosh \rho), Q_{\nu-3/2}^1(\cosh \rho), Q_{\nu+1/2}^1(\cosh \rho)\}. \quad (6.38)$$

$P_{\nu}^{\mu}(x)$ and $Q_{\nu}^{\mu}(x)$ are the Associated Legendre functions of the first and second kind. For $\nu = 0$, the four independent solutions to the fourth order differential equation Eq.(6.34) degenerate to two, since $P_{-3/2}^1(x) = P_{1/2}^1(x)$ and $Q_{-3/2}^1(x) = Q_{1/2}^1(x)$. In addition, because

$$P_{-\nu+1/2}^1(x) = P_{\nu-3/2}^1(x), \quad (6.39)$$

and

$$Q_{\nu+1/2}^1(x) = Q_{-\nu-3/2}^1(x) \quad (6.40)$$

for $\nu \in \mathbb{Z}$, we only need to consider $Q_{\nu-3/2}^1(x)$ and $P_{\nu+1/2}^1(x)$ with $\nu \in \mathbb{Z}$.

In what follows, we construct a physically acceptable solution *inside* a toroidal liquid droplet.

First of all, by making use of the reflection symmetry of vorticity field, which is related to stream function via

$$\vec{\Omega} \equiv \nabla \times \vec{v} = \nabla \times (\nabla \times \vec{\psi}) = -\Delta \vec{\psi}, \quad (6.41)$$

we should select the $\sin \nu\varphi$ from the general solution and exclude the $\nu = 0$ mode. It is also required that approaching the reference circle ($\rho \rightarrow \infty$) $v_x \rightarrow$ a finite value and $v_z \rightarrow 0$. So we will examine the asymptotic behavior of both v_x and v_z , which can be derived from the stream function ψ by

$$v_{\rho} = -\frac{g_{\rho\rho}}{\sqrt{g}} \partial_{\varphi} \psi, \quad (6.42)$$

$$v_\varphi = \frac{g_{\varphi\varphi}}{\sqrt{g}} \partial_\rho \psi, \quad (6.43)$$

$$v_x = v_\rho g^{\rho\rho} \vec{e}_\rho \cdot \vec{e}_x + v_\varphi g^{\varphi\varphi} \vec{e}_\varphi \cdot \vec{e}_x, \quad (6.44)$$

$$v_z = v_\rho g^{\rho\rho} \vec{e}_\rho \cdot \vec{e}_z + v_\varphi g^{\varphi\varphi} \vec{e}_\varphi \cdot \vec{e}_z. \quad (6.45)$$

After some calculation, it is found that only the Associated Legendre function of the second kind in the general solution is acceptable, and $P_{\nu+1/2}^1(r)$ can be excluded since it leads to divergence of velocity field near the reference circle. Imposing the physical requirements that approaching the reference circle v_x tends to a finite value and $v_z \rightarrow 0$ (reflection symmetry) yields the complete solution

$$\psi(\rho, \varphi) = \frac{a \sinh \rho}{(\cosh \rho - \cos \varphi)^{3/2}} \sum_{\nu=-\infty}^{+\infty} c_\nu \sin(\nu\varphi) Q_{\nu-3/2}^1(\cosh \rho) \quad (6.46)$$

Note that $v_x \rightarrow -\frac{\pi c_1}{2\sqrt{2}}$ and $v_z \rightarrow 0$ as $\rho \rightarrow \infty$ ($r \rightarrow 0$). Thus only the $\nu = 1$ mode contributes to the flow near the reference circle. The coefficients c_ν in Eq.(6.46) can be determined by matching to the velocity field on the interface. Assuming that high viscosity fixes the fluid particles on the interface to move with the interface as it shrinks, the boundary conditions are found to be $v_{x0} = V(1 - \frac{x_0}{2R_1})$ and $v_{z0} = -\frac{V}{2} \frac{z_0}{R_1}$, where x_0 and z_0 denote spatial points on the boundary and $V \equiv dR_1/dt$. The point ($x = 0, z = 0$) is the center of the cross section.

We will show that the $\nu = 1$ mode is sufficient to fit this boundary condition. Since the solution for stream function Eq.(6.46) is expressed in the $\{\varphi, \rho\}$ coordinates, for comparison we also express the boundary condition in terms of v_φ and v_ρ via. the transformation relation:

$$v_\rho = v_x \vec{e}_\rho \cdot \vec{e}_x + v_z \vec{e}_\rho \cdot \vec{e}_z, \quad (6.47)$$

and

$$v_\varphi = v_x \vec{e}_\varphi \cdot \vec{e}_x + v_z \vec{e}_\varphi \cdot \vec{e}_z. \quad (6.48)$$

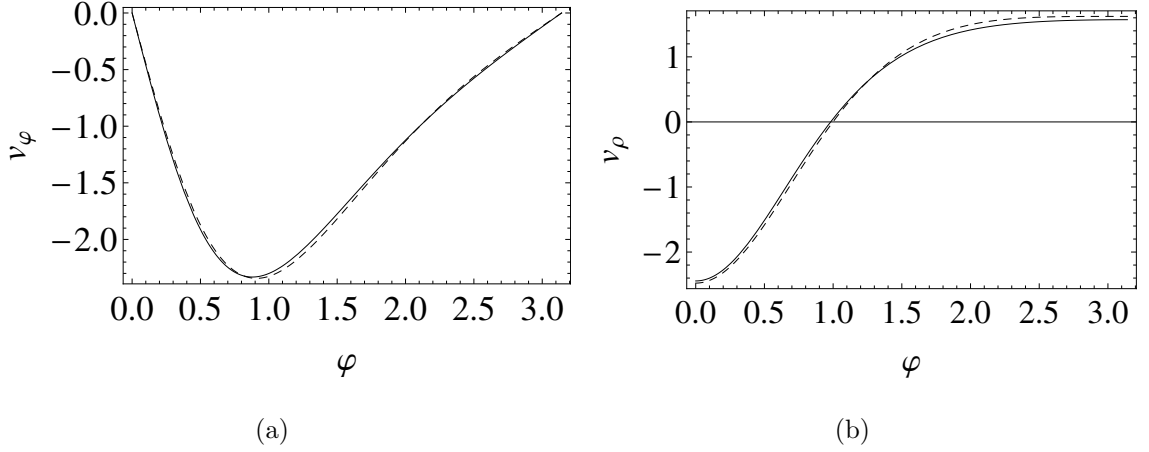


Figure 6.3: Determine the coefficient C_ν in Eq.(6.46) by fitting the boundary condition. The solid curves are the velocity field on the boundary, and the dashed curves are the velocity field derived from the stream function with $C_\nu/V = -4$. $\nu = 1$. $R_1 = 5$ mm, $R_{20} = 2$ mm.

On the other hand, the velocity field can be derived from the stream function Eq.(6.46) as

$$v_\rho = - \sum_\nu C_\nu \frac{\cosh \rho - \cos \varphi}{\sinh \rho} \left[-\frac{3 \sinh \rho \sin \varphi}{2(\cosh \rho - \cos \varphi)^{5/2}} (\sin \nu \varphi) + \frac{\sinh \rho}{(\cosh \rho - \cos \varphi)^{3/2}} (\nu \cos \nu \varphi) \right] Q_{\nu-3/2}^1(\cosh \rho), \quad (6.49)$$

and

$$v_\varphi = \sum_\nu C_\nu \frac{\cosh \rho - \cos \varphi}{\sinh \rho} \left[-\frac{-5 + 4 \cos \varphi \cosh \rho + \cosh 2\rho}{4(\cosh \rho - \cos \varphi)^{5/2}} Q_{\nu-3/2}^1(\cosh \rho) + \frac{\sinh \rho}{(\cosh \rho - \cos \varphi)^{3/2}} \partial_\rho Q_{\nu-3/2}^1(\cosh \rho) \right] \sin \nu \varphi \quad (6.50)$$

We numerically determine the indefinite coefficients C_ν in Eq.(6.46).

We plot the mode ν of v_φ and v_ρ in Eq.(6.49) on the boundary ($\rho = \rho_0 = R_1/R_2$) versus φ in Fig.6.3 (the dashed curve). By comparing them to the boundary condition (the solid curve in Fig.6.3), we can determine the value of C_ν/V as well as the mode ν . It is found that when $\nu = 1$, $C_\nu/V = -4$, the boundary condition can be well fitted. In Fig.6.3, the values of R_1 and R_2 are specified. In the shrinking process, both R_1 and R_2 change. In order to satisfy the boundary condition in the whole process,

the value of C_ν/V need to change correspondingly. It means that the velocity field inside toroidal droplet, which is specified by C_ν , is changing in the shrinking process. However, numerical experiments show that the $\nu = 1$ is always the principal one; we can always change the value of C_ν/V instead of that of ν to fit the boundary condition well. Note that the $\nu = 1$ mode is the only mode contributing to the flow near the reference circle

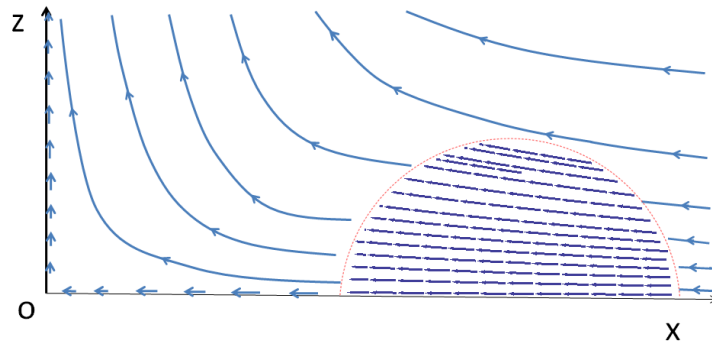


Figure 6.4: The velocity field inside and outside a cross-section of a toroidal liquid droplet. The dashed semi-circle is the interface of two distinct fluids. The velocity field inside the droplet is calculated by solving the biharmonic equation. The external flow pattern is schematically plotted by imposing boundary conditions and exploiting symmetry. The mode number $\nu = 1$, $R_1 = 5$ mm and $R_{20} = 2$ mm.

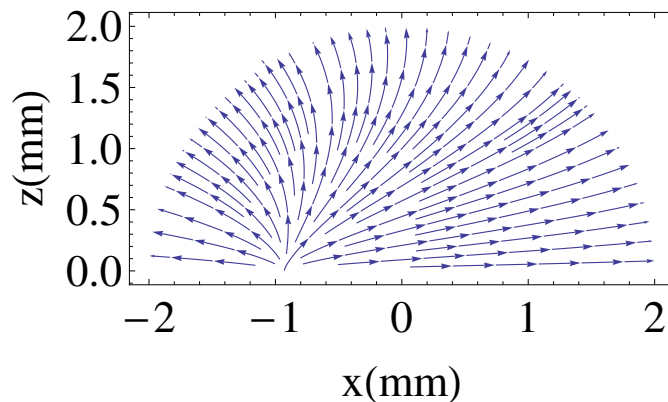


Figure 6.5: The velocity field inside the toroidal droplet of Fig.6.4 in a comoving reference frame shrinking with the droplet. The swelling of the cross section is readily inferred.

We may solve for the velocity field in the external fluid in the same way as we do

for inside toroidal droplet. However, the toroidal coordinates $\{\rho, \varphi, \theta\}$ cannot cover the whole space outside a toroid. For example, in region of $r > R_1$, we have

$$\frac{R_1}{r} = \cosh \rho < 1, \quad (6.51)$$

in which ρ is not well defined in the real domain. In addition, not all points on the circle with $r = R_1$ cannot be distinguished (except the center of torus locating at $\alpha = 0$) by the toroidal coordinates, because

$$\cos \varphi = \frac{r \cos \alpha + 1}{r + \cos \alpha} \rightarrow \frac{\cos \alpha + 1}{1 + \cos \alpha} = 1, \quad (6.52)$$

as $r \rightarrow 1$. All these points are described by a single point in the toroidal coordinates $\{\rho = 0, \varphi = 0\}$. For the center of torus, $\cos \varphi = (-r + 1)/(r - 1) = -1$, so it is described by $\{\rho = 0, \varphi = \pi\}$. Therefore, we turn to qualitative analysis of the external velocity field based on symmetry and the boundary condition. The external flow must satisfy the reflection and rotational symmetries and it should continuously connect the velocity field inside. The schematic plot of external flow is given in Fig.6.4. The velocity on x and z axis is parallel to them due to reflection symmetry about the x-y plane and the rotational symmetry about the z-axis, respectively. The velocity vanishes at the O point. From Fig.6.4 we see that the fluid in the hole of toroid is squeezed out in the shrinking process.

The velocity field inside the droplet in the laboratory frame is plotted in Fig.6.4. The shrinking of the droplet is clearly indicated by the inward directed flow inside the droplet. One also sees that outer fluid within the toroidal hole is squeezed out. Further insight is provided by plotting the velocity field (see Fig.6.5) inside the droplet in a reference frame comoving with the shrinking of the droplet. The swelling of the cross section resulting from volume conservation is clearly visible.

The vorticity field, $\vec{\Omega} \equiv \nabla \times \vec{v} = -\Delta \vec{\psi}$ is plotted in Fig.6.6 which shows its only non-zero component Ω_θ as a function of r and α respectively. Fig.6.6(a) shows that the vorticity field is only significant near the boundary – it decays rapidly as one approaches the reference circle. Fig.6.6(b) shows Ω_θ versus α for $\nu \in [-3, 3]$. The

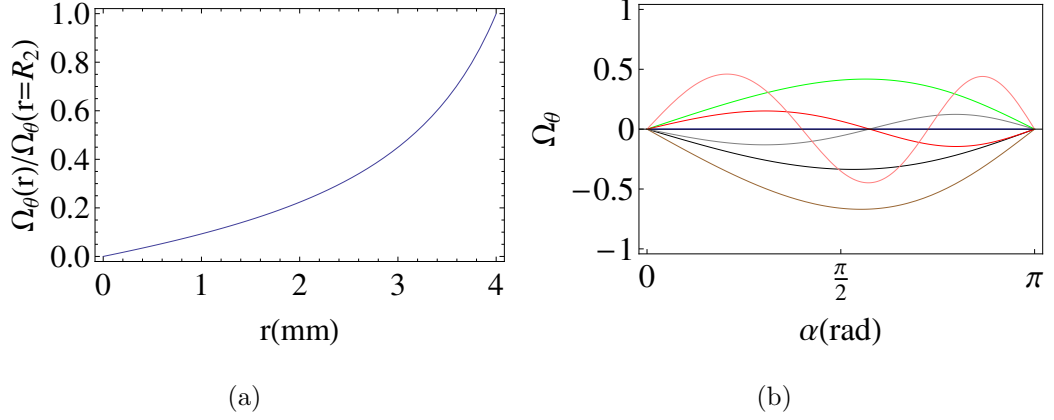


Figure 6.6: (a) The vorticity $\Omega_\theta(r)/\Omega_\theta(r = R)$ versus r . Parameters: $\nu = 1$, $c_1 = 1$, $\alpha = 1$ rad, $R_1 = 5$ mm and $R = 4$ mm . The vorticity field falls to zero at the reference circle. (b) Ω_θ versus angle α for modes ν in the range $(-3, 3)$. The vorticity Ω_θ is rescaled to show different modes in the same figure. Parameters: $\phi = 5$, $a = 1$. Blue curve: $\nu = 0$ (vorticity vanishes). Black curve: $\nu = 1$. Brown curve: $\nu = 2$. Gray curve: $\nu = 3$. Green curve: $\nu = -1$. Red curve: $\nu = -2$. Pink curve: $\nu = -3$. Note that the number of peaks or valleys is determined by the mode number ν .

vorticity field vanishes at $\alpha = 0$ and π due to its odd parity. The sign of Ω_θ reflects the chiral property of vortices. The number of peaks and valleys on the $z > 0$ plane (i.e., $\alpha \in [0, \pi]$) is

$$n = \begin{cases} -\nu, & \nu < 0 \\ \nu - 1, & \nu > 1 \\ 1, & \nu = 1, \end{cases}$$

and is therefore completely determined by the mode ν .

6.3 Shrinking speed

For the shrinkage mode, the shrinking speed is the physically interesting quantity, because on one hand it is measurable [200] and on the other hand it reflects the competition of free energy and viscous dissipation.

In the process of shrinking the free energy gained is dissipated in viscous damping. By equating the rate of change of the free energy, Eq.(6.1), to the viscous dissipation

rate we can obtain the shrinking speed. We focus here on the experimentally explored case of a low viscosity (η_i) inner fluid immersed in a viscous (η_o) outer bath [200]. In this case the dissipation occurs almost entirely in the outer fluid. Applying Stokes' equation for an incompressible fluid the dissipation rate can be separated into two parts

$$\dot{E}_{vis} = - \int dV \sigma'_{ij} \partial_i v_j = - \int df_i \sigma'_{ij} v_j + \int dV v_j \partial_i \sigma'_{ij} . \quad (6.53)$$

Here df_i is the i component of the area element of the interface. The first term is the heat flux on the fluid boundary and the second term is the dissipation rate inside the bulk fluid. The second term can be related to the vorticity: $\int v_j \partial_i \sigma'_{ij} dV = \eta \int v_j \Delta v_j dV = -\eta \int \vec{v} \cdot (\nabla \times \vec{\Omega}) dV$. Since the Reynolds number of the external fluid is very small in the experimental setup ($Re \approx 10^{-4}$ [200]), we may take the external flow to be as irrotational (vanishing vorticity) by recalling the experiment of flow through a cylindrical solid: an irrotational-rotational flow transition occurs at $Re \sim 1$, below which the flow is irrotational [212]. In the shrinking process, the toroidal droplet moves in the external fluid. This is equivalent to flow through the toroidal droplet. Since the viscosity of the internal fluid is very small in this case, the internal dissipation can be neglected. Thus we need to calculate only the surface integral in Eq.(10) to obtain the dissipation rate. We need the viscous stress on the boundary to evaluate the surface integral. Rotational symmetry and the limiting condition $\eta_i/\eta_o \ll 1$ imply both $\sigma'_{r\theta}$ and $\sigma'_{r\alpha}$ vanish at the interface. To determine $\sigma'_{rr} = 2\eta_o \partial_r v_r$ we need the gradient of v_r at the interface. Assuming that the fluid particles *near* the boundary move together with the interface during shrinking, as a result of the viscous external fluid, we have

$$\partial_r v_r|_{interface} = \frac{6R_1}{R^2} \dot{R} \cos \alpha. \quad (6.54)$$

Inserting Eq.(11) along with the velocity field on the interface into the surface term of Eq.(10) yields

$$\dot{E}_{vis} = -24\pi^2 \eta_o \left(\left(\frac{R_1}{R} \right)^2 - \frac{1}{2} \right) R \dot{R}_1 \dot{R}_2 . \quad (6.55)$$

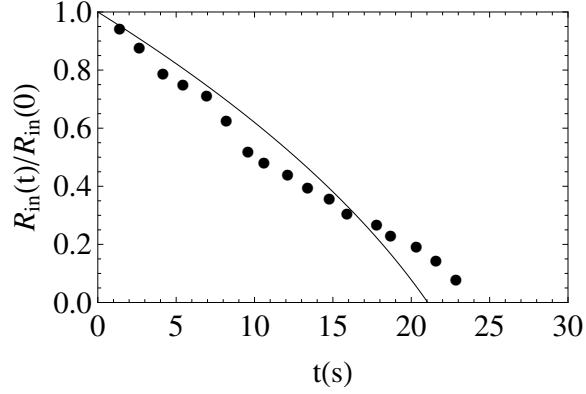


Figure 6.7: The time evolution of the normalized inner droplet radius $R_{in}(t)/R_{in}(0)$ for initial aspect ratio 1.4. The theoretical result is the solid curve and the experimental data points are taken from Ref.[200]. Parameters: $R_1(0) = 3$ mm; $v_s = \sigma/\eta_o = 133$ $\mu\text{m/s}$.

By equating the rate of change of the free energy from Eq.(6.1) and the dissipation rate Eq.(6.55), we have

$$\dot{R}_2(t) = \frac{v_s}{12} \frac{1}{\phi^2(t) - 1/2} \quad (6.56)$$

and the interior hole of the droplet decreases in size according to

$$\dot{R}_{in}(t) = -\frac{v_s}{12} \frac{2\phi(t) + 1}{\phi^2(t) - 1/2}, \quad (6.57)$$

where $\phi(t) = R_1(t)/R(t)$ and $v_s = \sigma/\eta_o$. The shrinking speed is controlled by the aspect ratio of the droplet, in accord with experimental observations [200]. In the limit of infinite aspect ratio (the cylinder) the shrinking speed vanishes, as required. The constant $1/2$ in the denominator of Eq.(6.56) plays an important role in the limit that the aspect ratio approaches one (fat tori). The plot of $R_{in}(t)/R_{in}(0)$ versus t is shown in Fig.6.7 for an initial aspect ratio $R_1(0)/R(0) = 1.4$, $\eta_i/\eta_o = 1/30,000$, $\sigma = 4$ mN/m, $R_1(0) \approx 3$ mm and $\eta_i = 10^{-3}$ kg/(m · s). For these parameters $v_s = \sigma/\eta_o \approx 133$ $\mu\text{m/s}$. Fig.6.7 shows that droplets shrink with roughly constant speed, as found in [200]. Our results predict that it would take about 21 s (aspect ratio 1.4) and 50 s (aspect ratio 1.9) for a toroidal droplet to shrink to close the inner hole of toroid, in qualitative agreement with the experimental values of 25 s

and 38 s respectively. Thus thinner toroidal droplets shrink more slowly, consistent with experimental observations [200].

Our energy conservation approach to determining the shrinking speed can also be applied to a 2-dimensional system where it yields an analytical result. Consider a shrinking hole on a liquid film. The limiting case of a shrinking toroidal liquid droplet with $R_{in} \rightarrow 0$ and $\eta_i/\eta_o \gg 1$ can be modelled as such a 2-dimensional system, since the dynamics of the hole becomes independent of the fluid far away from the hole. As the hole shrinks, a flow will be induced outside the hole on the film. In the Stokes flow regime, the velocity field can be derived analytically in the polar coordinates $\{\rho, \theta\}$ as $v_\rho = \frac{1}{\rho}r(t)\dot{r}(t)$ and $v_\theta = 0$. By energy conservation, the shrinking speed of the hole can also be derived analytically. By equating the rate of change of the line energy $\dot{E}_s = \frac{dE_s}{dt} = 2\pi\gamma \dot{r}$ and the viscous dissipation rate $\dot{E}_{vis} = -\int \rho d\rho d\theta (\sigma'^{\rho\rho} \partial_\rho v_\rho) = -2\pi\eta \dot{r}^2$, we have $\dot{r} = \frac{\gamma}{\eta}$, where η is the viscosity of fluid and γ is the line tension.

We expect that the formalism employed here will have a variety of applications to the dynamics of fluid interfaces. It may also be extended to liquid crystalline droplets where the interplay of liquid crystalline order and the shape of the droplet should be very rich.

Appendix 6.A The shape of the cross section

So far we have assumed that droplets remain perfectly circular in cross-section as they shrink. Here we show that this assumption is well justified.

The shape of a toroidal liquid droplet is characterized by the radii R_1 and R which may in general vary with α and θ . Retaining azimuthal symmetry we consider the following ansatz for R at a fixed time:

$$R(\alpha) = a + c_2 P_2(\cos \alpha) + c_3 P_3(\cos \alpha). \quad (6.58)$$

The second term describes an ellipse which is symmetric about z axis, while the third

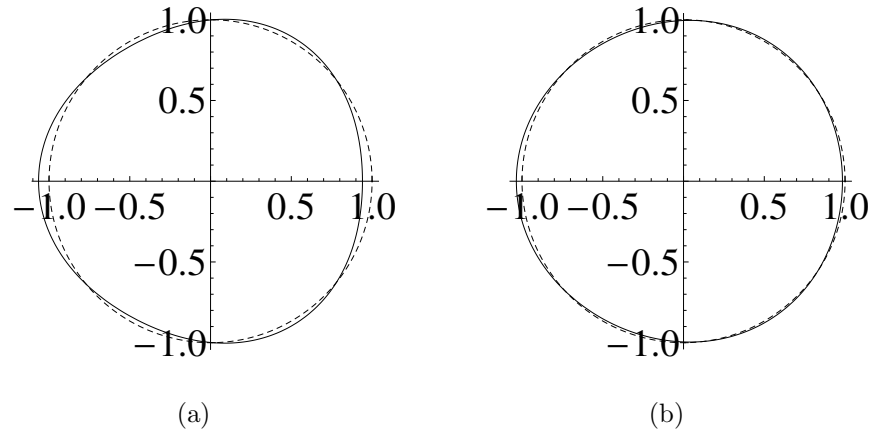


Figure 6.8: Minimum energy cross-sectional shapes within a two parameter family of possible shapes (see Eq.(6.58)). The dashed curves are the unperturbed circular shapes: (a) aspect ratio 10 (thin torus) and (b) aspect ratio 2 (fat torus).

term describes a shape with three round corners, which is asymmetric about the z -axis (we are ignoring the shrinking mode here, described by a $P_1(\cos \alpha)$ term). The shape of the droplet is specified by points in the $\{c_2, c_3 | c_2, c_3 \in [-b, b]\}$ space.

We numerically search for the ground state in the $\{c_2, c_3 | c_2, c_3 \in [-b, b]\}$ space for which

$$L = A - A_0 + \lambda |V - V_0| \quad (6.59)$$

is minimized, where V_0 and A_0 are the volume and surface area of the unperturbed droplet. λ is set to be large to impose volume conservation. We take $a = 1$ and $b = 0.2$.

For tori with typical aspect ratios $R_1/R = 10$ and 2, we find the ground states in the $\{c_2, c_3 | c_2, c_3 \in [-b, b]\}$ space shown in Fig.6.8. The cross-sections are very close to circular. In the experimental work of [200] this is also true.

Appendix 6.B Rayleigh instability vs. shrinking mode

It is observed experimentally[200] that the Rayleigh instability disappears for sufficiently fat solid tori ($R_1(t=0)/R(t=0) \lesssim 2$) whereas the shrinking mode is present for all aspect ratios. Here we derive a lower bound on the aspect ratio for the emergence of the Rayleigh instability.

Two conditions must be satisfied for the Rayleigh instability: (1) modes with wavelength $\lambda > \lambda_c$, where λ_c is the minimum wavelength of the Rayleigh instability mode and (2):

$$u_k(t=t_1) \gtrsim R(t=0), \quad (6.60)$$

where u_k is the perturbation amplitude and t_1 is the lifetime of the shrinking droplet ($R_{in}(t=t_1) = 0$). It is well known [201, 209] that u_k grows exponentially:

$$u_k(t) = u_k(0)e^{v_s t/R(0)}, \quad (6.61)$$

where $v_s = \sigma/\eta$ is the characteristic speed and $R(0)$ the characteristic length scale of the system. We assume that u_k grows exponentially all the way until breakup of the droplet. On the other hand we have shown that $R_{in}(t)$ decreases almost linearly in time. So formally, we have

$$R_{in}(t) = R_{in}(t=0) - v_c t, \quad (6.62)$$

from which we have $t_1 = \frac{R_{in}(t=0)}{v_c}$. By inserting Eq.(6.61,6.62) into Eq.(6.60), we obtain

$$\frac{R_1(0)}{R(0)} \gtrsim 1 + c \ln\left(\frac{R(0)}{u_k(0)}\right), \quad (6.63)$$

where $c = v_c/v_s$ is an aspect ratio factor of order one that tends to 1/2 for aspect ratio one by Eq.(6.57). Thus the Rayleigh instability is dominant for sufficiently thin tori.

It can be checked that for aspect ratios satisfying Eq.(6.63) even the perimeter of the interior of the torus ($2\pi(R_1(0) - R(0))$) can accommodate the Rayleigh instability mode, i.e.,

$$\frac{2\pi(R_1(0) - R(0))}{R(0)} \gtrsim 2\pi \ln\left(\frac{R(0)}{u_k(0)}\right) > 2\pi. \quad (6.64)$$

Chapter 7

Self-propulsion of droplets by spatially-varying surface topography

Under partial wetting conditions, making a substrate uniformly rougher enhances the wetting characteristics of the corresponding smooth substrate – hydrophilic systems become even more hydrophilic and hydrophobic systems even more hydrophobic. In this chapter we show theoretically that spatial texturing of the substrate topography may lead to spontaneous propulsion of droplets. Individual droplets tend to be driven toward regions of maximal roughness for intrinsically hydrophilic systems and toward regions of minimal roughness for intrinsically hydrophobic systems. Spatial texturing can be achieved by patterning the substrate with sinusoidal wrinkles whose wavelength varies in one direction (inhomogeneous wrinkling) or lithographically etching a radial pattern of fractal (Koch curve) grooves on the substrate. Richer energy landscapes for droplet trajectories can be designed by combining texturing of spatial topography with chemical or material patterning of the substrate.

7.1 Introduction

Consider a liquid droplet partially wetting a solid substrate such as glass in contact with a gas such as air. Broadly speaking a substrate may wet easily (hydrophilic) or poorly (hydrophobic) depending on the nature of the substrate, the liquid and the gas. More specifically the three relevant interfacial surface tensions determine the contact angle made by the liquid-gas contact line meeting the plane of the substrate. The contact angle is less than 90° for hydrophilic systems and greater than 90° for hydrophobic systems. A totally wetting thin film corresponds to vanishing contact angle and a complete spherical drop balanced at a point on the substrate corresponds to the superhydrophobic limit with a 180° contact angle.

Uniform surface roughness amplifies the basic wetting characteristics of the corresponding planar system. For hydrophilic/hydrophobic systems the greater substrate area, for a given planar projection, available on the rough substrate makes the wetting more/less favorable and lowers/raises the contact angle. What about surfaces with spatially inhomogeneous properties? Although it is known theoretically and experimentally that variable chemical patterning [218] and Leidenfrost droplets contacting hot surfaces with asymmetric sawtooth patterns [219, 220] can lead to spontaneous propulsion of droplets, we show theoretically that pure inhomogeneous spatial topography of the surface with no other variability is sufficient to drive droplet motion. Droplets are expected to spontaneously move around in the landscape of the surface topography maximizing or minimizing the roughness for naturally hydrophilic/hydrophobic systems respectively. Thus self-propelled droplets can be engineered to follow prescribed paths without external drive by appropriately designing the surface topography. We also propose specific experimentally geometries that could be engineered to observe this phenomenon.

In addition, one may also vary the chemical composition of the surface so that the intrinsic surface tensions are spatially dependent. The combination of chemical and surface topography offers a richer variety of potential structures to obtain desired

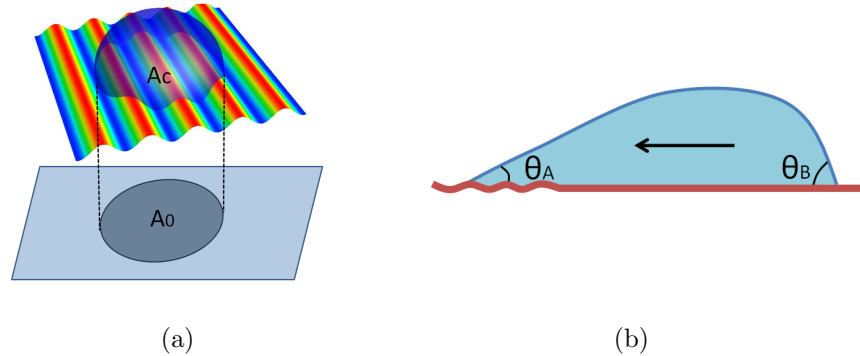


Figure 7.1: (a) A liquid droplet sitting on a rough substrate has more contact area with the substrate ($A_c > A_0$) than the same droplet on an otherwise identical flat substrate. (b) A liquid droplet partially wetting a hydrophilic substrate with inhomogeneous roughness has a smaller contact angle at the rougher end (θ_A) than at the smoother end (θ_B).

flow patterns. The African beetle *Stenocara* fog-basks by tilting forward into the early morning fog-laden wind of the Namib desert and collecting micron-sized water droplets on the smooth hydrophilic peaks of its fused overwings (elytra)[221]. Once a sufficiently massive droplet is formed it rolls downhill against the wind to pool in textured waxy hydrophobic troughs and from there the drop flows to the beetles mouth. Surface structures modeled on the *Stenocara* wings have been synthesized by creating hydrophilic patterns on superhydrophobic surfaces with water/2-propanol solutions of a polyelectrolyte[222].

7.2 Method

The principle of driving liquid droplets via roughness gradients is simple. The free energy of a liquid droplet on a substrate on length scales well below the capillary length, where surface tension dominates over gravity, is $F = -IA_c + \sigma_{SV}A_t + \sigma_{LV}A_{LV}$, where $I = \sigma_{SV} - \sigma_{SL}$ is the imbibition parameter [60], σ_{SL} , σ_{SV} and σ_{LV} are the respective surface tensions between the three phases (Solid/Liquid/Vapor). For water under 1 atm and at room temperature, $\sigma_{LV} = 72$ mN/m. For water on substrates

made of molecular crystals or plastics, $\sigma_{SV} \approx 10-50$ mN/m and $\sigma_{SL} = \sigma_{SO} - \sigma_{LV} \cos \theta$ by Young's relation [60]. A_c is the contact area between the droplet and substrate, A_t is the (constant) total area of a substrate and A_{LV} is the area of the liquid-vapor interface, which is taken to be constant even when a droplet moves. The system of a liquid droplet on a rough substrate may also be viewed as a droplet on a flat substrate with an effective imbibition parameter I_{eff} resulting from the roughness. I_{eff} is defined by $IA_c \equiv I_{eff}A_0$, where A_0 is the planar projection of the actual contact area. For rough surfaces, $A_c > A_0$, as shown in Fig.7.1(a), and therefore $I_{eff}/I > 1$. Up to irrelevant constants, the free energy of a droplet on a rough substrate is

$$F = -I_{eff}(\vec{x})A_0, \quad (7.1)$$

where I_{eff} varies from place to place when the spatial roughness is inhomogeneous. The wetting characteristics of a substrate/liquid composite system determines the sign of I and therefore I_{eff} . A hydrophilic system is characterized by $I > 0$ and an acute contact angle $\theta = \arccos(I/\sigma_{LV})$. A hydrophobic system is characterized by $I < 0$ and an obtuse contact angle [60]. When I , and so I_{eff} , is positive (negative) a substrate lowers (increases) its free energy when covered by a liquid. This spontaneously drives droplets on hydrophilic (hydrophobic) substrates towards rougher (smoother) regions respectively. Eq.(7.1) can also be used to understand the movement of droplets on a chemically heterogeneous substrates where $I_{eff}(\vec{x})$ depends on the wetting characteristics of the chemical composition at the corresponding position on the substrate. Chemical methods that drive droplets by directly modifying the physical imbibition parameter are known [218]. Here we propose that liquid droplets will spontaneously move on substrates with suitable spatially varying topography *alone*, with *no* change in the physical imbibition parameter.

The self-propulsion of liquid droplets on substrates with inhomogeneous roughness can also be understood in terms of the uneven distribution of the Laplace pressure across the droplet. The contact angle for a rough substrate (θ_r) is given by $\cos \theta_r = r \cos \theta$, with $r = A_c/A_0$ [223]. Thus surface roughness amplifies the intrinsic

wetting properties of the corresponding planar substrate. Take a droplet spanning a hydrophilic surface that is rougher on the left than on the right, as illustrated in Fig.7.1 (b). The contact angle is then smaller on the left than on the right: $\theta_A < \theta_B$. The mean curvature H at the B end thus exceeds that at the A end, leading to a Laplace over-pressure ($P = 2\sigma_{LV}H$) gradient from right to left driving the droplet to the rougher part of the surface. The reverse argument applies to a hydrophobic substrate, leading to motion towards the smoother part of the substrate. The self-propulsion of a droplet on a substrate with spatially varying roughness clearly requires the size of the contact disk between the droplet and the substrate to be larger than the typical size over which the roughness varies significantly.

7.3 Results and discussion

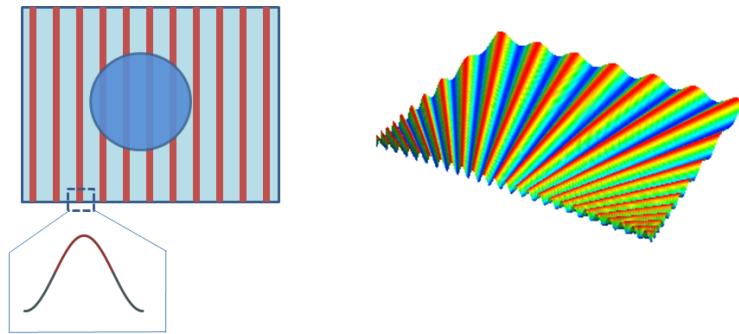


Figure 7.2: Left: a liquid droplet partially wetting a substrate with a uniaxial sinusoidally modulated roughness. Right: Schematic plot of sinusoidal grooves with wavenumber monotonically increasing in the direction orthogonal to the sinusoidal height profile.

To be specific, consider a droplet on a uniaxial sinusoidal substrate, as shown in Fig.7.2, experimentally realizable via wrinkled membranes [224]. The height of the substrate is represented by $z(x) = a_k \cos(kx)$, with translational invariance along the y -direction. The roughness amplitude a_k will be taken much smaller than the maximum height of the droplet so that the shape of the liquid-air interface is unaffected

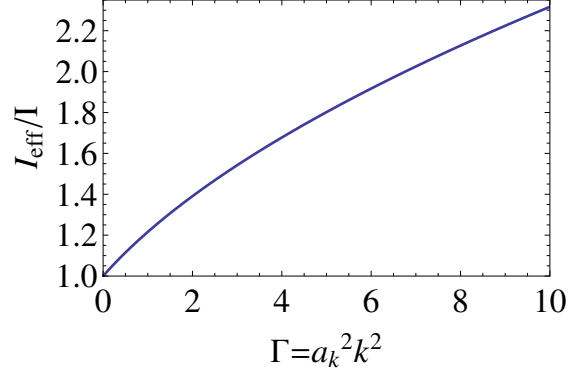


Figure 7.3: The ratio of the effective imbibition parameter to the physical imbibition parameter versus $\Gamma = a_k^2 k^2$ for a liquid droplet partially wetting a sinusoidally modulated substrate.

by the shape of the substrate. For small amplitude roughness liquid droplets can be in complete contact with the substrate, since air pockets do not form underneath the liquid [60, 223]. The effective imbibition parameter is given by

$$\frac{I_{eff}}{I} = \frac{4}{\pi} \int_0^1 dy \sqrt{1-y^2} \sqrt{1 + \Gamma \sin^2(\tilde{k}y)}, \quad (7.2)$$

where $\tilde{k} = kR$ is the dimensionless wavenumber and $\Gamma = a_k^2 k^2$. Clearly Γ , arising from the gradient of the substrate height, is the parameter controlling the effective imbibition. For $R \gg \frac{2\pi}{k}$, Eq.(2) simplifies to [225]

$$\frac{I_{eff}}{I} = \frac{2}{\pi} R(\Gamma), \quad (7.3)$$

where $R(x) = \int_0^{\pi/2} d\theta \sqrt{1 + x \sin^2 \theta}$. In this limit the effective imbibition parameter is dependent only on the product of the amplitude and the wavenumber of the sinusoidal substrate. Fig.7.3 is a numerical plot of the monotonic growth of I_{eff}/I vs. Γ . I_{eff}/I is doubled for $\Gamma \approx 8$. A simple gradient of the effective imbibition parameter over the substrate can be achieved by varying the wavenumber k along the groove axis (y), as shown in the schematic Fig.7.2. Droplets are expected to migrate to maximize/minimize the contact area for intrinsically hydrophilic/hydrophobic substrates. The magnitude of the driving force along the groove axis is proportional to

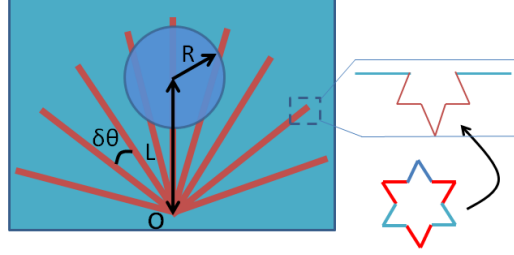


Figure 7.4: A substrate etched by fractal grooves. The cross-sectional shape of the grooves is the lower half of the Koch curve, as shown in the inset.

the gradient of the effective imbibition parameter:

$$\nabla_y I_{eff} = \frac{2I}{\pi} [R(\Gamma) - S(\Gamma)] \frac{d \ln \tilde{k}(y)}{dy}, \quad (7.4)$$

where $S(x) = \int_0^{\pi/2} \frac{d\theta}{\sqrt{1+x \sin^2 \theta}}$, and $R(x) - S(x) = \frac{\pi x}{4} - \frac{3\pi x^2}{32} + \mathcal{O}(x^3)$. The driving force thus depends rather weakly on $\tilde{k}(y)$ and vanishes as Γ approaches zero.

Rough substrates may also be designed based on fractals [226]. Consider a substrate with etched grooves whose cross section is the lower half of the Koch curve, as illustrated in Fig.7.4 [227]. The Koch curve may be constructed by starting with an equilateral triangle of side length a_0 and perimeter $L_0 = 3a_0$, then recursively adding equilateral triangles symmetrically on each line segment. After n steps, the perimeter of the new graph becomes $L_n = L_0(4/3)^n$ with the length of each elementary line segment being $a_n = a_0(1/3)^n$. The Hausdorff, or self-similarity, dimension of the Koch curve is $d_H = \ln 4 / \ln 3 \approx 1.26$ [228]. The order of a physically realizable Koch curve has an upper limit for the order $n_{max} = \frac{\ln(a_0/a_n)}{\ln 3} \sim 8$ by specifying $a_n \sim 10$ nm and $a_0 \sim 0.1$ mm [229]. Now consider a set of close-packed evenly aligned straight grooves constructed from an n -th order Koch curve. The distance between two neighboring grooves is twice the breadth of a groove. The contact area between a droplet of radius R and the fractal substrate, in the limit R much bigger than the breadth of a groove, is $A_c = \pi R^2 [1 + q(n)]$, where $q(n = 0) = 3/4$ and $q(n > 0) = 2(4/3)^{n-2} - 1/2$. Since

$q(n)$ is always positive, $A_c/A_0 > 1$. The effective imbibition parameter is

$$\frac{I_{eff}}{I} = 1 + q(n). \quad (7.5)$$

Thus the effective imbibition parameter depends only on the order of the Koch curve n and is independent of the seed side length a_0 . I_{eff}/I is two for $n = 1$ and exceeds 10 for $n = 8$. Note that the extra volume of liquid inside the finer structure of the fractal grooves is negligible in the limit of large n as the area A_n of the n -th order Koch curve converges: $\lim_{n \rightarrow \infty} A_n = 2\sqrt{3}a_0^2/5 \sim a_0^2 \ll a_0h$, where h is the droplet thickness.

An effective roughness gradient can be made by etching a radial array of grooves with Koch cross-section, as sketched in Fig.7.4. We take an intrinsically hydrophobic surface inclined at an angle α to the horizontal. A droplet sitting near the origin (O) of the radial array is expected to move upward to reduce the contact energy provided the gradient of the effective imbibition parameter is sufficient to overcome gravity. The number of grooves covered by a droplet of size R is $N = 2R/(L\delta\theta)$, where $\delta\theta$ is the angular distance between neighboring grooves and L is the distance of the droplet from the origin. For simplicity, consider the “far-field” limit in which the droplet is sufficiently far from the origin that all the grooves under the droplet are effectively parallel. The change in contact area due to the roughness is $\Delta A = A_c - A_0 = \frac{1}{2}N\pi(b_n - l_0)R$, where b_n is the area of a groove of unit length with $b_n(n > 0) = \frac{3a_0}{2}(\frac{4}{3})^n$ and $b_n(n = 0) = 5a_0/3$, and $l_0 = 2a_0/3$ is the groove breadth. This results in an effective imbibition parameter

$$\frac{I_{eff}}{I} = 1 + \frac{b_n - l_0}{L\delta\theta}. \quad (7.6)$$

A droplet rising up a distance δL increases its gravitational potential energy by $\delta W = mg\delta L \sin \alpha$, where $m \sim \rho R^2 h$ is the mass of the droplet. Meanwhile the surface energy decreases by $\delta F = A_0 \delta I_{eff}$, where $\delta I_{eff} = I_{eff}(L + \delta L) - I_{eff}(L)$. Spontaneous climb therefore requires $\delta I_{eff}/\delta L > mg \sin \alpha / A_0$. Inserting Eq.(7.6) for the effective

imbibition parameter yields

$$\frac{b_n - l_0}{l_0} > \frac{L^2 \delta\theta \, mg \sin \alpha}{A_0 I l_0}. \quad (7.7)$$

This condition can be satisfied for large droplets near the origin on substrates with dense grooves. The right hand side of Eq.(7.7) is of order $10 \sin \alpha$ for $L \sim \text{cm}$, $R \sim \text{mm}$, $I \sim \text{mN/m}$, $\delta\theta \sim a_0/L$ and $h \sim 0.1R$. Since $(b_n - l_0)/l_0 \sim 10$ for $n = 5$, radially carved grooves made of the 5-th order Koch curves would generate sufficient roughness gradient to drive droplets uphill.

There are several points in our analysis that may ultimately call for a more thorough treatment. Sharp substrate edges impede the motion of droplets via pinning of the triple line [230]. Adhesion hysteresis may also arise from the microscopic interactions between a droplet and the substrate [231]. These two effects are the main source of frictional energy dissipation [232]. We have neglected entirely viscous dissipation due to internal fluid flow within moving droplets [60, 81]. The contact angle hysteresis may also impede the motion of a droplet on a rough hydrophilic surface, while there is no contact angle hysteresis on a rough hydrophobic surface due to strong thermal fluctuations at the liquid-solid interface on the nanoscale [233]. In addition, in response to the roughness gradient of a substrate, the originally circular contact profile of a liquid droplet may distort towards the more wettable region to reduce the contact energy.

The geometry-driven propulsion of droplets in a system with axial symmetry is found in both nature and the lab either in a tapered tube or along a spider silk fiber with a conic spindleknots structure [234, 235]. In this chapter, we show theoretically that liquid droplets on substrates can be driven by pure inhomogeneous spatial topography. The size of a droplet is required to be smaller than the capillary length such that gravity can be ignored, but big enough to sense the gradient of roughness. In addition to chemical, electrical and thermal methods, the geometric patterning method provides a new way of controlling droplet flow on substrates which we expect to find application in a variety of areas of wetting research.

Chapter 8

The electric double layer structure around charged spherical interfaces

8.1 Introduction

Charged objects in electrolyte solutions are surrounded by electric double layers (EDL) [93]. One ionic layer is due to a host of chemical interactions, and the second layer is formed by the excess of oppositely charged ions in the solution, screening the charged objects. The EDL structure is responsible for the stability of colloidal dispersions [85] and various electrostatic phenomena in biophysical systems [86]. The distribution of the screening potential in EDL is characterized by the Poisson-Boltzmann (PB) equation. In this chapter, we will study the EDL structure around charged spherical interfaces, which are ubiquitous in colloidal and biophysical systems [236, 237].

Largely due to its nonlinear nature, analytical solutions to the PB equation are available only for planar [238] and cylindrical [239] systems. For a spherical system, the analytical solution to the linearized PB equation is available [85]. Despite a recently proposed analytical series solution [240], a formally simple approximate solution is still in demand for studying analytical problems that are based on the

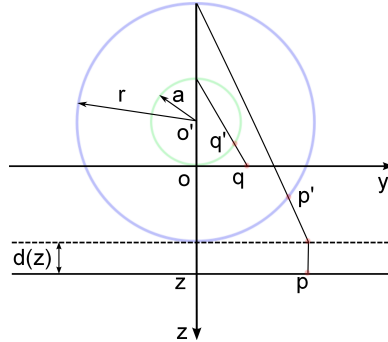


Figure 8.1: The mapping from the $z > 0$ bulk space to the space outside a sphere with radius a (represented by the blue circle) via consecutive stereographic projections from a plane to a sphere. A deviation $d(z)$ is introduced to guarantee the equality of the potential on the blue spherical shell and the potential at the plane located at z .

screening potential in EDL. Numerical techniques[241] and the Debye-Huckel linearized approximations have long been the only available basic methods to solve the PB equation. Various perturbative solutions have been proposed based on the planar solution [242], or the linearized solution [243], as the zeroth order approximation. Perturbative methods that start with the planar solution are limited to the regime of large spherical radius, while those which start with the linearized solution work in the weak potential regime. The geometric construction of a formally simple approximate analytical solution that can match both the planar and the linearized solutions is one concern of this letter.

8.2 Approximate spherical solution to the PB equation

In q :- q symmetric electrolytes, the dimensionless Poisson-Boltzmann equation is [85]

$$\Delta\psi = \sinh \psi, \quad (8.1)$$

in the natural units $k_B T/q$ and the Debye length $\kappa^{-1} = \sqrt{\epsilon k_B T / (8\pi n q^2)}$. q is the absolute value of the charge of ions. We propose an analytic scheme to yield an ap-

proximate solution to the Poisson-Boltzmann equation in a spherical system from the known analytical solution to the planar problem. The planar and spherical systems are connected by a geometric mapping defined in Fig. 8.1. Both the planar and spherical systems are schematically plotted in Fig. 8.1. The planar system is composed of a charged plate locating on the x-y plane with the solution in the $z > 0$ bulk space; and the corresponding spherical system consists of a charged sphere of radius a centered at the origin, which is immersed in the solution in the $r > a$ bulk space. The surface potential in both systems is denoted as ψ_0 . The potential in the planar system is known as $\psi(z)$, while that around the corresponding spherical system is $\psi(r)$. These two potentials can be related by a geometric mapping which is defined as follows. By moving an arbitrary equipotential plane at z in the planar system by $d(z)$ followed by a stereographic projection as shown in Fig. 8.1, the equipotential plane $\psi(z)$ in the plate system is geometrically mapped to the equipotential spherical shell $\psi(r(z))$ in the corresponding spherical system. The charged plate on the x-y plane is mapped to the spherical interface at $r = a$, so $d(z = 0) = 0$. The whole $z > 0$ bulk space in the planar system can be mapped to the bulk space outside the spherical interface by repeating the mapping defined above for all equipotential planes below the x-y plane.

The displacement field $d(z)$ is introduced to guarantee that

$$\psi(z) = \psi(r) \tag{8.2}$$

with $r = a + z - d(z)$. $d(z)$ encodes all information of the potential about the spherical interface. Geometrically $d(z)$ describes how the equipotential planes in the planar system squeeze to form the equipotential spherical shells in the corresponding spherical system. The problem for solving the PB equation in a spherical system is now converted to solving for the geometric deviation $d(z)$. The form of $d(z)$ can be found in the weak potential regime where both $\psi_L(z)$ of a planar system and $\psi_L(r)$ of a spherical system are known:

$$\psi_L(z) = \psi_0 e^{-z}, \tag{8.3}$$

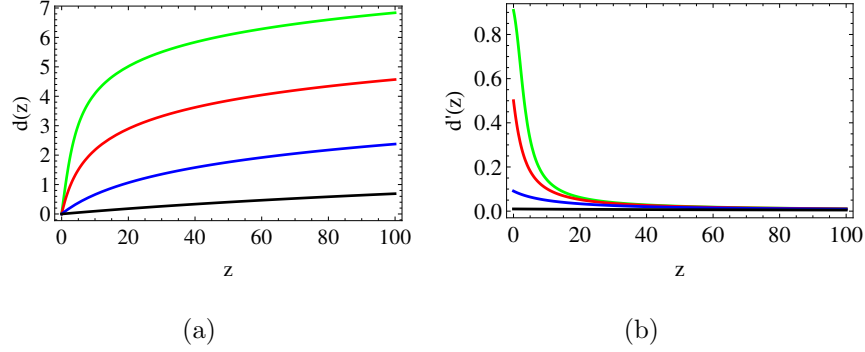


Figure 8.2: (a) The plot of the displacement field $d(z)$ for various spherical radii: $a = 0.1$ (green), $a = 1$ (red), $a = 10$ (blue), $a = 100$ (black). As $a \rightarrow \infty$, $d(z)$ is expected to vanish. (b) The plot of the strain fields $d'(z)$ for the corresponding displacement fields $d(z)$ in (a).

and

$$\psi_L(r) = \psi_0 \frac{a}{r} e^{a-r}, \quad (8.4)$$

where a is the radius of the spherical interface and the subscript L stands for linearized solution. Inserting Eq. (8.3, 8.4) into Eq. (8.2) leads to $a/(a+z-d(z)) = \exp(-d(z))$, from which we have

$$d(z) = a + z - W(ae^{a+z}), \quad (8.5)$$

where $W(x)$ is the Lambert's W function defined by $x = W(x) \exp(W(x))$ [244]. It is checked that $d(z \rightarrow 0) = 0$ and $d(z) \rightarrow 0$ as $a \rightarrow \infty$. And $d(z \rightarrow \infty) \sim \ln(z/a)$, since asymptotically $W(x \rightarrow \infty) \sim \ln x - \ln(\ln x)$ (Ref. [12]). The Lambert's W function is also found in other physical systems, such as the fringe field of a capacitor and Wiens displacement law in black body radiation [245]. Eq. (8.5) shows that $d(z)$ is independent of ψ_0 in the weak potential limit, since ψ_0 appears as a prefactor in both $\psi(z)$ and $\psi(r)$ in the weak potential limit as shown in Eq. (8.3, 8.4).

The plot of $d(z)$ for various spherical radii is given in Fig. 8.2 (a). The squeezing of equipotential surfaces near a spherical interface with smaller radius is seen to be larger. It is expected that the displacement vanishes for an infinitely large spherical interface that approaches a plate. Fig. 8.2 (a) also shows the behaviors of $d(z)$ in two regions –

steep slope for small z and much smaller slope for large z where $d(z \rightarrow \infty) \sim \ln(z/a)$. It gives the qualitative picture of forming equipotential spherical shells from the corresponding equipotential planar slices. Near the charged spherical interface each slice moves more than the slice ahead of it that is closer to the interface. In the region far away from the interface, the squeezing is much more uniform. The relative squeezing of equipotential surfaces is better demonstrated in terms of the “strain” field $d'(z)$. The strain field plotted in Fig. 8.2 (b) shows that the strain is concentrated near the spherical interface and the strain concentration is more significant near spherical interfaces of smaller radii.

We suggest that the form of $d(z)$ for arbitrary ψ_0 be approximated by Eq. (8.5) under the assumption of weak dependence of $d(z)$ on ψ_0 . This assumption is to be substantiated later. We can then construct the analytical approximate solution to the PB equation for a spherical system from the known analytical solution to a planar system, which is

$$\psi = 2 \ln \frac{1 + \gamma e^{-z}}{1 - \gamma e^{-z}}, \quad (8.6)$$

where $\gamma = (\exp(\psi_0/2) - 1) / (\exp(\psi_0/2) + 1)$. On the other hand, $r(z) = W(a \exp(a+z))$ and $W(a \exp(a+z)) \exp(W(a \exp(a+z))) = a \exp(a+z)$ yield

$$z(r) = r - a + \ln(r/a). \quad (8.7)$$

The approximate solution denoted as $\psi_G(r)$ for the spherical system is thus derived as

$$\psi_G(r) = 2 \ln \left[\frac{1 + \gamma \exp(-(r - a + \ln(r/a)))}{1 - \gamma \exp(-(r - a + \ln(r/a)))} \right], \quad (8.8)$$

where the RHS is the potential in the corresponding plate system with z replaced by $z(r)$. Near a spherical interface of large radius, i.e., $(r-a)/a \ll 1$ and $a \gg 1$, the ψ_G solution approaches the planar solution, as required. In the region far away from the interface ($r \gg a$), Eq. (8.8) becomes $\psi_G(r) = 4\gamma a \exp(-(r-a))/r$, which reduces to the linear spherical solution Eq. (8.4) in the weak potential limit. Note that the ψ_G

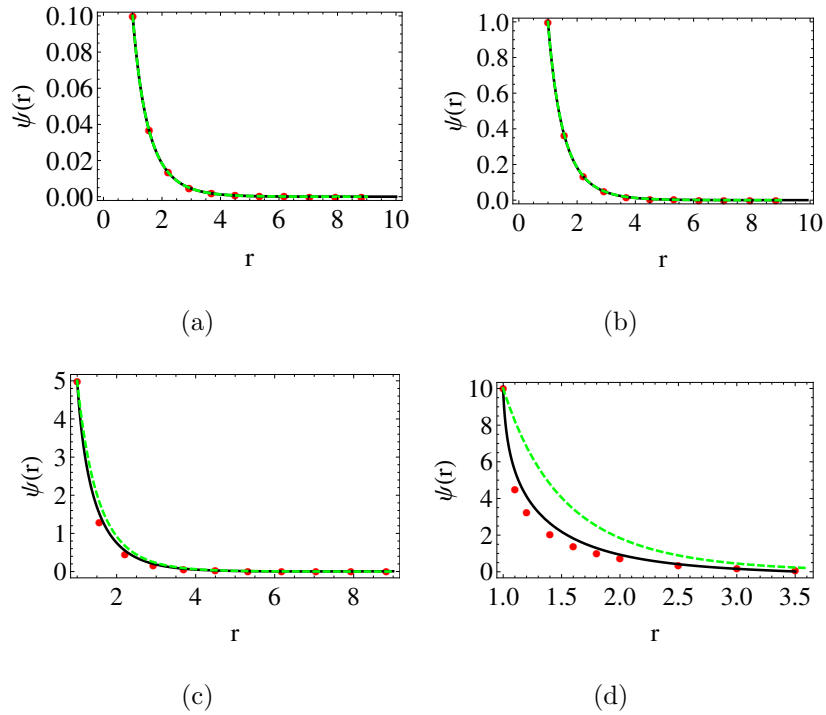


Figure 8.3: The potential around a charged spherical interface of unit radius in a q:q solution. The surface potentials in (a)-(d) are respectively 0.1, 1, 5, 10 measured by $q/(k_B T)$. The curves give the numerical solution to the Poisson-Boltzmann equation (black), analytical solution for weak ψ_0 (green dashed) and the solution constructed by the our method (red dots).

solution may be derived algebraically by a variable substitution $s = a/r \exp(-(r-a))$ in Eq. (8.1) and more accurate results can be obtained by perturbation analysis [246, 247]. In comparison to the algebraic method, the derivation of the ψ_G solution via the geometric mapping not only reduces the complexity of algebraic calculations, but also shows how the spherical geometry modifies the equipotential surfaces of a planar system as encoded by the geometric deviation $d(z)$. The relation between the ψ_G solution and both the linearized and planar solutions is also revealed in the geometric derivation.

8.3 Applicability of the geometric solution

Eq. (8.8) is derived from the planar and the linearized spherical solution, so at the very least it is expected to work for either $a \gg 1$ or $\psi_0 \ll 1$. It is therefore superior to the linear solution, which only works in the weak potential limit. The region of validity of the ψ_G solution can be derived algebraically. By introducing $x = 1/r$, the PB equation for a spherical system becomes [248]

$$C(x) \frac{\partial^2}{\partial x^2} \psi = \sinh \psi, \quad (8.9)$$

where $C(x) = x^4$. Inspired by the functional form of the planar and the linearized spherical solutions Eqs.(8.3, 8.4), we use $\psi(x) = 2 \ln((1 + g(x))/(1 - g(x)))$ as a trial solution. Depending on the sign of $\psi(x)$, $g(x) = \pm \exp(-f(x))$ and $g(x) \in (-1, 1)$ corresponding to $\psi \in (-\infty, \infty)$. Inserting the ansatz into Eq. (8.9) yields

$$g(x)[C(x)(f'^2 - f'') - 1] + g^3[C(x)(f'^2 + f'') - 1] = 0. \quad (8.10)$$

For $|g| \ll 1$, by dropping the g^3 term, the solution to Eq. (8.10) is $f(x) = 1/x - \ln x + c_1$, with an integration constant c_1 . Inserting $f(x)$ into the ansatz ψ yields the ψ_G solution. An alternative condition for dropping the g^3 term in Eq. (8.10) is $C(x)(f'^2 + f'') - 1 \ll 1$, which is equivalent to $x = 1/r \ll 1$ by inserting the expressions for $f(x)$ and $C(x)$. Therefore, for either $|g| \ll 1$ or $x = 1/r \ll 1$, the solution to Eq. (8.10) coincides with the ψ_G solution. Note that $|g| \ll 1$ is equivalent to the weak potential limit, and $x = 1/r \ll 1$ holds for $a \gg 1$ since $r > a$. An important case falls in this region of validity of the ψ_G solution. Consider colloids of size R in a solution of ion strength I (in mol/L). The Debye length is $\kappa^{-1}(\text{nm}) = 0.304/\sqrt{I(\text{mol/L})}$ which is at the order of nm for $I \sim 1$ mol/L [111]. For $R \sim \mu\text{m}$, $a = R/\kappa^{-1} \gg 1$. Therefore, the approximate analytical ψ_G solution is suitable for typical colloidal dispersions. In comparison to the series solution [240], the formal simplicity of the ψ_G solution enables further analytical study of the electrostatics of colloidal systems.

The ψ_G solution turns out to have a larger region of validity. Fig. 8.3 shows comparisons of the ψ_G solution (red dots), the linearized solution (green dashed) and the numerical solution (black) to the PB equation for a spherical system for different potentials. For weak potential ($\psi_0 = 0.1(a), 1(b)$), the three solutions fall on the same curve. The linearized solution works well at least up to $\psi_0 = 5$ without qualitatively deviating from the numerical solution. So the linearized theory applies for moderate values of surface potential [249]. As ψ_0 exceeds 5, the linearized solution starts to deviate from the numerical solution, while ψ_G conforms to the numerical solution up to $\psi_0 = 10$, where the linearized solution deviates significantly the numerical solution. This indicates that the dependence of $d(z)$ on ψ_0 is weak for $a = 1$ up to $\psi_0 = 10$.

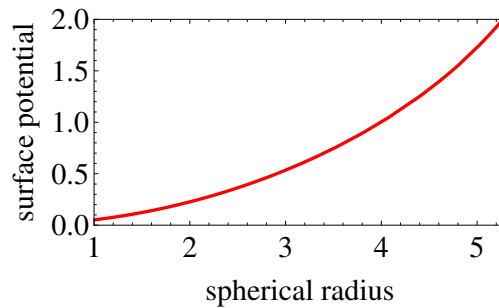


Figure 8.4: The ψ_G solution is applicable below the red curve in the parameter space $\{a, \psi_0\}$. On the red curve, $\delta = \epsilon = 10^{-3}$.

The quality of the ψ_G solution can be systematically studied by defining a ratio $\delta = \max_r \{ |(\Delta\psi - \sinh \psi) / \sinh \psi| \}$. The smaller the ratio δ is, the better the solution is. For a given precision $\epsilon = 10^{-3}$, the applicable region of the ψ_G solution is found to be below the red curve in the parameter space $\{a, \psi_0\}$, as shown in Fig. 8.4. For $a \gtrsim 5$, the ψ_G solution applies even for large potentials. There exists, however, a cut-off value for the surface potential. High potential, or equivalently low temperature, may lead to correlation of counter-ions near the charged interface that is ignored in the mean field PB equation [86]. In addition, high potential leads to high concentration of ions so that the finite dimension of ions must be taken into consideration [85]. The advantage of the ψ_G solution over the planar solution is shown explicitly in Fig. 8.5.

The ψ_G solution works better than the planar solution even for large spherical radius.

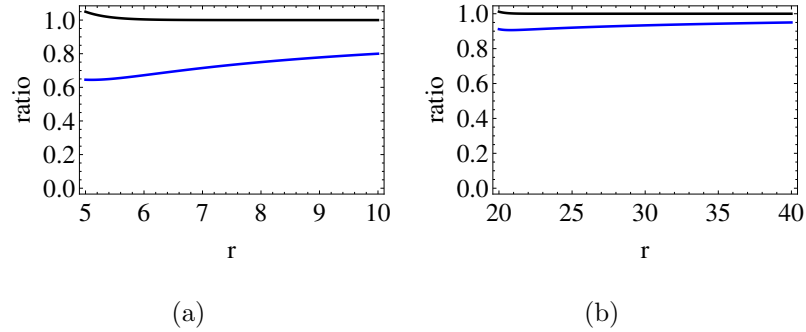


Figure 8.5: The comparison of the ψ_G solution (black) and the planar solution (blue) in terms of the ratio of the LHS to RHS of Eq. (8.1). The radii of the spherical interface are $a = 5(a)$ and $20(b)$. $\psi_0 = 1$.

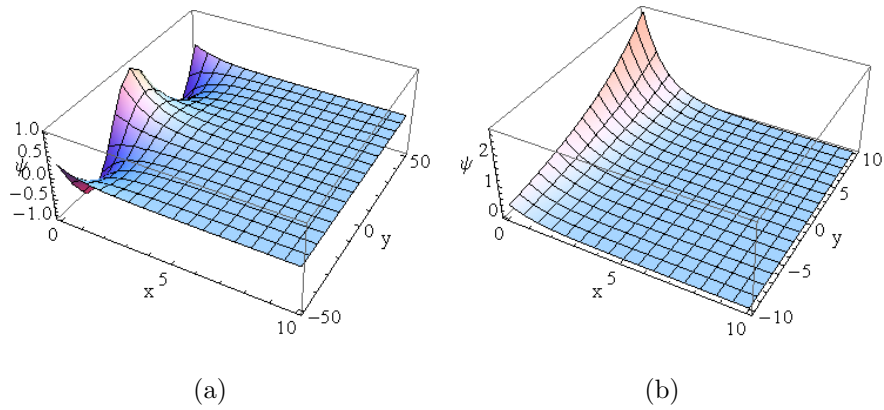


Figure 8.6: The potential distributions ($\exp(\alpha x + \beta y)$) in the double layer corresponding to the periodic (a) and aperiodic (b) boundary conditions. $k_a = k_p = 0.5$.

8.4 Analogy between an EDL system and capillary deformation

We proceed to study how the nonuniform surface potential on a charged spherical interface influences the EDL structure. For simplicity, we work in the regime of

weak potential and large spherical radius, so the system is regarded as locally planar, located on the y-z plane. The solution to the linearized PB equation is

$$\psi(x, y) = \sum_{\beta} A_{\beta} e^{\alpha(\beta)x} e^{\beta y}, \quad (8.11)$$

where $\alpha^2 + \beta^2 = 1$, and A_{β} is determined by the boundary condition $\psi_0(y)$ via $\psi_0(y) = \sum_{\beta} A_{\beta} \exp(\beta y)$. Since α is a function of β , the potential distributions along the x and y-directions are correlated. Now consider two typical boundary conditions - periodic with $\beta = ik_p$ and aperiodic with $\beta = k_a$. For the first case, $\alpha = -\sqrt{1 + k_p^2}$. For the second case, $k_a \ll 1$ is required to guarantee the weak potential condition, and $\alpha = -\sqrt{1 - k_a^2}$. Therefore, the decay length of the potential in the EDL decreases/increases for a periodic/aperiodic distribution of the surface potential.

The plot of the potential distributions for periodic/aperiodic boundary conditions are shown in Fig. 8.6. The profile resembles the capillary deformation near a plate with varying wetting properties. The underlying analogy between an electric double layer and capillary deformation is seen clearly from the following equations. For weak potential the PB Equation is linearized

$$\psi = \kappa^{-2} \Delta \psi = \begin{cases} \kappa^{-2} [\psi''(r) + \frac{1}{r} \psi'(r)], & \text{cylinder} \\ \kappa^{-2} [\partial_x^2 \psi(x, y) + \partial_y^2 \psi(x, y)], & \text{plane} \end{cases}$$

And the capillary deformation $z(r)$ near an immersed object is governed by the shape equation [60]:

$$z(\vec{x}) = 2\lambda_c^2 H(\vec{x}) = \begin{cases} \lambda_c^2 [z''(r) + \frac{1}{r} z'(r)], & \text{cylinder} \\ \lambda_c^2 [\partial_x^2 z(x, y) + \partial_y^2 z(x, y)], & \text{plane} \end{cases}$$

which holds for weak deformation. $2H(\vec{x}) = 1/R_1 + 1/R_2$ is the mean curvature at the point \vec{x} on the liquid interface, and $\lambda_c = \sqrt{\sigma/(\rho g)}$ is the capillary length comparing the competition between surface tension and gravity. The analogy between an EDL system and capillary deformation allows the use of well-developed methods for the calculation of electrostatic interactions in DLVO theory in less well-studied lateral capillary interactions between particles adsorbed at a liquid-fluid interface [120].

8.5 Conclusion

In conclusion, we have studied the EDL structure around charged spherical interfaces by analysis of the Poisson-Boltzmann equation. Despite the point charge assumption of electrolyte ions and the neglect of ion-ion corrections, the PB equation generally works well especially for problems of electrostatic interaction of colloidal particles [93]. In this chapter, we have derived an approximate analytical solution to the Poisson-Boltzmann equation for the spherical system by a geometric mapping. The formal simplicity of the ψ_G solution enables further analytical study of spherical systems. The regime of applicability includes not only the weak potential regime where the linearized solution also works well, but also the regime of large spherical radius. Typical colloidal dispersions with the size of colloids much bigger than the Debye length fall in the latter regime.

Bibliography

- [1] L. Giomi, Doctoral Thesis (2009).
- [2] R. Kamien, *Reviews of Modern Physics* **74**, 953 (2002).
- [3] D. Nelson, *Defects and Geometry in Condensed Matter Physics* (Cambridge University Press, 2002), 1st ed.
- [4] D. R. Nelson, T. Piran, and S. W. ed, *Statistical Mechanics of Membranes and Surfaces* (World Scientific, Singapore, 2004).
- [5] D. Hilbert and S. Cohn-Vossen, *Geometry and the imagination* (Chelsea Publishing Company, 1952).
- [6] D. Struik, *Lectures on Classical Differential Geometry* (Dover Publications, 1988), 2nd ed.
- [7] T. Frankel, *The Geometry of Physics, An Introduction* (Cambridge Press, 1997), revised edition ed.
- [8] S. Safran, *Statistical Thermodynamics of Surfaces, Interfaces, and Membranes* (Westview Press, 2003).
- [9] P. Chaikin and T. Lubensky, *Principles of Condensed Matter Physics* (Cambridge University Press, 1995), 1st ed.
- [10] M. Bowick and L. Giomi, *Advances in Physics* **58**, 449 (2009).

- [11] H. Shin, Doctoral Thesis (2008).
- [12] D. Shechtman, I. Blech, D. Gratias, and J. W. Cahn, Phys. Rev. Lett. **53**, 1951 (1984).
- [13] D. Levine and P. J. Steinhardt, Phys. Rev. Lett. **53**, 2477 (1984).
- [14] J. Farges *et al*, J. Phys. (Paris) **36**, C2 (1975).
- [15] J. Farges *et al*, J. Phys. (Paris) **38**, C2 (1977).
- [16] J. Farges *et al*, Surf. Sci. **106**, 95 (1981).
- [17] M. Kleman and J. F. Sadoc, J. Phys. Lett. (Paris) **40**, 569 (1979).
- [18] J. F. Sadoc and R. Mosseri, Philos. Mag. B **45**, 467 (1982).
- [19] P. J. Steinhardt, D. R. Nelson, and M. Ronchetti, Phys. Rev. Lett. **47**, 1297 (1981).
- [20] D. R. Nelson, Phys. Rev. Lett. **50**, 982 (1983).
- [21] M. Kleman, Adv. Phys. **38**, 605 (1989).
- [22] A. Horvat *et al.*, ACS Nano **2(6)** (2008).
- [23] D. Nelson and L. Peliti, J.Phys.(France) **48**, 1085 (1987).
- [24] V. Berezinskii, Sov. Phys., JETP **32**, 493 (1971).
- [25] J. M. Kosterlitz and D. J. Thouless, J. Phys. C **5**, L124 (1972).
- [26] J. M. Kosterlitz and D. J. Thouless, J. Phys. C **6**, 1181 (1973).
- [27] J. M. Kosterlitz, J. Phys. C **7**, 1046 (1974).
- [28] M. Bowick, D. Nelson, and A. Travasset, Physical Review B **62**, 8738 (2000).

- [29] M. Bowick, D. R. Nelson, and A. Travesset, Phys. Rev. Lett. **89**, 185502 (2002).
- [30] A. Perez-Garrido, M. Dodgson, and M. Moore, Phys. Rev. B **56**, 3640 (1997).
- [31] L. Giomi and M. Bowick, Phys.Rev.B **76**, 054106 (2007).
- [32] M. Bowick, D. Nelson, and A. Travesset, Physical Review E **69**, 041102 (2004).
- [33] V. Vitelli and D. Nelson, Physical Review E **70**, 051105 (2004).
- [34] V. Vitelli, J. Lucks, and D. Nelson, Proceedings of the National Academy of Sciences **103**, 12323 (2006).
- [35] W. Irvine, V. Vitelli, and P. Chaikin, Nature **468**, 947 (2010).
- [36] B. Mbanga, G. Grason, and C. Santangelo, Phys. Rev. Lett. **108**, 017801 (2012).
- [37] M. Bowick, H. Shin, and A. Travesset, Physical Review E **75**, 021404 (2007).
- [38] H. Shin, M. Bowick, and X. Xing, Phys. Rev. Lett. **101**, 037802 (2008).
- [39] F. MacKintosh and T. Lubensky, Phys. Rev. Lett. **67**, 1169 (1991).
- [40] T. Lubensky and J. Prost, J. Phys. II France **2**, 371 (1992).
- [41] X. Xing, J. Stat. Phys. **134**, 487 (2008).
- [42] D. Nelson, Nano. Lett. **2**, 1125 (2002).
- [43] R. Kamien, Science **299**, 1671 (2003).
- [44] K. Shin *et al*, Science **306**, 76 (2004).
- [45] A. Jackson *et al*, J. Am. Chem. Soc. **128**, 11135 (2006).
- [46] S. Glotzer and M. Solomon, Nat. Mater. **6**, 557 (2007).
- [47] S. Bon, S. Cauvin, and P. Colver, Soft Matter **3** (2007).

- [48] X. He and F. Schmid, Phys. Rev. Lett. **100** (2008).
- [49] L. Jia, A. Cao, D. Lévy, B. Xu, P. Albouy, X. Xing, M. Bowick, and M. Li, Soft Matter **5**, 3446 (2009).
- [50] L. Jia, P. Albouy, A. Di-Cicco, A. Cao, and M. Li, Polymer **52**, 2565 (2011).
- [51] L. Jia, D. Lévy, D. Durand, M. Imperor-Clerc, A. Cao, and M. Li, Soft Matter **7**, 7395 (2011).
- [52] J. Frank and M. Kardar, Phys. Rev. E **77**, 041705 (2008).
- [53] N. Upadhyaya and V. Vitelli, Phys. Rev. E **84** (2011).
- [54] X. Xing *et al.*, accepted by PNAS (arXiv:1108.4763v1) (2012).
- [55] T. Witten, Rev. Mod. Phys. **79**, 643 (2007).
- [56] H. King and R. Schroll and B. Davidovitch and N. Menon, A sheet on a drop reveals wrinkling and crumpling as distinct symmetry-breaking instabilities, submitted for publication at PNAS (2012).
- [57] H. Diamant and T. Witten, Phys.Rev.Lett. **107**, 164302 (2011).
- [58] M. Bowick and Z. Yao, Europhys. Lett. **93**, 36001 (2011).
- [59] M. Bowick and L. Giomi, Advances In Physics **58**, 449 (2009).
- [60] P. Gennes, F. Brochard-Wyart, and D. Quéré, *Capillarity and Wetting Phenomena: Drops, Bubbles, Pearls, Waves* (Springer, 2003).
- [61] J. Eggers, Reviews of Modern Physics **69**, 865 (1997).
- [62] A. Frohn and N. Roth, *Dynamics of Droplets (Experimental Fluid Mechanics)* (Springer, 2000), 1st ed.
- [63] A. Abate *et al*, Lab on a Chip **11**, 1713 (2011).

- [64] H. Stone, *Annu.Rev.Fluid Mech.* **26**, 65 (1994), a review paper on droplet deformation in flows, surfactant effect, satellite drops, chaotic flows, tip streams, and capillary instability.
- [65] R. Craster and O. Matar, *Reviews of Modern Physics* **81** (2009).
- [66] C. Isenberg, *The Science of Soap Films and Soap Bubbles* (Dover, 1992).
- [67] R. Deegan, O. Bakajin, T. Dupont, G. Huber, S. Nagel, and T. Witten, *Nature* **389**, 827 (1997).
- [68] B. Weon and J. Je, *Physical Review E* **82**, 015305 (2010).
- [69] W. Han and Z. Lin, *Angew. Chem. Int. Ed. Engl.* **51(7)**, 1534 (2012).
- [70] X. Shi, M. Brenner, and S. Nagel, *Science* **265**, 219 (1994).
- [71] I. Cohen and S. Nagel, *Physics of Fluids* **13**, 3533 (2001).
- [72] I. Cohen, M. Brenner, J. Eggers, and S. Nagel, *Physical Review Letters* **83**, 1147 (1999).
- [73] W. Zhang and J. Lister, *Physical Review Letters* **83**, 1151 (1999).
- [74] B. Zeff, B. Kleber, J. Fineberg, and D. Lathrop, *Nature* **403**, 401 (2000).
- [75] J. Eggers, J. Lister, and H. A. Stone, *J. Fluid Mech.* **401**, 293 (1999).
- [76] J. Paulsen, J. Burton, and S. Nagel, *Phys. Rev. Lett.* **106**, 114501 (2011).
- [77] N. Bohr and J. Wheeler, *Physical Review* **56**, 426 (1939).
- [78] R. Foty *et al*, *Development* **122**, 1611 (1996).
- [79] S. Waitukaitis *et al.*, *Phys. Rev. E* **83**, 051302 (2011).
- [80] Y. Pomeau and E. Villermaux, *Physics Today* p. 39 (2006).

- [81] L. Landau and E. Lifshitz, *Fluid Mechanics* (Pergamon Press, 1987), 2nd ed.
- [82] S. Middleman, *Modeling Axisymmetric Flows* (Academic Press, 1995).
- [83] Z. Yao and M. Bowick, *Eur. Phys. J. E* **34**, 32 (2011).
- [84] Z. Yao and M. Bowick, *Soft Matter* **8(4)**, 1142 (2011).
- [85] E. Verwey and J. Overbeek, *Theory of the stability of lyophobic colloids* (Elsevier, 1948).
- [86] W. Gelbart *et al.*, *Phys. Today* **53**, 38 (2000).
- [87] R. Dias and B. L. ed, *DNA Interactions with Polymers and Surfactants* (John Wiley and Sons, New Jersey, 2008).
- [88] M. Oettel and S. Dietrich, *Langmuir* **24**, 1425 (2008).
- [89] C. Holm, P. Kekicheff, and R. P. ed, *Electrostatic Effects in Soft Matter and Biophysics* (NOTO Science Series II, 2000).
- [90] R. Lipowsky and E. S. ed., *Structure and dynamics of membranes* (Elsevier, 1995).
- [91] L. Landau and E. Lifshitz, *Statistical Physics (Part I)* (Butterworth-Heinemann, 1999).
- [92] D. McQuarrie, *Statistical Mechanics* (Harper Collins, NY, 1976).
- [93] H. Ohshima, *Theory of Colloid and Interfacial Electric Phenomena* (Academic Press Inc., 2006).
- [94] S. Nordholm, *Chem. Phys. Lett.* **105**, 302 (1984).
- [95] R. Penfold *et al.*, *J. Chem. Phys.* **92**, 1915 (1990).
- [96] M. Stevens and M. Robbins, *Europhys. Lett.* **12**, 81 (1990).

- [97] M. Barbosa *et al*, Europhys. Lett. **52**, 80 (2000).
- [98] R. Groot, J. Chem. Phys. **95**, 9191 (1990).
- [99] A. Diehl *et al*, Physica A **274**, 433 (1999).
- [100] C. Patra and A. Yethiraj, J. Phys. Chem. **103**, 6080 (1999).
- [101] P. Debye and E. Huckel, Physik Z. **24**, 185 (1923).
- [102] G. Gouy, J. Phys. (France) **9**, 457 (1910).
- [103] G. Gouy, Ann. Phys. (Leipzig) **7**, 129 (1917).
- [104] D. Chapman, Philos. Mag. **25**, 475 (1913).
- [105] J. Urbanija, Seminar of Electrical double layer, Ljubljana, May 2007.
- [106] I. Borukhov, D. Andelman, and H. Orland, Phys. Rev. Lett. **79**, 435 (1997).
- [107] R. Roa *et al*, Phys. Chem. Chem. Phys. **13**, 3960 (2011).
- [108] A. Grosberg, T. Nguyen, and B. Shklovskii, Rev. Mod. Phys. **74**, 329 (2002).
- [109] Khan, J. Colloid Interface Sci. **101**, 193 (1984).
- [110] Pashley, J. Colloid Interface Sci. **102**, 23 (1984).
- [111] J. Israelachvili, *Intermolecular and Surface Forces* (Academic Press Inc., 1985).
- [112] J. Mahanty and B. Ninham, *Dispersion Forces (Colloid Science)* (Academic Press Inc, 1977).
- [113] J. Zwanikken and M. O. de la Cruz, Phys. Rev. E **82**, 050401 (R) (2010).
- [114] L. Guldbbrand *et al*, J. Chem. Phys. **80**, 2221 (1984).
- [115] Y. Levin, Brazilian Journal of Physics **65**, 1577 (2002).

- [116] Y. Levin, Rep. Prog. Phys. **34**, 1158 (2004).
- [117] G. Manning, J. Chem. Phys. **51**, 924 (1969).
- [118] G. Manning, J. Chem. Phys. **51**, 934 (1969).
- [119] D. Stigter, J. Phys. Chem. **82**, 1604 (1978).
- [120] V. Paunov, Langmuir **14**, 5088 (1998).
- [121] A. Bausch, M. Bowick, A. Cacciuto, A. Dinsmore, M. Hsu, D. Nelson, M. Nikolaides, A. Travasset, and D. Weitz, Advances in Colloid and Interface Science **299**, 1716 (2003).
- [122] M. Bowick, D. R. Nelson, and A. Travasset, Phys. Rev. B **73**, 024115 (2006).
- [123] L. Giomi and M. J. Bowick, Phys. Rev. E **78**, 010601(R) (2008).
- [124] L. Giomi and M. Bowick, Eur. Phys. J. E **27**, 275 (2008).
- [125] L. Giomi and D. Giuliani, <http://physics.syr.edu/~lgiomi/torus/database/>.
- [126] B. Binks, Phys. Chem. Chem. Phys. **9**, 6285 (2007).
- [127] S. Pickering, J. Chem. Soc. **91**, 2001 (1907).
- [128] M. Leunissen, A. van Blaaderen, A. Hollingsworth, M. Sullivan, and P. Chaikin, Proc. Nat. Acad. Sci. USA **104**, 2585 (2007).
- [129] M. Leunissen, J. Zwanikken, R. van Roij, P. Chaikin, and A. van Blaaderen, Phys. Chem. Chem. Phys. **9**, 6405 (2007).
- [130] A. Dinsmore *et al.*, Science **298**, 1006 (2002).
- [131] W. Irvine, A. Hollingsworth, D. Grier, and P. Chaikin, Proc. Nat. Acad. Sci. (2010).

- [132] M. J. Bowick, L. Giomi, H. Shin, and C. Thomas, *Phy. Rev. E* **77**, 021602 (2008).
- [133] L. Giomi and M. Bowick, *Phys. Rev. B* **76**, 054106 (2007).
- [134] M. Rubinstein and D. Nelson, *Phy. Rev. B* **28**, 6377 (1983).
- [135] G. Tarjus, F. Susset, and P. V. <http://arxiv.org/abs/1005.2684v1>.
- [136] F. Sausset, G. Tarjus, and D. Nelson, *Phy. Rev. E* **81**, 031504 (2010).
- [137] C. Modes and R. Kamien, *Phys. Rev. Lett.* **99**, 235701 (2007).
- [138] C. Modes and R. Kamien, *Phys. Rev. E* **77**, 041125 (2008).
- [139] D. W. Henderson and D. Taimina, *Math. Intell.* **23(2)**, 17 (2001).
- [140] J. F. Sadoc and J. Charvolin, *Acta. Cryst. A* **45**, 10 (1989).
- [141] <http://www.gang.umass.edu/>.
- [142] J. Eells, *Math. Intell.* **9**, 53 (1987).
- [143] C. Delaunay, *J. Math. pures et appl.* **1(6)**, 309 (1841).
- [144] N. D. P.A. Kralchevsky, *Current Opinion in Colloid and Interface Science* **6**, 383 (2001).
- [145] K. P.A. Kralchevsky, *Advances in Colloid and Interface Science* **85**, 145 (2000).
- [146] Y. Jung, K. Chu, and S. Torquato, *Journal of Computational Physics* **223**, 711 (2007).
- [147] M. Deserno, *Notes on Differential Geometry* (2004).
- [148] R. Gillette and D. Dyson, *Chemical Engineering* **2**, 44 (1971).
- [149] V. Vitelli, J. Lucks, and D. Nelson, *PNAS* **103**, 12323 (2006).

- [150] J. Weertman and J. Weertman, *Elementary Dislocation Theory* (The Macmillan Company, 1964).
- [151] G. A. Devries *et al.*, *Science* **315**, 358 (2007).
- [152] D. Discher, Y. Won, D. Ege, J. Lee, F. Bates, D. Discher, and D. Hammer, *Science* **284**, 1143 (1999).
- [153] D. Discher and A. Eisenber, *Science* **297**, 967 (2002).
- [154] A. Halperin, *Macromolecules* **23**, 2724 (1990).
- [155] S. Jenekhe and X. Chen, *Science* **279**, 1903 (1998).
- [156] S. Jenekhe and X. Chen, *Science* **283**, 372 (1999).
- [157] A. Nowak, V. Breedveld, L. Pakstis, B. Ozbas, D. Pine, D. Pochan, and T. Deming, *Nature* **417**, 424 (2002).
- [158] E. Bellomo, M. Wyrsta, L. Pakstis, D. Pochan, and T. Deming, *Nat. Mater.* **3**, 244 (2004).
- [159] L. Palmer and S. Stupp, *Acc. Chem. Res.* **41**, 1674 (2008).
- [160] X. Wang, G. Guerin, H. Wang, Y. Wang, I. Manners, and M. Winnik, *Science* **317**, 644 (2007).
- [161] F. He, T. Gadt, I. Manners, and M. Winnik, *J. Am. Chem. Soc.* **133**, 9095 (2011).
- [162] J. Yang, D. Lévy, W. Deng, P. Keller, and M. Li, *Chem. Commun.* **34**, 4345 (2005).
- [163] E. Mabrouk, D. Cuvelier, F. Brochard-Wyart, P. Nassoy, and M. Li, *Proc. Natl. Acad. Sci. USA* **106**, 7294 (2009).

- [164] R. Pinol, L. Jia, F. Gubellini, D. Lévy, P. Albouy, P. Keller, and M. Li, *Macromolecules* **40**, 5625 (2007).
- [165] B. Xu, R. Pinol, M. Nono-Djamen, S. Pensec, P. Keller, P. Albouy, D. Lévy, and M. Li, *Faraday Discussions* **143**, 235 (2009).
- [166] S. Boisse, J. Rieger, A. Di-Cicco, P. Albouy, C. Bui, M. Li, and B. Charleux, *Macromolecules* **42**, 8688 (2009).
- [167] J. del Barrio, L. Oriol, C. Sanchez, J. Serrano, A. Di-Cicco, P. Keller, and M. Li, *J. Am. Chem. Soc.* **132**, 3762 (2010).
- [168] H. Yang, L. Jia, C. Zhu, A. Di-Cicco, D. Lévy, P. Albouy, M. Li, and P. Keller, *Macromolecules* **43**, 10442 (2010).
- [169] L. Miao *et al.*, *Phys. Rev. E* **49**, 5389 (1994).
- [170] S. Svetina and B. Zeks, *Eur. Biophys. J* **17(2)**, 101 (1989).
- [171] W. Helfrich, *Phys. Lett. A* **50**, 115 (1974).
- [172] J. Lidmar, L. Mirny, and D. Nelson, *Phys. Rev. E* **68**, 051910 (2003).
- [173] T. Nguyen, R. Bruinsma, and W. Gelbart, *Phys. Rev. E* **72**, 051923 (2005).
- [174] H. Shin, M. Bowick, and X. Xing, *Phys. Rev. Lett.* **101**, 037802 (2008).
- [175] E. Sackmann, *FEBS Letters* **346**, 3 (1994).
- [176] M. Bates, *J. Chem. Phys.* **128** (2008).
- [177] C. Itzykson and J. Zuber, *Quantum Field Theory* (Dover Publications, 2006).
- [178] P. de Gennes and J. Prost, *The Physics of Liquid Crystals* (Oxford University Press, 1995), 2nd ed.

- [179] M. Stone and P. Goldbart, *Mathematics for Physics* (Cambridge University Press, 2009).
- [180] E. Demaine *et al.*, *Comput. Geom.* **42** (2009).
- [181] J. Hure, B. Roman, and J. Bico, *Phys. Rev. Lett.* **106** (2011).
- [182] J. Sadoc and R. Mosseri, *Geometric Frustration* (Cambridge University Press, 1999).
- [183] B. Roman and J. Bico, *J.Phys.* **22**, 493101 (2010).
- [184] B. Audoly and Y. Pomeau, *Elasticity and Geometry* (Oxford University Press, 2010).
- [185] M. Marder, R. Deegan, and E. Sharon, *Physics Today* (2007).
- [186] <http://www.susqu.edu/brakke/evolver/evolver.html>.
- [187] J. Nitsche, *Lectures on Minimal Surfaces* (Cambridge University Press, 1989).
- [188] P. Kralchevsky and K. Nagayama, *Particles at Fluid Interfaces and Membranes* (Elsevier, 2001).
- [189] H. K. D. Vella and L. Mahadevan, *J. Fluid Mech.* **502**, 89 (2004).
- [190] P. Castro-Villarreal, *J. Stat. Mech.* P08006, 2010.
- [191] H. Winkler, *Bauhaus: Weimar, Dessau, Berlin and Chicago* (MIT Press, 1978).
- [192] P. Jackson, *Complete Origami Course* (Doubleday, 1989).
- [193] J. Kim *et al.*, *Science* **335** (2012).
- [194] P. Shipman and A. Newell, *Phys. Rev. Letts.* **92**, 168102 (2004).
- [195] K. Kasahara, *Extreme Origami* (Sterling Publishing Co., Inc., New York, 2002).

- [196] S. Houliara and S. Karamanos, *J. Pressure Vessel Technol.* **133**, 011201 (2011).
- [197] E. Schmidt, *Math. Z.* **44** (1939).
- [198] M. Kaltenbrunner *et al.*, *Nature Communications* **3** (2012).
- [199] E. Sackmann and R. Bruinsma, Cell Adhesion As Wetting Transition? Les Houches Summer School **75**, 285 (2002).
- [200] E. Pairam and A. Fernández-Nieves, *Physical Review Letters* **102**, 234501 (2009).
- [201] L. Rayleigh, *Philosophical Magazine* **XXXIV**, 145 (1892).
- [202] S. Tomotika, *Proceedings of the Royal Society of London. Series A. Mathematical and Physical Sciences* **150**, 322 (1935).
- [203] C. Boys, *Soap Bubbles* (Thomas Y. Crowell Company (New York), 1962).
- [204] S. Chandrasekhar, *Hydrodynamic and Hydromagnetic Stability* (Clarendon Press, Oxford, 1961).
- [205] M. Moseler and U. Landman, *Science* **289**, 1165 (2000).
- [206] E.F. Goedde and M.C. Yuen, *Journal of Fluid Mechanics* **40**, 495 (1970).
- [207] H. Teng, C. Kinoshita, and S. Masutani, *Int.J. Multiphase Flow* **21**, 129 (1995).
- [208] R. Donnelly and W. Glaberson, *Proceedings of the Royal Society of London. Series A, Mathematical and Physical Sciences* **290**, 547 (1966).
- [209] L. Rayleigh, *Philosophical Magazine* **XXXIV**, 177 (1892).
- [210] T. Squires and S. Quake, *Reviews of Modern Physics* **77**, 977 (2005).
- [211] T. Faber, *Fluid Dynamics for Physicists* (Cambridge University Press, 1995).

- [212] R. Feynman, R. Leighton, and M. Sands, *The Feynman Lectures on Physics*, vol. 2 (Addison-Wesley Publishing Company, INC, 1964).
- [213] H. Becker and T. Massaro, *Journal of Fluid Mechanics* **31**, 435 (1968).
- [214] M. Bowick, D. Nelson, and A. Travesset, *Physical Review E* **69**, 041102 (2004).
- [215] J. Vanderlinde, *Classical Electromagnetic Theory* (Kluwer Academic Publisher, 2004), 2nd ed.
- [216] M. Andrews, *Journal of Electrostatics* **64**, 664 (2006).
- [217] S. Khuri and A. Wazwaz, *Applied Mathematics and Computation* **85**, 139 (1997).
- [218] F. Brochard, *Langmuir* **5**, 432 (1989).
- [219] D. Quéré and A. Ajdari, *Nat. Mater.* **5**, 429 (2006).
- [220] t. H. Linke, *Phys. Rev. Lett.* **96**, 154502 (2006).
- [221] A. R. Parker and C. Lawrence, *Nature* **414**, 33 (2001).
- [222] L. Zhai *et al.*, *Nano Lett.* **6**, 1213 (2006).
- [223] R. Wenzel, *Ind. Eng. Chem.* **28**, 988 (1936).
- [224] D. Vella, M. Adda-Bedia, and E. Cerda, *Soft Matter* **6**, 5778 (2010).
- [225] The contact area A_c of a droplet of radius R and a sinusoidal substrate can be calculated in the Cartesian coordinates with the origin at the center of the droplet. The contact area in the first quadrant is $A_c/4 = \sum_{i=0}^{N=R/\lambda} L_\lambda \sqrt{R^2 - x_i^2}$, where $x_i = i\lambda$ ($i = 0, 1, 2..N$) are the positions of the sinusoidal peaks. For $R \gg \lambda$, $\sum_{i=0}^{N=R/\lambda} \Delta i = \int_0^N di$, where $\Delta i = 1$. A_c can thus be obtained by integration.

- [226] T. Onda, N. S. S. Shibuichi, and K. Tsujii, *Langmuir* **12**, 2125 (1996).
- [227] H. von Koch, *Acta Math.* **30**, 145 (1906).
- [228] K. Falconer, *Fractal Geometry: Mathematical Foundations and Applications* (Wiley, New Jersey, 1990).
- [229] T. Ito and S. Okazaki, *Nature* **406**, 1027 (2000).
- [230] M. Nosonovsky and B. Bhushan, *Microsyst. Technol.* **11**, 535 (2002).
- [231] B. Bhushan ed, *Nanotribology and Nanomechanics: An Introduction* (Springer, New York, 2005).
- [232] M. Nosonovsky, *J. Chem. Phys.* **126**, 224701 (2007).
- [233] C. Yang, U. Tartaglino, and B. Persson, *Eur. Phys. J. E* **25**, 139 (2008).
- [234] Y. Zheng *et al.*, *Nature* **463** (2010).
- [235] P. Renvoise *et al.*, *Europhy Lett.* **86** (2009).
- [236] W. Russel, D. Saville, and W. Schowalter, *Colloidal Dispersions* (Cambridge University Press, 1992).
- [237] B. Honig and A. Nicholls, *Science* **268**, 1144 (1995).
- [238] F. Andrietti, A. Peres, and R. Pezzotta, *Biophys. J.* **16(9)**, 1121 (1976).
- [239] C. Tracy and H. Widom, *Physica A* **244**, 402 (1997).
- [240] L. D'yachkov, *Tech. Phys. Lett.* **31**, 204 (2005).
- [241] A. Loeb, J. Overbeek, and P. Wiersema, *The Electrical Double Layer Around a Spherical Particle* (M.I. T. Press, Cambridge, Mass., 1961).
- [242] J.-Y. Parlange, *J. Chem. Phys.* **57**, 376 (1972).

- [243] S. Brenner and R. Roberts, *J. Phys. Chem.* **77**, 2367 (1973).
- [244] E. Weisstein, *CRC Concise Encyclopedia of Mathematics* (CRC Press, 2003), 2nd ed.
- [245] S. Valluri, D. Jeffrey, and R. Corless, *Canad. J. Phys.* **78**, 823 (2000).
- [246] L. White, *J. Chem. Soc. Faraday Trans.* **2**, 577 (1977).
- [247] H. Ohshima, T. Healy, and L. White, *J. Colloid Interface Sci.* **90**, 17 (1982).
- [248] The PB equation can be written in a unified form: $C(x)\psi''(x) = \sinh \psi(x)$ in the planar ($C(x) = 1$ with $x = z$), cylindrical ($C(x) = \exp(-2x)$ with $x = \ln r$) and spherical ($C(x) = x^4$ with $x = 1/r$) cases.
- [249] M. Bier *et al.*, *J. Chem. Phys.* **130**, 024703 (2009).

VITA

NAME OF AUTHOR: Zhenwei Yao

PLACE OF BIRTH: Huzhou, China

DATE OF BIRTH: Dec 17, 1981

DEGREES AWARDED:

B.S., Physics, Xi'an Jiaotong University, China (2004)

M.S., Physics, Xi'an Jiaotong University, China (2007)

PROFESSIONAL EXPERIENCE:

Syracuse University, Department of Physics, Graduate Teaching/Research Assistant (2007-2012)

PUBLICATIONS:

- The Electric Double Layer Structure around Charged Spherical Interfaces, Z. Yao, M. Bowick and X. Ma, *J. Chem. Phys.* 136, 044106 (2012) [arXiv:1110.5309v2]
- Self-propulsion of droplets by spatially-varying roughness, Z. Yao, M. Bowick, *Soft Matter* 8(4), 1142 (2011) [arXiv:1106.5542v1]
- Morphology of nematic and smectic vesicles, X. Xing, H. Shin, M. Bowick, Z. Yao, L. Jia and M. Li, accepted to publish at PNAS (2011) [arXiv:1108.4763v1]
- The shrinking instability of toroidal liquid droplets in the Stokes flow regime, Z. Yao and M. Bowick, *Eur. Phys. J. E* 34, 32 (2011) [arXiv:1011.3437v3]
- Crystalline order on catenoidal capillary bridges, M. Bowick and Z. Yao, *Europhys. Lett.* 93, 36001 (2011) [arXiv:1012.4378v1]

- Equilibrium conformation of polymer chains with noncircular cross section, S. Zhao, S. Zhang, Z. Yao and L. Zhang, Phys. Rev. E 74, 032801 (2006) [arXiv:0805.2994v1]
- Buckling and competition of energy and entropy lead conformation of single-walled carbon nanocones, S. Zhang, Z. Yao, S. Zhao and E. Zhang, Appl. Phys. Letts. 89, 131923 (2006) [arXiv:0805.2992v1]

TALKS and PRESENTATIONS:

- Contributed talk, *The electric double layer structure around charged spherical interfaces*, APS March meeting, Boston, MA, 2012
- Invited seminar talk, *Instabilities of toroidal liquid droplets in the Stokes flow regime*, University of Pittsburgh, 2012
- Invited seminar talk, *Instabilities of toroidal liquid droplets in the Stokes flow regime*, Northwestern University, 2011
- Invited seminar talk, *Instabilities of toroidal liquid droplets in the Stokes flow regime*, The University of Chicago, 2011
- Invited seminar talk, *Instabilities of toroidal liquid droplets in the Stokes flow regime*, University of Massachusetts Amherst, 2011
- Seminar, *Self-propulsion of liquid droplet via inhomogeneous roughness*, Physics Department, Syracuse University, 2011
- Research Oral Presentation, *Instabilities of toroidal liquid droplets in the Stokes flow regime*, Syracuse University, 2011
- Sound bites talk, *Self-propulsion of liquid droplet via inhomogeneous roughness*, 11th New York Complex Workshop, Syracuse University, 2011

- Contributed talk, *Shrinking instabilities of toroidal liquid droplets in the Stokes flow regime*, APS March Meeting, Dallas, TX, 2011
- Sound bites talk, *Instability of toroidal liquid droplet*, 9th New York Complex Workshop, Cornell University, NY, 2010
- Contributed talk, *Rayleigh instability of toroidal liquid droplet*, APS March Meeting, Portland, OR, 2010
- Sound bites talk, *Shape of structured vesicles*, workshop on Soft Active Materials (I2CAM), Syracuse University, 2009